

IDENTIFICATION OF ROTORCRAFT STRUCTURAL DYNAMICS
FROM FLIGHT AND WIND TUNNEL DATA

Robert M. McKillip, Jr.
Principal Investigator

February 1997

FINAL REPORT COVERING THE PERIOD
FEBRUARY 1991 - AUGUST 1992

Prepared under NASA-Ames Agreement No. NAG 2-694

by

Robert M. McKillip, Jr.
(Former Assistant Professor)
for the Department of Mechanical and Aerospace Engineering
Princeton University
Princeton, New Jersey 08544

for

AMES RESEARCH CENTER
NATIONAL AERONAUTICS AND SPACE ADMINISTRATION
MOFFETT FIELD, CALIFORNIA 94035

NAG 2-694: Identification of Rotorcraft Structural Dynamics Characteristics from Flight and Wind Tunnel Data

Background

This research grant topic addressed the capability of using blade-mounted instrumentation, notably accelerometers, to reconstruct blade modal motion and forced response from both wind tunnel and flight test data. Two documents produced as a consequence of this investigation are attached as an Appendix: the first, "Reconstruction of Helicopter Rotor Blade Modal Properties and Examination of Blade-Mounted Sensor Data", comprised part of a visiting student's thesis for the degree of Diplom-Ingenieur from the University of Stuttgart; the second, "Instrumented Blade Experiments Using a Light Autogiro", is a conference paper from the 16th European Rotorcraft Forum, held in Glasgow, Scotland in September of 1990, and is a condensed version of a Master's Thesis submitted to the Department of Mechanical and Aerospace Engineering at Princeton University.

The first document explores, after some tutorial material, the possibility of identifying the forced modal response of the rotorblade using only accelerometer measurements. Through a collection of various filtering concepts, it is shown that some success may be achieved in this regard, although the method involves considerable "tuning" on the part of the engineer and hence is not yet suitable for "production" work. A finite element analysis is developed that provides some technical basis for design of the various filtering methods.

The second document discusses the developmental work associated with instrumenting a light autogiro's rotor blades with accelerometers for measurement of in-plane and out-of-plane response. Issues related to data formatting, power conditioning, and impact testing of the data system and sensors are discussed. The ultimate goal of the project - the demonstration testing of the system on the autogiro in towed operation - has yet to transpire, as the runway that was to serve as the test track was destroyed by the University to support further development of the Forrestal Campus.

While these two works did not directly generate a solution to this complex identification and measurement problem, they have aided the further development of this concept. On-going Navy-sponsored work related to rotor instrumentation and data processing has been able to utilize portions of each of these works to identify methods for extracting both rotor motion and applied loads from similarly instrumented rotorcraft. Results of this work have been recently reported at the American Helicopter Society's Annual Forum.



INSTITUT FÜR STATIK UND DYNAMIK DER
LUFT- UND RAUMFAHRTKONSTRUKTIONEN

Universität Stuttgart
Pfaffenwaldring 27, 7000 Stuttgart 80
Federal Republic of Germany



Princeton University

School of Engineering and Applied Science
Department of Mechanical and Aerospace Engineering

P.O. Box CN5263
Princeton, New Jersey 08544-5263

**RECONSTRUCTION OF HELICOPTER ROTOR BLADE MODAL
PROPERTIES AND
EXAMINATION OF BLADE-MOUNTED SENSOR-DATA**

by
Thorsten Breitfeld

Prepared at:
Princeton University
School of Engineering and Applied Science
Department of Mechanical and Aerospace Engineering
Princeton, New Jersey
May 1990

Submitted to:
Institut für Statik und Dynamik der Luft- und Raumfahrtkonstruktionen
Universität Stuttgart
in partial fulfillment of the requirements for the degree of Diplom-Ingenieur in
Aerospace Engineering from the University of Stuttgart

Prepared by:

cand. aer. Thorsten Breitfeld

Approved by:

Professor Robert M. McKillip, Jr.
Thesis Advisor
Princeton University

Prof. Dr.- Ing. Dieter Dinkler
Betreuer
Universität Stuttgart

Table of Contents

List of Symbols	iv
Notational Conventions.....	iv
List of Abbreviations.....	iv
List of Symbols, Chapter 1.....	v
List of Symbols, Chapter 2.....	vi
List of Symbols, Chapter 3.....	vii
 Introduction.....	 1
 1. Analysis of Structural Vibration.....	 1
1.1 Introduction to Modal Theory.....	3
1.1.1 Modal Theory.....	3
1.1.2 Orthogonality Conditions.....	7
1.1.3 Structures with Distributed Mass.....	9
1.1.4 The Finite Element Theory.....	13
1.2 Experimental Modal Analysis.....	14
 2. Modeling the Beam by the Finite Element Method.....	 20
2.1 Introduction.....	20
2.1.1 The Element Stiffness Matrix.....	20
2.1.2 The Element Mass Matrix.....	21
2.1.3 Assembly of the Structure Stiffness Matrix.....	22
2.1.4 Assembly of the System Mass Matrix.....	23
2.1.5 Static Reduction of the System Matrices.....	23
2.1.6 Treatment of Singular Matrices.....	25
2.2 Results of the Non-Rotating (Static) Analysis.....	28
2.3 Prediction of the Rotating Natural Frequencies.....	32
2.3.1 Predicting the Bending Frequencies of a Rotating Beam given the Non-Rotating Bending Frequencies.....	32
2.3.2 Linear Height and Stiffness Distributions.....	35
2.3.3 Determining the Rotating Mode Shapes.....	36
2.3.4 Natural Frequency as a Function	

of Rotational Speed.....	40
2.3.5 Accuracy and Convergence Characteristics for this Finite Element Application.....	43
2.4 Comparison of the Finite Element Calculation with the Full-Scale UH-60A Rotor Blade	
Non-Rotating Modal Analysis Shake Test.....	46
2.4.1 NASA Shake Test.....	46
2.4.2 Shake Test Results.....	49
2.4.2.1 Rotor Blade Data for Shake Test.....	49
2.4.3 Results of the Non-Rotating Finite Element Analysis.....	51
2.4.3.1 Discretization Technique.....	51
2.4.3.2 Results from other Boundary Conditions.....	60
2.4.4 Rotating Results.....	61
2.4.4.1 Increase of the Natural Frequencies.....	61
2.4.4.2 Comparison between Rotating and Non-Rotating Predicted Mode Shapes	63
3. Spectral Analysis of the UH 60A Flight Records.....	68
3.1 Introduction.....	68
3.2 Projected Natural Frequencies.....	74
3.3 Analysis Procedure.....	74
3.3.1 Obtaining the Spectral Density Distribution.....	74
3.3.2 Ideal Boxcar Filters in the Frequency Domain.....	76
3.3.3 Mapping to the Z-Plane.....	76
3.3.4 Digital Filter Design.....	77
3.3.5 Power Spectral Ratios.....	79
3.3.6 Discussion of the Power Spectral Density Ratios.....	93
Appendix A.....	95
Tables of the First Eigenvectors of Beams with Different Boundary Conditions and Geometric Properties.....	95

Appendix B.....	98
Measured Residuals of the NASA - Shake Test.....	98
Appendix C.....	102
Finite Element Program for Rotating Structures.....	102
References	129
References, Part A.....	129
References, Part B.....	129
References, Part C.....	131

List of Symbols

Unless otherwise given in the text, the following symbols are defined as they are given below.

Notational Conventions

- (1) Vectors are denoted by a line under the symbol (as in \underline{u})
- (2) Matrices are shown in the shadow typefont (as in \mathbb{U})
- (3) $(\dot{})$ denotes the first derivative with respect to time
- (4) $(\ddot{})$ denotes the second derivative with respect to time
- (5) $()'$ denotes the first derivative with respect to an independent variable
- (6) $()''$ denotes the second derivative with respect to an independent variable
- (7) $(\tilde{})$ denotes a time dependency of a variable
- (8) $()^T$ denotes a transposed matrix
- (9) $()^{-1}$ denotes an inverse matrix
- (10) $[]$ denotes the diagonal of a matrix
- (11) $\|\|$ denotes the norm of a matrix
- (12) $\mathcal{L}[x(t)] = X(s)$ Laplace transform of $x(t)$

List of Abbreviations

BLT	Bilinear Transformation
BW	Butterworth
CAMRAD	Comprehensive Analytical Model of Rotorcraft Aerodynamics and Dynamics
CE	Characteristic Equation
CH	Chebycheff
CT	Continuous Time
DFT	Discrete Fourier Transform
DOF	Degrees of Freedom ()

DS	Division Schemes
DT	Discrete Time
FFT	Fast Fourier Transform
FRF	Frequency Response Function
MTR	Modern Technology Rotor
NASA	National Aeronautics and Space Administration
PSD	Power Spectral Density
TRENDS	Tilt Rotor Engineering Data System

List of Symbols, Chapter 1

given in order of occurrence

E	Modulus of elasticity
I	Stiffness
B	$E * I$
M	System mass matrix
m	Element mass matrix
D	System damping matrix
K	System stiffness matrix
k	Element stiffness matrix
F	Outside forces on a System
t	Time
ω_n	n-th Natural frequency
λ_n	n-th Eigenvalue ($\omega_n = \lambda_n^{0.5}$)
\underline{u}_n	n-th normalized eigenvector
U	Modal system matrix
$q_1(t)$	Time dependency
\tilde{q}_i	Amplitudes of the specific mode at a point in time $q(t) := \tilde{q}$
m_{gen}	Generalized mass matrix
$m_{gen,j}$	j-th element of the generalized mass matrix
k_{gen}	Generalized stiffness matrix
$k_{gen,j}$	j-th element of the generalized stiffness matrix
Θ	Modal matrix (as in $\Theta M \Theta = I$)
I	Identity matrix
R	Generalized force ($U^T \tilde{F} = R$)

Q	Shear force
μ	Mass distribution
M	Bending moment
κ	Radius of curvature
$\xi_j(x)$	i -th eigenfunction
l	Length of a beam
c_{ij}	Element of the coefficient matrix for the polynomial approach
s	Complex Laplace variable
$F(s)$	Laplace Transform of the Excitation
$f(s)$	Element of $F(s)$
$H(s)$	Frequency response matrix, or transfer matrix
$h(x)$	Element of $H(s)$
p_k and p_k^*	Conjugate complex roots
r	Residues
\mathbb{R}	Residue matrix

List of Symbols, Chapter 2

given in order of occurrence

\underline{P}	Vector of static forces and moments
$\underline{\delta}$	Vector of linear and angular displacements
u	Linear displacement
φ	Angular displacement
\mathbb{K}_{re}	Stiffness matrix with rearranged rows and columns
\mathbb{M}_{re}	Mass matrix with rearranged rows and columns
\mathbb{T}	Transformation matrix for static condensation
$\hat{\mathbb{M}}$	Reduced mass matrix
$\hat{\mathbb{K}}_{uu}$	Reduced stiffness matrix
\mathbb{D}	Diagonal matrix of the eigenvalues
$\tilde{w}_i(x)$	i -th element of the rotating mode shape vector
$w_1^{(n)}(x)$	i -th element of the n -th non-rotating mode shape
N_a	Number of nights lain awake, hoping all this would work out
\tilde{q}_n	Time and amplitude dependency of the n -th non rotating mode
U	Potential energy
T	Kinetic energy
Δ_i	Shortening of the blade at the radial position x_i along the beam

\mathbb{K}_{stat}	Non rotating stiffness Matrix
\mathbb{K}_{dyn}	Additional terms of the stiffness matrix brought on by rotation
\mathbf{U}_{rot}	Modal matrix of the rotating system
Ψ	Rotational parameter
Ω	Rotational speed of the system
Φ	Rotational parameter
$w_i(x)$	Deflection at the i-th point of the system
Λ	Diagonal matrix of the λ 's \mathbf{r} vectorial remainder,
E_{adj}	Adjusted modulus of elasticity

List of Symbols, Chapter 3

given in order of occurrence

R_{xx}	Correlation function
$S_{xx}(\omega)$	Power spectral density
$z \equiv e^{(sT)}$	The z-transform
$s = \sigma + i\omega$	Laplace variable
f_n	Nyquist frequency
f_c	Cutoff frequency
f_s	Stopband frequency
f_{samp}	Sampling frequency
ω	Continuous time filter frequency
Ω	Digital filter frequency
T	Period of oscillation

Introduction

Excessive vibration remains one of the most difficult problems that faces the helicopter industry today, affecting all production helicopters at some phase of their development. Vibrations in rotating structures may arise from external periodic dynamic airloads whose frequencies are close to the natural frequencies of the rotating system itself. The goal for the structures engineer would thus be to design a structure as free from resonance effects as possible. In the case of a helicopter rotor blade these dynamic loads are a consequence of asymmetric airload distribution on the rotor blade in forward flight, leading to a rich collection of higher harmonic airloads that force rotor and airframe response. Accurate prediction of the dynamic characteristics of a helicopter rotor blade will provide the opportunity to affect in a positive manner noise intensity, vibration level, durability, reliability and operating costs by reducing objectionable frequencies or moving them to a different frequency range and thus providing us with a lower vibration rotor. In fact, the dynamic characteristics tend to define the operating limits of a rotorcraft. As computing power has increased greatly over the last decade, researchers and engineers have turned to analyzing the vibrational characteristics of aerospace structures at the design and development stage of the production of an aircraft. Modern rotor blade construction methods lead to products with low mass and low inherent damping so careful design and analysis is required to avoid resonance and an undesirable dynamic performance. In addition, accurate modal analysis is necessary for several current approaches in elastic system identification and active control.

1. Analysis of Structural Vibration

The analysis procedure falls into the two categories: experimental structural analysis which involves the testing and measurement of an actually built structure, and analytical structural analysis, which consists of mathematically modeling a structure on a computer and predicting its response to excitations as well as inferring the inherent vibrational characteristics like mode shape and natural frequency. Structural analysis based on a computational

method allows the freedom to either experiment with a new design or change an existing design and then to make a statement about the magnitude of the changes in dynamic properties resulting from some perturbation of the original design. This relieves the designer from making costly physical changes to the system itself until he is satisfied with the characteristics presented to him in the simulation. One of the major problems to date is that none of the analytic models developed for the simulation of rotor blade behavior are capable of an accurate response prediction over the entire flight envelope of a helicopter. An exact model would have to include detailed unsteady aerodynamic predictions for the airloads as well as nonlinear geometric coupling effects due to the blade rotation.

In response to this discrepancy between predicted and measured vibrational behavior, the US Army in conjunction with NASA, has undertaken a program of flight testing a highly instrumented UH-60A "Blackhawk" helicopter. The purpose of these experiments is to provide the industry and the university research community with a wealth of flight test data obtained under specific flight conditions. This data would serve to be correlated and compared with various parts of currently ongoing aeroelastic and vibrational helicopter rotor and airframe simulations. It is hoped that finding and evaluating the discrepancies between the database and simulation results will improve the understanding into where the engineering approximations and assumptions in the simulation programs are deficient. The database was further extended by conducting a static, non-rotating shake test of the same UH-60A rotor blade. In this shake test it was possible to determine the non-rotating dynamic properties of the rotor blade by identifying its modes of vibration and natural frequencies. As any vibrational state can be said to consist of a specific combination of its vibrational modes, each having a particular natural frequency, we find the area of coincidence of the analytical and experimental part of structure dynamics here. It is always important to have one set of measurements to quantify the accuracy of the mathematical model. The simulation model can then be adjusted or altered to better conform to the real model. Having once learned that the mathematical model does indeed correspond with the experimental data, the engineer can change the structural and material properties of his mathematical model with a high degree of confidence that his simulation calculations will reflect the real performance of the structure he is designing.

1.1 Introduction to Modal Theory

The dynamic properties of an elastic structure are most commonly modeled using either a set of linear differential equations in the time domain, or by a set of algebraic equations after a Fourier transform of these differential equations of motion. The latter is commonly used during the actual testing phase of a design. First we will examine the former.

1.1.1 Modal Theory

In the analysis of dynamic systems having one or more degrees of freedom and their response to any sort of excitation, the theory of modal analysis can be applied to the structure.

The modal theory simply states that any shape of the oscillating structure can be expressed in terms of natural modes of the structure and the degree of the participation of these modes. The natural modes are the physical shape that the structure takes when excited at a natural frequency. An easy way of thinking of these natural modes is to consider the following two degree of freedom system (Fig 1.1) composed of two masses that are connected by two springs and two damping devices. The number of natural modes that one can expect to find always corresponds to the number of degrees of freedom. It follows that we can expect to find 2 normal modes and their natural frequencies.

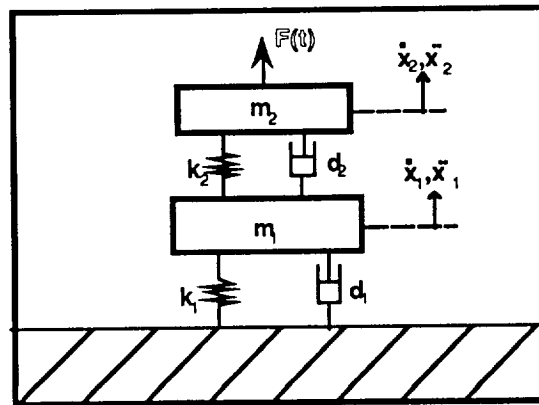


Fig 1.1 A dynamic System

As this structure is excited with a force, $F(t)$, of variable frequency, we can envision two cases in which the masses vibrate in a stationary way. In one case, the masses will vibrate in phase with each other, though with different amplitudes. In the other case, they will vibrate 180 degrees out of phase with each other. Both these cases are associated with a natural frequency of the system. The system is a *lumped parameter model*, consisting of two discrete mass points. After deriving all the necessary equations for the lumped parameter model, we will expand the theory to encompass structures with distributed mass, i.e. beams.

When we set up the equations of motion for a linear system, we obtain the familiar equation in matrix-form :

$$\mathbf{M} \ddot{\underline{x}} + \mathbf{D} \dot{\underline{x}} + \mathbf{K} \underline{x} = \underline{F}(t) \quad (1.1.1-1)$$

This equation represents the force balance between the inertial ($\mathbf{M} \ddot{\underline{x}}$), dissipative ($\mathbf{D} \dot{\underline{x}}$) and restoring forces ($\mathbf{K} \underline{x}$) and all outside forces ($\underline{F}(t)$). For any model of a structure or system, with any number of degrees of freedom (DOF), as long as we use only masses, springs and proportional dampers, we will obtain the above form of the equations of motion. All linear properties of a structure can be defined by the mass, damping and stiffness matrices. We now have a system of second order coupled differential equations that are linear and time-invariant. \mathbf{M} , \mathbf{D} and \mathbf{K} are matrices of the dimension ($n \times n$), n being the number of DOF. The equation is coupled because the \mathbf{D} and \mathbf{K} matrices are not diagonal, only symmetric. To uncouple these equations we must find a basis for this system, in which all the matrices become diagonal, thus reducing the n coupled equations to a system of n uncoupled equations. This can be thought of as reducing the structure to a system of masses with one DOF each. The process is called *modal decomposition*. Modal decomposition in the case of light damping or if the damping matrix is proportional to either the mass or stiffness matrix, or proportional to both leads to real modes, while any damping that does not fall into the beforementioned categories will lead to complex modes.

To execute such a modal decomposition we will have to find the eigenvalues, λ , (or natural frequencies $\omega_n = \lambda_n^{0.5}$) and the eigenvectors, \underline{u} , of our structure. In the

interest of simplicity we will disregard damping in the following derivations and solve the homogeneous form of (1.1.1-1). Assuming for $\underline{x}(t)$

$$\underline{x}(t) = \underline{u} e^{\lambda t} \quad (1.1.1-2)$$

and thus

$$\ddot{\underline{x}} = \lambda^2 \underline{u} e^{\lambda t} = \lambda^2 \underline{x}$$

Substituting into (1.1.1-1) and solving for λ leads to

$$(\lambda^2 \mathbf{M} + \mathbf{K}) \underline{u} = 0 \quad (1.1.1-3)$$

This gives us the characteristic equation (CE) for the structure. A non-trivial solution exists only when

$$\det(\lambda^2 \mathbf{M} + \mathbf{K}) = 0 \quad (1.1.1-4)$$

This CE is a polynomial whose roots are the eigenvalues of the system. Depending on the kind of polynomial that the CE represents, we can imagine the roots to be of different character. If we assume zero damping in our example case we would find 4 complex roots or a pair of conjugate complex roots. The roots are purely imaginary, having no real part. Successively inserting these roots back into equation (1.1.1-3), we receive the matrix equations for the eigenvectors \underline{u} . These eigenvectors are only defined in terms of their direction, not their magnitude, since the matrix equations are linearly dependent. (Traditionally the eigenvectors are scaled so that some DOF that is in some way predominant is unity. In the case of vibrating beams we will always set that DOF to unity that displays the maximum deflection). The vectors thus calculated are the normalized eigenvectors, \underline{u}_n , associated with the natural frequency, ω_n , or the n -th eigenvalue, λ_n . In our example, we would get two of these eigenvectors, and could assemble them into the *modal system matrix* $\mathbf{U} = [\underline{u}_1, \underline{u}_2]$.¹

¹Let us consider the system matrix that was found for our example: First of all we must remember that the eigenvectors were arbitrarily scaled, so that they represent only the amplitude relations of the oscillations of the lumped parameter masses. Recognizing this, we find that for $m_1=m_2$, $d_1=d_2=0$ and $k_1=k_2$ that our eigenvectors are:

Another very helpful way of understanding the significance of eigenvectors can be found in Ref 1.-1. The eigenvalue/eigenvector form gives an interesting insight into the nature of the solution:

$$\left(\frac{1}{\omega_n}\right) \underline{u}_n = \mathbb{K}^{-1} \mathbb{M} \underline{u}_n \quad (1.1.1-4)$$

The right-hand side of this equation subjects the displacement vector at each lumped mass (\underline{u}_n) to a matrix multiplication which should both extend and rotate this vector. The same vector, on the left side of the equation, is simply subjected to a multiplication with a scalar constant, resulting in only a expansion of the vector but no change in its orientation. So, the vectors we are seeking, are vectors that are not rotated by the matrix multiplication on the right-hand side. Such solution vectors are the eigenvectors.

Using these eigenvectors, we are in the position to modaly decompose the equations of motion. We have said that every form that the oscillating structure takes can be expressed in terms of the eigenvectors :

$$\underline{x}(t) = \underline{u}_1 q_1(t) + \underline{u}_2 q_2(t) = [u_1 \ u_2] \begin{bmatrix} q_1 \\ q_2 \end{bmatrix} = \mathbb{U} \tilde{\underline{q}} \quad (1.1.1-5)$$

note: $\underline{q}(t) := \tilde{\underline{q}}$

\tilde{q}_1 and \tilde{q}_2 give the amplitudes of the specific mode at a point in time and thus are responsible for the time-dependency of the equation of motion. They are unknown until some initial conditions are introduced to the problem.

$$\underline{u}_1 = \begin{pmatrix} 0.618 \\ 1 \end{pmatrix}$$

$$\underline{u}_2 = \begin{pmatrix} -1.618 \\ 1 \end{pmatrix}$$

We see, that for the first resonant, or natural frequency, the masses are oscillating in phase (both components of the eigenvectors have the same sign). For the second resonant frequency the masses are oscillating 180° out of phase.

It can be shown that a front and back multiplication with the modal matrix, \mathbf{U} , the mass and stiffness matrices are diagonalized (this uses the orthogonality condition, explained later).

$$\mathbf{M}_{\text{diag}} = \mathbf{U}^T \mathbf{M} \mathbf{U} \quad (1.1.1-6a)$$

$$\mathbf{K}_{\text{diag}} = \mathbf{U}^T \mathbf{K} \mathbf{U} \quad (1.1.1-6b)$$

So, taking our original equation (1.1.1-1) and inserting (1.1.1-2) and then multiplying both sides by \mathbf{U} we get:

$$\mathbf{U}^t \mathbf{M} \mathbf{U} \ddot{\tilde{\mathbf{q}}} + \mathbf{U}^t \mathbf{K} \mathbf{U} \tilde{\mathbf{q}} = \mathbf{U}^t \mathbf{F}(t) \quad (1.1.1-7)$$

or

$$\mathbf{M}_{\text{diag}} \ddot{\tilde{\mathbf{q}}} + \mathbf{K}_{\text{diag}} \tilde{\mathbf{q}} = \tilde{\mathbf{f}} \quad (1.1.1-8)$$

with

$$\tilde{\mathbf{f}} := \mathbf{U}^t \mathbf{F}(t)$$

Which are, essentially the uncoupled equations of motion for the structure we are examining.

1.1.2 Orthogonality Conditions

By the transformation employed in eq. (1.1.1-6) , we have used the so-called orthogonality conditions, that must be validated in order for the transformation to work. These are

For the mass matrix :

$$\underline{u}_j^t \mathbf{M} \underline{u}_k = 0 \quad \text{for all } j \neq k \quad (1.1.2-1)$$

$$\underline{u}_j^t \mathbf{M} \underline{u}_j = m_{\text{gen},j} \quad \text{for } j=k \quad (1.1.2-1a)$$

and for the stiffness matrix :

$$\underline{u}_j^t \mathbb{K} \underline{u}_k = 0 \quad \text{for all } j \neq k \quad (1.1.2-2a)$$

$$\underline{u}_j^t \mathbb{K} \underline{u}_j = k_{gen,j} \quad \text{for } j=k \quad (1.1.2-2b)$$

For a mechanical explanation of this, we can consider that the mass-forces $-\omega_j^2 \mathbb{M} \underline{u}_k$ of the k-th eigenfunction does not perform work on the displacements u_j of another (different) eigenfunction j. The work being done on this eigenfunction is through the mass-forces of its own eigenfunction $-\omega_j^2 \mathbb{M} \underline{u}_j$. The numerical value of m_{gen} , that results from the front and back multiplication of the mass matrix by the modal matrix, is called the *generalized mass*.

In addition, inserting (1.1.2-1) and (1.1.2-2) into the equations for the eigenvalues we get an additional n equations. for the natural frequencies:

$$-\omega_j^2 m_{gen,j} + k_{gen,j} = 0 \quad (1.1.2-3)$$

or

$$\omega_j^2 = \frac{k_{gen,j}}{m_{gen,j}} \quad (1.1.2-4)$$

The uncoupled equations of motion take on the following form:

$$m_{gen,j} \ddot{\tilde{q}}_j + k_{gen,j} \tilde{q}_j = \tilde{r}_j \quad j=1, \dots, n \quad (1.1.2-5)$$

These n equations of motion for one DOF systems can be solved one after the other and after superimposing these solutions we get the total response of the system :

$$\underline{x}(t) = \sum_{j=1}^n \underline{u}_j \tilde{q}_j = \mathbf{U} \tilde{\mathbf{q}} \quad (1.1.2-6)$$

This equation also represents the transformation from the physical coordinate system to the modal coordinate system with the orthogonal eigenvectors of the structure as its basis.

A more intuitive and useful modal decomposition procedure is to choose the magnitude of the eigenvectors \underline{u} in such a manner that the front and back multiplication of the mass matrix by the modal matrix results in a unity matrix for the generalized mass matrix and a stiffness matrix that has only $\omega_n^2 = \lambda_n$ on its diagonal.²

$$\Theta \mathbf{M} \Theta = \mathbf{I} \quad (1.1.2-7)$$

and

$$\Theta \mathbf{K} \Theta = [\lambda_n] \quad (1.1.2-8)$$

The uncoupled equations of motion in modal coordinates now read

$$\mathbf{I} \ddot{\tilde{\mathbf{q}}} + [\lambda_i] \tilde{\mathbf{q}} = \mathbf{U}^T \tilde{\mathbf{F}} \quad (1.1.2-9)$$

With

$$\mathbf{U}^T \tilde{\mathbf{F}} = \mathbf{R} \quad (1.1.2-10)$$

as the generalized force and

$$\mathbf{x}(t) = \Theta \tilde{\mathbf{q}} \quad (1.1.2-11)$$

as the transfer equation to modal coordinates.

1.1.3 Structures with Distributed Mass

² Scaling the eigenvectors \underline{u} to achieve this is termed orthonormalizing the eigenvectors. These orthonormalized eigenvectors are denoted $\underline{\phi}$ and found by

$$\underline{\phi}_n = \left(\frac{1}{m_n} \right)^{0.5} \underline{u}_n$$

The orthonormal modal matrix is Θ .

In the case of a beam for instance, we cannot necessarily discretize the system as a lumped parameter model if we want to achieve a fair amount of accuracy. So, we take the mass distribution into account and set up a continuous system. The eigenvectors of such a system turn into eigenfunctions as the discretization becomes finer.

The differential equations of motion for a beam can be quickly derived by applying the three kinds of equations used to solve any structural dynamics problem: equilibrium condition, material law and the kinematic law. Consider an element of the beam:

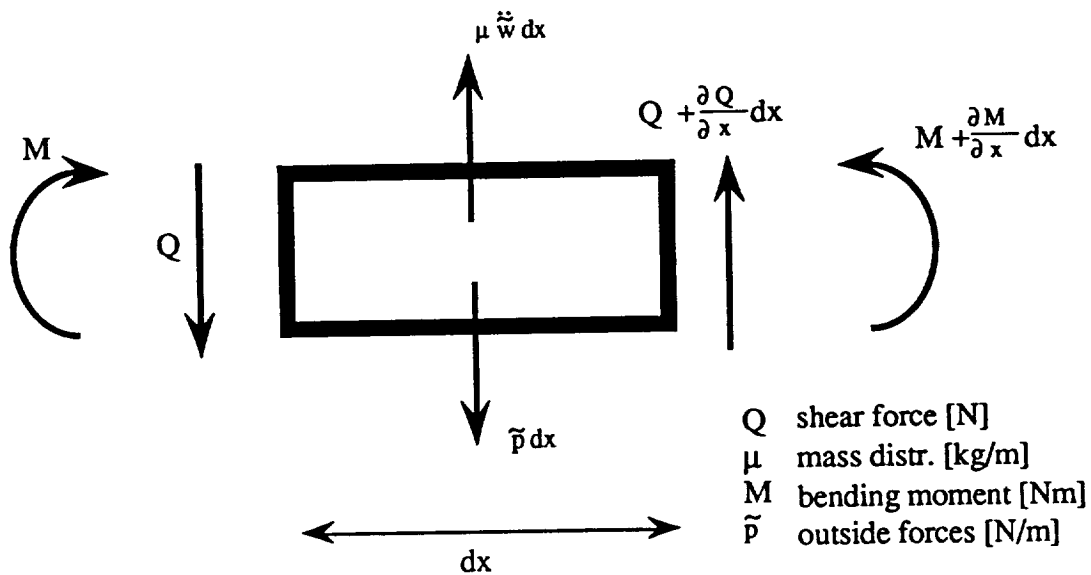


Fig 1.1.3-1 Beam Element

Equilibrium Conditions

Moment (disregarding 2nd order terms

Shear

and the rotational inertia of the element)

$$\left(\frac{\partial M}{\partial x}\right) = Q$$

$$Q = \mu \ddot{w} - \tilde{p}$$

$$M'' = Q'$$

$$\Rightarrow M'' + \tilde{p} - \mu \ddot{w} = 0$$

Material Law

$M = EI \kappa$ (the linear relationship: bending moment- radius of curvature κ)

Kinematics

$$\kappa = -w''$$

If the modulus of elasticity is constant, we can write

$$B(x) = E I(x)$$

and the differential equation of motion are

$$[B(x) \tilde{w}''(x)]'' + m(x) \ddot{\tilde{w}}(x) = \tilde{p} \quad (1.1.3-1)$$

Or considering a uniform beam, the equation reduces to

$$B \tilde{w}'''' + m \ddot{\tilde{w}} = \tilde{p} \quad (1.1.3-1a)$$

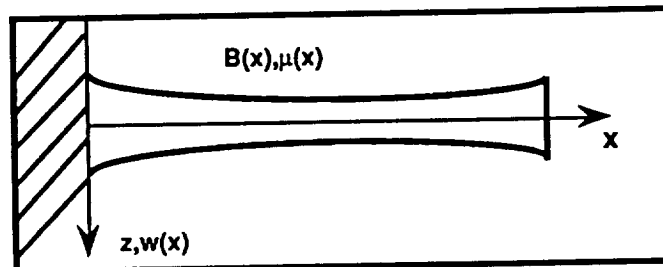


Fig 1.1.3-2 Cantilever Beam

As in the case of the lumped parameter model, we assume that it is also possible to modally decompose this beam into decoupled, one-DOF oscillatory systems. In addition we stated that the response of such a system could be expressed by a superposition of its eigenvectors, \underline{u}_j , and a participation factor, \tilde{q}_j , that carried the timevariation of the system. Now, in examining a continuous system, the eigenvectors are replaced by eigenfunctions $\xi_j(x)$. So the equation for the superposition of the eigenvectors now is

$$\tilde{w}(x) = \sum_i \xi_i(x) \tilde{q}_i(x) \quad (1.1.3-2)$$

In the case of a uniform beam it is still possible to find an analytical solution for the eigenfunctions. Using the boundary conditions for a cantilever beam, this solution is

$$\xi_i(x) = \frac{\cosh\{\lambda_i x\} - \cos\{\lambda_i x\}}{\cosh\{\lambda_i l\} + \cos\{\lambda_i l\}} - \frac{\sinh\{\lambda_i x\} - \sin\{\lambda_i x\}}{\sinh\{\lambda_i l\} + \sin\{\lambda_i l\}} \quad (1.1.3-3)$$

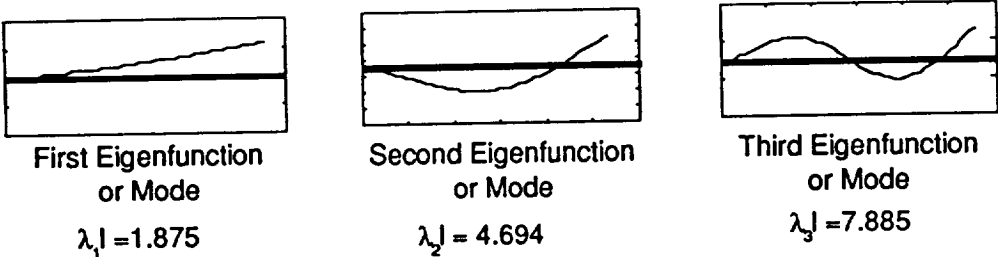


Fig 1.1.3-3 First Three Eigenmodes

Clearly, if the beam has a mass distribution and a changing geometry along its axis, an analytical solution can no longer be found and one must revert to numerics. A polynomial is used to approach the eigenfunction of the beam. The beam is discretized into small parts in a consistent manner and eigenvectors of the discrete system are calculated. The element of the eigenvector \underline{u}_n is understood to be the deflections of the structure at that lumped mass m_{nn} . The polynomial is laid through these points of deflections in order to attain a estimate of the shape- or eigenfunction.

The polynomial approach is written

$$\xi_i(x) = \sum_j c_{ij} \eta_j(x) \quad (1.1.3-4)$$

inserting this into eq. (1.1.3-2) gives us:

$$\tilde{w}(x) = \sum_i \sum_j c_{ij} \eta_j(x) \tilde{q}_i(x) \quad (1.1.3-5)$$

where c_{ij} being the coefficient matrix for the polynomial approach. In closing, note the similarities between the discrete formulation and the continuous formulation of the problem:

$$m_j \ddot{\tilde{q}}_j + d_j \dot{\tilde{q}}_j + k_j \tilde{q}_j = \tilde{r}_j \quad (1.1.3-5)$$

	Discrete System $j= 1...N$	Discrete System $j= 1...∞$
Eigenforms or mode shapes	\underline{u}_j - vector	$\xi_j(x)$ - function
generalized mass m_j	$\underline{u}_j^t \mathbf{M} \underline{u}_j$	$\int_0^l \mu(x) \phi_j^2(x) dx$
generalized damping d_j	$k_m m_j + k_s s_j$	$k_m m_j + k_s s_j$
generalized stiffness k_j	$\underline{u}_j^t \mathbf{K} \underline{u}_j$	$\int_0^l B(x) \xi_j''^2(x) dx$
generalized forces p_j	$\underline{u}_j^t \underline{p} f(t)$	$\int_0^l \xi_j(x) p(x) dx$
Response of System	$\tilde{\mathbf{x}} = \sum_{j=1}^N \underline{u}_j \tilde{q}_j$	$\tilde{w} = \sum_{j=1}^{\infty} \xi_j(x) \tilde{q}_j$

Table 1.1.3-1 Continuous and Discrete Systems

1.1.4 The Finite Element Theory

The Finite Element Theory is an approach that discretises the system into small, well defined pieces whose properties are known, and derives the vibration characteristics by assembling these small parts back to the large system and solving the equation of motion and decoupling them. The use of finite element techniques for dynamic structure analysis introduces great flexibility to rotorcraft design which is needed because of the often complex root geometry and nonlinear stiffness and mass distribution of the blade. The application and implementation of Finite Elements will be discussed in detail later.

1.2 Experimental Modal Analysis

Experimental measurements are usually made in the Laplace-Domain (also known as the *Frequency Domain*). This form of vibrational analysis became popular as very fast algorithms for the Fast Fourier Transform (FFT) and the Discrete Fourier Transform (DFT) were developed in the 1960's. The ability of these Digital Fourier Analyzers to quickly convert time histories and extract modal characteristics in the frequency domain has made them an important tool in measuring the modal characteristics of structures. The NASA shake test identified the modal residues of the UH-60A rotor blade. To correctly interpret this data we must look a little closer at the theory behind modal residues, the FFT and the Laplace-domain.

Consider the second order differential equation of motion derived in a previous chapter :

$$\mathbf{M} \ddot{\underline{x}} + \mathbf{D} \dot{\underline{x}} + \mathbf{K} \underline{x} = \mathbf{F}(t) \quad (1.1.1-1)$$

1.2.1 The Laplace Transform

Any function of time can be transformed into an analytical function of the complex variable, s , in the Laplace domain by the Laplace transform. There it can be algebraically altered and transformed back into the time domain. The greatest advantage that this transformation gives is that the differential equation of motion is changed into a simple polynomial that is much easier to solve. The transformation equation to the Laplace-domain from the time-domain is

$$\mathcal{L} [x(t)] = X(s) = \int_0^{\infty} e^{-st} [x(t)] dt \quad (1.2.1-1)$$

and the back-transform is

$$\mathcal{L}^{-1} [X(s)] = x(t) = \int_0^{\infty} e^{-st} [X(s)] dt \quad (1.2.1-2)$$

The complex Laplace variable s gives the relationship and magnitude of frequency and damping parameters on a complex plane is shown in Fig 1.2.1-1.

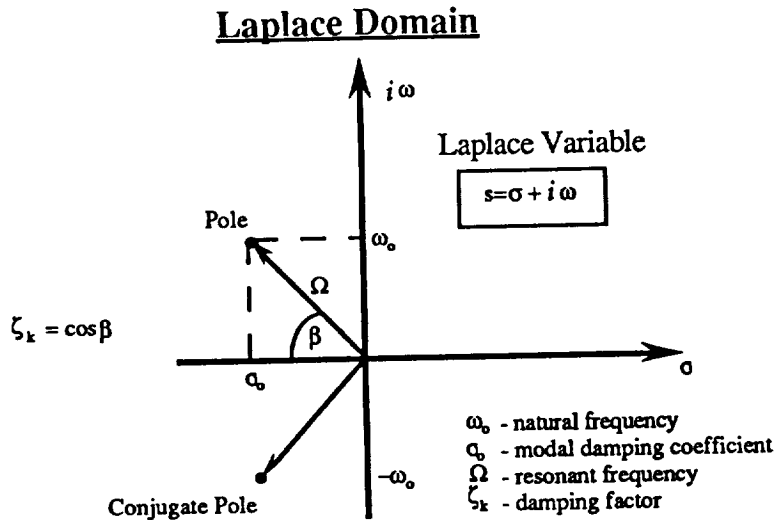


Fig 1.2.1-1 The Laplace Domain

The transform of a variable x to the Laplace domain will be written as $\mathcal{L}[x]$. To use this Laplace transform on our differential equation we need the transformation of \dot{x} and \ddot{x} .

$$\mathcal{L}\left[\frac{dx}{dt}\right] = \int_0^{\infty} e^{-st} \left[\frac{dx}{dt}\right] dt \quad (1.2.1-3)$$

Integrating this by parts finally gives us

$$\mathcal{L}\left[\frac{dx}{dt}\right] = s \mathcal{L}[x] - x(0) \quad (1.2.1-4)$$

or

$$\mathcal{L}[\dot{x}] = s X(s) - x(0) \quad (1.2.1-5)$$

Similarly we can find

$$\mathcal{L}\left[\frac{d^2x}{dt^2}\right] = \mathcal{L}[\ddot{x}] = s^2 X(s) - s x(0) - \dot{x}(0) \quad (1.2.1-5)$$

If we ignore the initial conditions (which can always be done for stable systems) this transforms our equations of motion to

$$\mathbf{M} s^2 X(s) + \mathbf{D} s X(s) + \mathbf{K} X(s) = \mathbf{F}(s) \quad (1.2.1-5)$$

an algebraic equation in the complex variables. It can be easily seen that the mathematics do indeed take on a simpler form in this domain.

Solving for $X(s)$

$$X(s) = \frac{\mathbf{F}(s)}{\mathbf{B}(s)} \quad (1.2.1-5)$$

where

$X(s)$ = Laplace Transform of the Response

$\mathbf{F}(s)$ = Laplace Transform of the Excitation

$\mathbf{B}(s) = \mathbf{M} s^2 + \mathbf{D} s + \mathbf{K}$

This equation is used as the basis to define the Frequency Response Function (FRF) such that:

$\text{L.-transform of the Output} = \text{FRF} \cdot \text{L.-transform of the Input}$ <p>or</p> $X(s) = \mathbf{H}(s) F(s)$

with $\mathbf{H}(s) = [\mathbf{M} s^2 + \mathbf{D} s + \mathbf{K}]^{-1}$, the Frequency Response Matrix

Now all the outside forces, responses of the structure, velocities, accelerations and coordinates are expressed in the frequency-domain. The transfer matrix \mathbf{H} contains transfer functions $h(s)$ that give the transformed response $X(s)$ for every input $f(s)$ at every DOF.

$$\begin{bmatrix} X_1(s) \\ X_2(s) \\ X_3(s) \\ \vdots \\ X_n(s) \end{bmatrix} = \begin{bmatrix} h_{11}(s) & h_{12}(s) & \dots & h_{1n}(s) \\ h_{21}(s) & \cdot & \dots & \cdot \\ \cdot & \cdot & \dots & \cdot \\ h_{n1}(s) & \cdot & \cdot & \cdot \end{bmatrix} \begin{bmatrix} f_1(s) \\ f_2(s) \\ f_3(s) \\ \cdot \\ f_n(s) \end{bmatrix} \quad (1.2.1-5)$$

The transfer functions, $h(x)$, are also of a complex nature. The real part corresponds to the magnitude and the imaginary part corresponds to the phase

shift of the response. For simplicity, let us once again consider a simple two-DOF system, keeping in mind that the statements made can be transferred to multiple-DOF systems as well.

In this case, the characteristic equation (CE) for the inverse of the frequency response matrix \mathbb{B} would be a polynomial of the degree $2n$ with n pairs of conjugate complex roots, p_k and p_k^* . Expressing the CE in terms of its roots we can write:

$$\text{Det } \mathbb{B} = C (s-p_1) (s-p_1^*) (s-p_2) (s-p_2^*) \dots (s-p_n) (s-p_n^*) \quad (1.2.1-6)$$

So, the components of the frequency response matrix can be written as

$$h_{ij}(s) = \frac{m_{ij} s^2 + d_{ij} s + k_{ij}}{\text{CE}} \quad (1.2.1-7)$$

A diagram representing the properties of the FRF and its connections to the DOFs is shown in Fig. 1.2.1-2. The input f_i as well as the outputs $x_1 \dots x_n$ are transformed (\Rightarrow) into the Laplace domain becoming F_i and $X_1 \dots X_n$. The magnitude and phase shift of the output in relationship to the input excitation is given by the FRF.

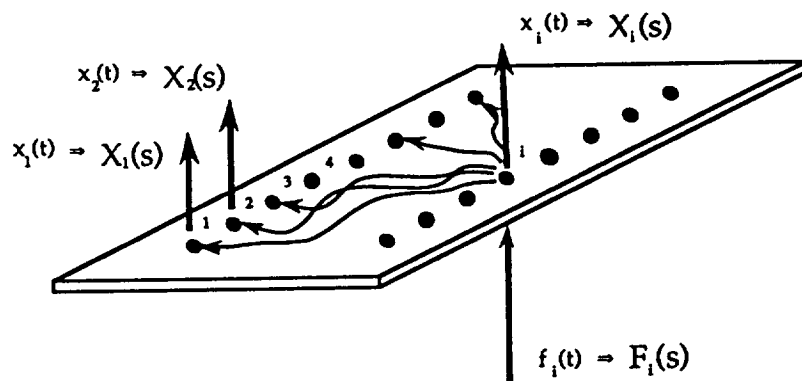


Fig 1.2.1-2 The Frequency Response Function

If we assume that the poles of \mathbf{H} , i.e. the roots of the CE of \mathbb{B} , are of multiplicity one for our physical system, we can expand the denominator³ and write

$$h_{ij}(s) = \sum_{k=1}^n \left[\frac{r_k}{(s-p_k)} + \frac{r_k}{(s-p_k^*)} \right] \quad (1.2.1-8)$$

$$p_k = \sigma_k + i \omega_k$$

σ_k = damping coefficient
 ω_k = nat. freq of oscillation

Examining the response matrix for one specific mode, k , the response functions h_{ij} all have the common denominator $\left[\frac{1}{(s-p_k)} + \frac{1}{(s-p_k^*)} \right]$ and differ only in the numerator, r_k . These *residues* r_k are the only parameters that vary along the structure and are collected in the residue matrix \mathbf{R}_k .

$$\mathbf{R}_k = \begin{bmatrix} r_{11} & r_{12} & \dots & r_{1n} \\ \cdot & \cdot & \dots & \cdot \\ r_{n1} & \cdot & \dots & \cdot \end{bmatrix} \quad (1.2.1-9)$$

implying that $\mathbf{H} = \frac{\mathbf{R}_k}{\text{const}}$ or $\mathbf{H}_k \sim \mathbf{R}_k$

The matrix of the system residues, just like the modal matrix, represent the motion of a structure when excited at a resonant frequency, both giving the amplitude and direction of the response at some DOF. Taking advantage of the symmetry inherent in the response matrix \mathbf{H} ($h_{ij} = h_{ji}$) we can make the connection to the modal matrix. This represents the experimental/analytical link of the modal analysis procedure.

$$\mathbf{R}_k = \mathbf{Q}_k \underline{u}_k \underline{u}_k^T \quad (1.2.1-10)$$

³ A polynomial $B(x)$ that is divided by a polynomial $A(x)$ can always be written in the partial fraction form

$$\frac{A(x)}{B(x)} = \frac{r_1}{s-p_1} + \frac{r_2}{s-p_2} + \dots + \frac{r_n}{s-p_n} + k(x) \quad , \quad (s-p_i) \text{ being the roots of } B$$

where Q_k is an arbitrary constant since the mode shapes are defined only in direction not magnitude.

Arbitrarily choosing the i -th column of the residue matrix, we can write (suppressing the index k for the moment, since we are examining only the transfer function for the k -th mode)

$$\begin{bmatrix} r_{1i} \\ r_{2i} \\ r_{3i} \\ \vdots \\ r_{ii} \\ \vdots \\ \vdots \\ r_{ni} \end{bmatrix} = Q \begin{bmatrix} u_1 u_i \\ u_2 u_i \\ u_3 u_i \\ \vdots \\ u_i u_i \\ \vdots \\ \vdots \\ u_n u_i \end{bmatrix} = Q u_i \underline{u} \quad (1.2.1-10)$$

We can calculate the residue for the driving point (structure excitation point), r_{ii}

$$r_{ii} = Q u_i u_i = Q u_i^2 \quad (1.2.1-11)$$

or

$$u_i = \left(\frac{r_{ii}}{Q} \right)^{0.5} \quad (1.2.1-12)$$

which delivers the proportionality factor of the two matrices. Thus, as long as a driving point measurement is made and this driving point does not correspond to a node of the examined mode, the entire residue matrix can be constructed by measuring only one row or column of the transfer matrix, i.e. knowledge of one mode.

2. Modeling the Beam by the Finite Element Method

2.1 Introduction

Since a wealth of data concerning the vibrations of a cantilever beam exists (Ref. 2.-1,6,11,12), a finite element model for the boundary conditions clamped-free was written. Once a sufficient accuracy was determined, this model could be altered to encompass other boundary conditions of a vibrating system, i.e. hinged-free or free-free.

Because the algorithm for predicting the rotating mode shapes (see section 2.3.1) relies heavily on the slopes or derivatives of the eigenform of the non-rotating mode shape of the beam, these slopes were compared with those given in Ref. 2.-1 and Ref. 2.-2. After verifying the accuracy of the non-rotating model, an extension of the method of Ref. 2.-3 using the finite element method was applied, and the results for the rotating model were compared to the exact solution of Ref. 2.-2 - a 5 mode extension for a cantilevered Beam and a 6 mode extension in the case of a hinged beam.

The beam is divided into n elements and a stiffness and mass matrix is derived for each single element. These element matrices are then assembled into a system matrix, taking into account the boundary conditions. In this case the continuous mass distribution is replaced by a lumped parameter mass distribution, which means that each end (or node) of the element is assigned half the finite element mass.

2.1.1 The Element Stiffness Matrix

The element stiffness matrix, \mathbf{k} , expresses the relationship between static forces and moments, \underline{P} , and linear and angular displacements, $\underline{\delta}$:

$$\underline{P} = \mathbf{k} \underline{\delta} \quad (2.1.1-1)$$

A beam segment or element with the properties shown in Fig. 2.1.1-1 has four degrees of freedom, a linear and an angular one at each node.

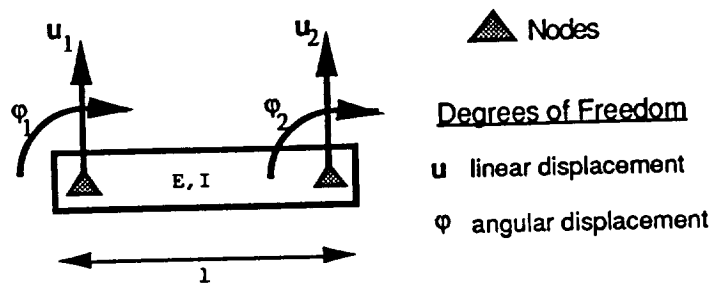


Fig. 2.1.1-1 BEAM Element

The element stiffness matrix is derived in detail in Ref. 2.-4 using the principle of virtual deflection and found to be

$$\mathbf{k} = \frac{EI}{l^3} \begin{bmatrix} 12 & -6l & -12 & -6l \\ -6l & 4l^2 & 6l & l^2 \\ -12 & 6l & 12 & 6l \\ -6l & l^2 & 6l & 4l^2 \end{bmatrix} \quad (2.1.1-2)$$

(4x4)

2.1.2 The Element Mass Matrix

Following the lumped mass distribution assumption, the inertia associated with each rotational degree of freedom is assumed to be zero while the mass of each element is assigned evenly to the nodes. This distribution of the mass is shown in Fig. 2.1.2-1.

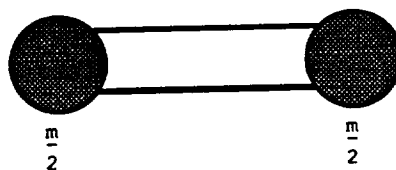


Fig. 2.1.2-1 Lumped Mass Distribution

Thus, the element mass matrix can be written as

$$\mathbf{m} = \begin{bmatrix} \frac{m}{2} & 0 & 0 & 0 \\ 0 & 0 & 0 & 0 \\ 0 & \frac{m}{2} & 0 & 0 \\ 0 & 0 & 0 & 0 \end{bmatrix} \quad (2.1.2-1)$$

2.1.3 Assembly of the Structure Stiffness Matrix

The stiffness matrix of the structure, in our case a beam consisting of n finite elements, is assembled by identifying the degrees of freedom at each element node, numbering them in a consistent manner and simply adding those contributing to the same system degree of freedom. This is what is known as the *direct method*. For an homogeneous cantilever beam with a constant cross-section (we will call this sort of beam simply "constant"), this assembly process is demonstrated in Fig. 2.1.3-1. For a cantilever beam, the boundary conditions are $\phi_1 = 0$ and $u_1 = 0$.

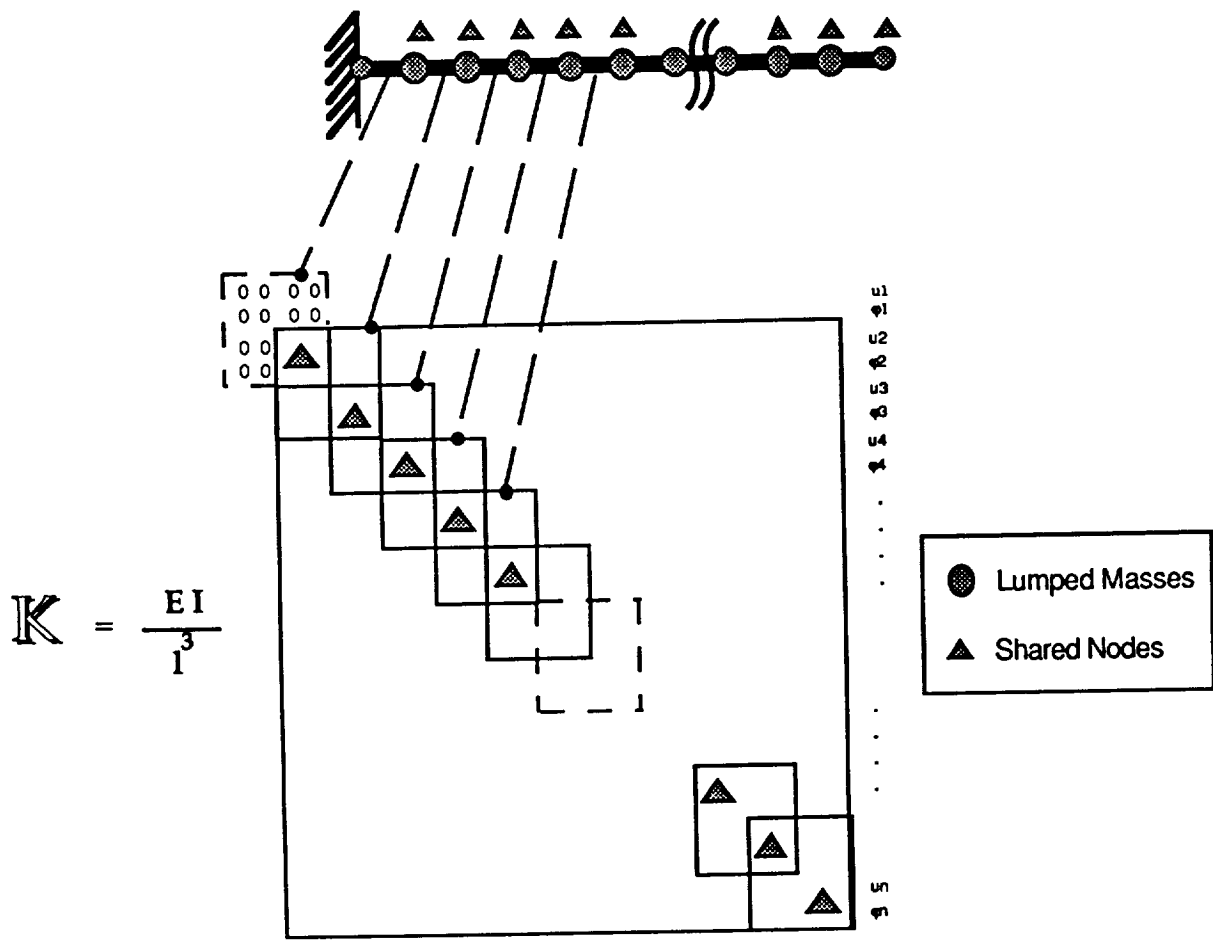


Fig. 2.1.3-1 Assembly of the Stiffness Matrix

The *system* stiffness matrix relates the forces and the displacements at the *system* nodal coordinates in the same way as the *element* stiffness matrix relates them in the *element* nodal coordinates. The rules governing the assembly process for the

eigenproblem. The reduction of massless or inertialess degrees of freedom introduces no error.

The reduction of the stiffness matrix is somewhat involved, but can nonetheless be easily accomplished. First, we permute the rows and columns in the stiffness matrix such that the displacement and rotational degrees of freedom are adjacent to each other. This leads us to a stiffness matrix with rearranged rows and columns, \mathbf{K}_{re} that can be partitioned as follows:

$$\mathbf{K}_{re} = \begin{bmatrix} \mathbf{K}_{uu} & \mathbf{K}_{u\phi} \\ \mathbf{K}_{\phi u} & \mathbf{K}_{\phi\phi} \end{bmatrix} \begin{matrix} \vdots \\ \vdots \end{matrix} \quad (2.1.5-1)$$

So that now the equations of motion can be written as

$$\begin{bmatrix} \mathbf{m} & \mathbf{0} \\ \mathbf{0} & \mathbf{0} \end{bmatrix} \begin{bmatrix} \ddot{\mathbf{u}} \\ \ddot{\boldsymbol{\phi}} \end{bmatrix} + \begin{bmatrix} \mathbf{K}_{uu} & \mathbf{K}_{u\phi} \\ \mathbf{K}_{\phi u} & \mathbf{K}_{\phi\phi} \end{bmatrix} \begin{bmatrix} \mathbf{u} \\ \boldsymbol{\phi} \end{bmatrix} = \begin{bmatrix} \mathbf{P}_u \\ \mathbf{0} \end{bmatrix} \quad (2.1.5-2)$$

The lower part of this matrix equation gives us

$$\mathbf{K}_{\phi u} \mathbf{u} + \mathbf{K}_{\phi\phi} \boldsymbol{\phi} = \mathbf{0} \quad (2.1.5-3)$$

or

$$\begin{bmatrix} \mathbf{u} \\ \boldsymbol{\phi} \end{bmatrix} \begin{bmatrix} \mathbf{K}_{\phi u} \\ \mathbf{K}_{\phi\phi} \end{bmatrix} = \begin{bmatrix} \mathbf{0} \\ \mathbf{0} \end{bmatrix} \quad (2.1.5-4)$$

as the equation of constraint. Thus, the rotational and translational degrees of freedom can be related to each other as

$$\boldsymbol{\phi} = -\mathbf{K}_{\phi\phi}^{-1} \mathbf{K}_{\phi u} \mathbf{u} \quad (2.1.5-5)$$

Setting

$$\mathbf{T}_{\phi u} = -\mathbf{K}_{\phi\phi}^{-1} \mathbf{K}_{\phi u} \quad (2.1.5-6)$$

the transformation equation becomes

$$\begin{bmatrix} \underline{u} \\ \underline{\phi} \end{bmatrix} = \begin{bmatrix} \mathbf{I} \\ \mathbf{T}_{\phi u} \end{bmatrix} \underline{u} = \mathbf{T} \underline{u} \quad (2.1.5-7)$$

Now, the rearranged \mathbf{K}_{re} and \mathbf{M}_{re} matrices can be reduced in dimension by the transformation matrix \mathbf{T} to

$$\hat{\mathbf{M}} = \mathbf{T}^t \mathbf{M}_{re} \mathbf{T} \quad (2.1.5-8a)$$

$$\hat{\mathbf{K}} = \mathbf{T}^t \mathbf{K}_{re} \mathbf{T} \quad (2.1.5-8b)$$

The mass matrix is reduced, in the case of lumped masses, simply by deleting those rows and columns that pertain to the rotating degrees of freedom.

or

$$\hat{\mathbf{M}} = \mathbf{M}_{re} \quad (2.1.5-9a)$$

$$\hat{\mathbf{K}}_{uu} = \mathbf{K}_{uu} - \mathbf{K}_{\phi u}^t \mathbf{K}_{\phi\phi}^{-1} \mathbf{K}_{\phi u} \quad (2.1.5-9b)$$

The rearranged mass matrix, \mathbf{M}_{re} , remains essentially unchanged by the reduction, while the stiffness matrix is transformed to the *reduced stiffness matrix* $\hat{\mathbf{K}}_{uu}$. The eigenvalue problem

$$(\hat{\mathbf{K}}_{uu} - \lambda \mathbf{M}_{re}) \phi = 0 \quad (2.1.5-10)$$

can now be solved using the available algorithms.

2.1.6 Treatment of Singular Matrices

A beam with one end free and the other end hinged represents a statically undetermined system, and the system stiffness matrix assembled using the finite element method is singular. A singular matrix cannot be inverted. In addition, the numerical size of the elements of the mass and stiffness matrix differ by a large factor that increases with the degree of discretisation. The above factors contribute to the danger of numerical difficulties in solving the eigenproblem. To circumvent these numerical problems, the mass and stiffness matrices were divided by their norm, and the equivalent eigenproblem was solved to obtain the eigenvectors and eigenvalues .

The norm of a matrix \mathbf{A} is defined as

$$\|\mathbf{A}\| = (\det(\mathbf{A} \mathbf{A}^t))^{1/2} \quad (2.1.6-1)$$

Dividing a matrix by its norm in this case yields a numerically well-conditioned matrix. Applying this to the eigenproblem results in

$$\det[\mathbf{K}' - \eta \mathbf{M}'] = 0 \quad (2.1.6-2)$$

with

$$\mathbf{K}' = \frac{\mathbf{K}}{\|\mathbf{K}\|} \quad \mathbf{M}' = \frac{\mathbf{M}}{\|\mathbf{M}\|} \quad \eta = \lambda \frac{\|\mathbf{M}\|}{\|\mathbf{K}\|} \quad (2.1.6-3)$$

After solving for λ , we reinsert the eigenvalues (one of them being zero; corresponding in this case to the rigid body mode of the hinged beam) into the eigenproblem (2.1.5-10). The n -th eigenvector can now be found by inserting the n -th eigenvalue into the eigenproblem:

Inserting $\lambda_i = \lambda_n$ into

$$(\mathbf{K} - \lambda_i \mathbf{I} - \mathbf{M}) \phi_i = \mathbf{A} \phi_i = 0 \quad (2.1.6-4)$$

where ϕ_i is the eigenvector corresponding to λ_i , and decomposing \mathbf{A} into the matrices \mathbf{P} and \mathbf{P}^{-1} and the diagonal matrix \mathbf{D}

$$\mathbf{A} = \mathbf{P} \mathbf{D} \mathbf{P}^{-1} \quad (2.1.6-5)$$

we can write

$$\mathbf{D} \mathbf{P}^{-1} \phi = 0 \quad (2.1.6-6)$$

Defining

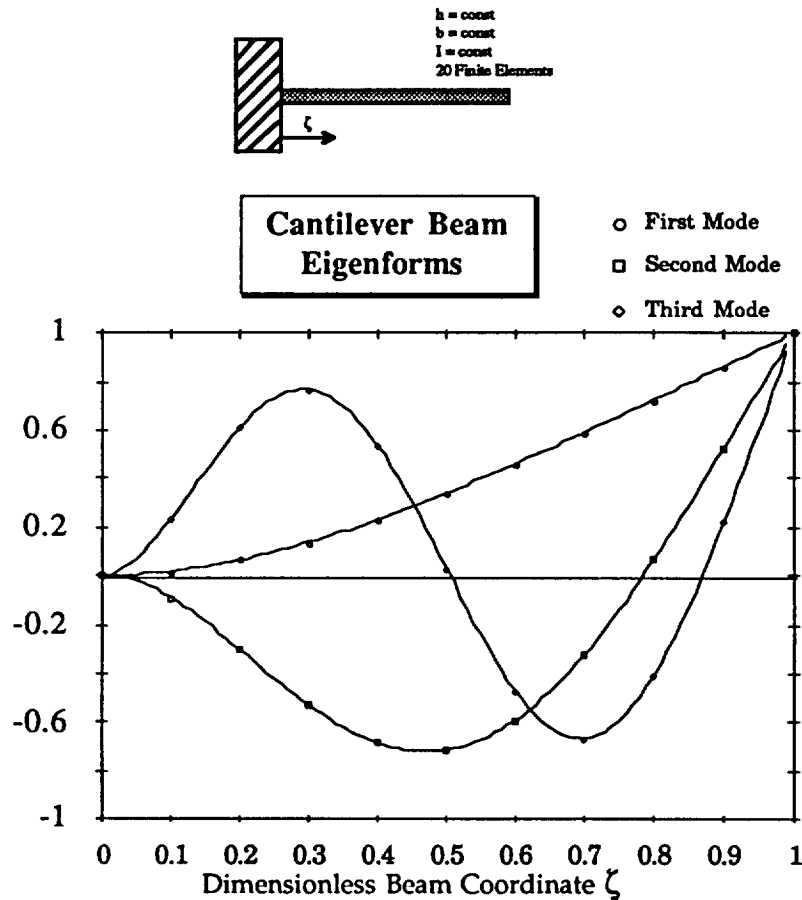
$$\underline{y} := \mathbf{P}^{-1} \phi \quad (2.1.6-7)$$

it follows that

$$\mathbf{D} \underline{y} = 0 \quad (2.1.6-8)$$

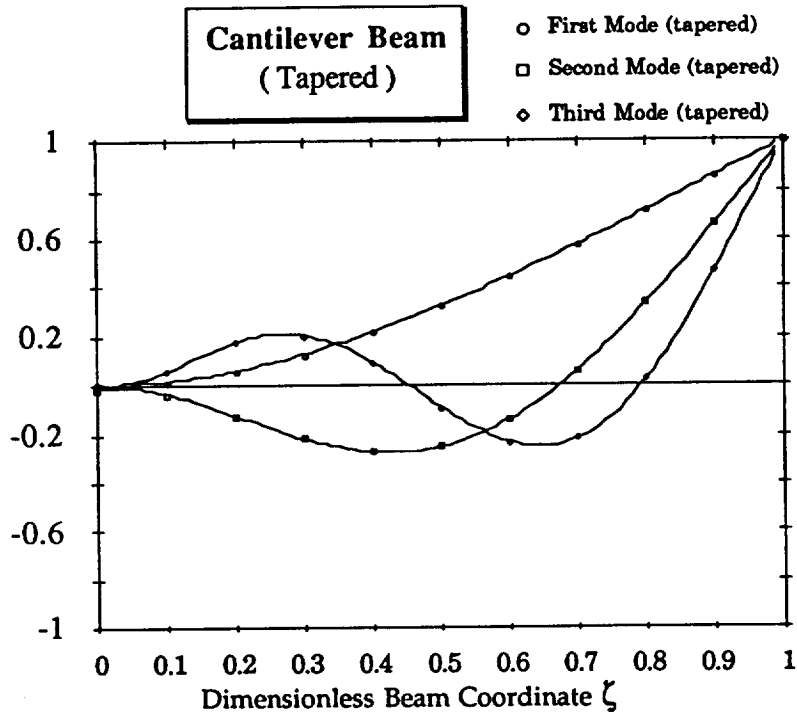
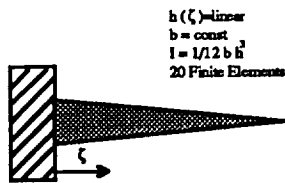
2.2 Results of the Non-Rotating (Static) Analysis

Calculations were performed on cantilever and hinged beams, having both constant and tapering stiffness and height distributions. Results are presented for tapered and constant cantilevered and hinged beams in Figs. 2.2-1 to 2.2-4.



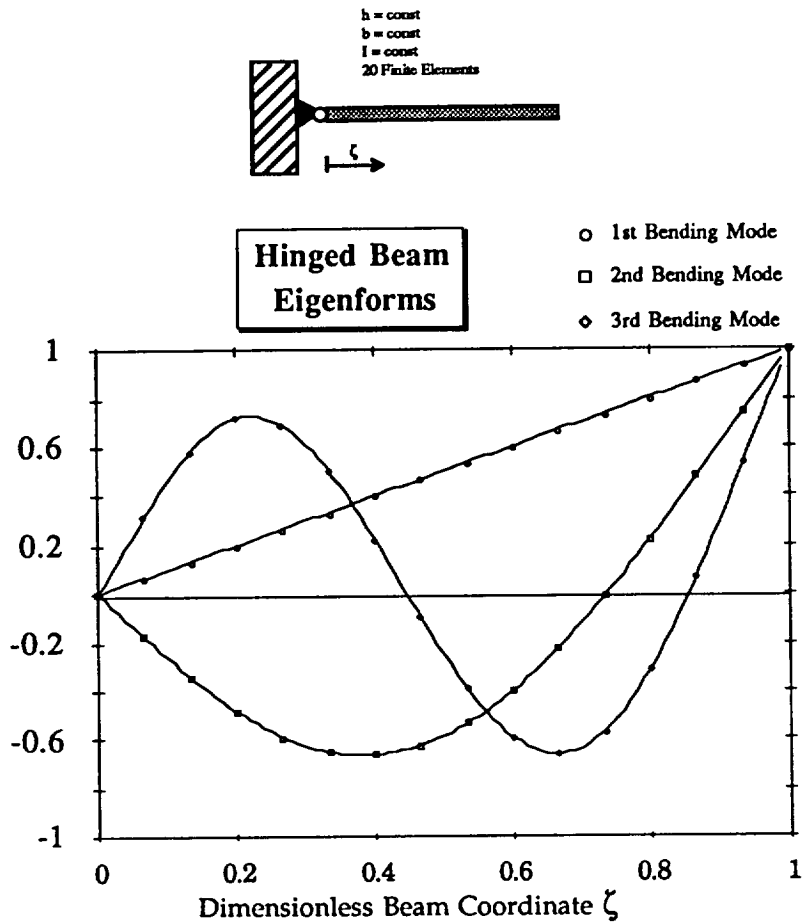
Coord	First Mode	Second Mode	Third Mode
0.0	0.00000	0.00000	0.00000
0.1	0.0167628	-0.0928322	0.229821
0.2	0.0638290	-0.301486	0.610493
0.3	0.136403	-0.527415	0.767384
0.4	0.229766	-0.685807	0.537735
0.5	0.339372	-0.717123	0.0292471
0.6	0.460966	-0.594037	-0.471250
0.7	0.590711	-0.322196	-0.666258
0.8	0.725340	0.0654301	-0.410146
0.9	0.862316	0.520821	0.216292
1.0	1.00000	1.00000	1.00000

Fig. 2.2-1 Mode shapes and Coordinates of the Cantilevered, Constant Beam



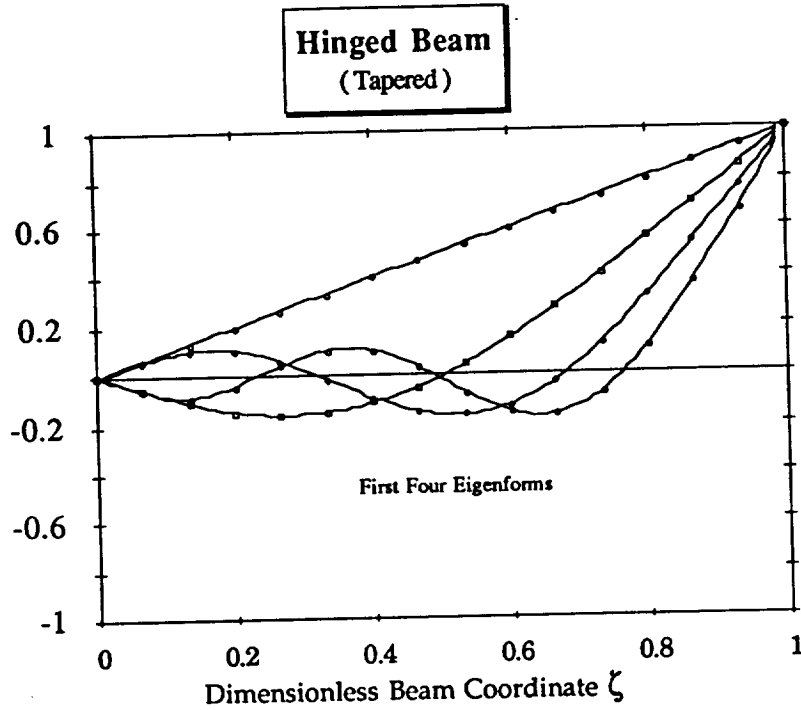
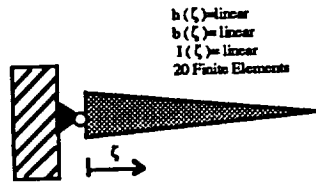
Coor	First Mode (tapered)	Second Mode (tapered)	Third Mode (tapered)
0.0	0.00154295	-0.0156330	0.00672200
0.1	0.0147688	-0.0360000	0.0565879
0.2	0.0577830	-0.125706	0.174609
0.3	0.126396	-0.220433	0.201682
0.4	0.216554	-0.272842	0.0921422
0.5	0.324336	-0.251821	-0.0906786
0.6	0.445950	-0.141774	-0.232354
0.7	0.577741	0.0581017	-0.218733
0.8	0.716185	0.334526	0.0192293
0.9	0.857889	0.660860	0.467178
1.0	1.00000	1.00000	1.00000

Fig. 2.2-2 Mode shapes and Coordinates of the Cantilevered, Tapered Beam



Coordinate	First Mode Rigid Body	Second Mode	Third Mode	Fourth Mode
0.00000	0.00000	0.00000	0.00000	0.00000
0.066667	0.066667	-0.176168	0.312006	-0.427397
0.133333	0.133333	-0.342705	0.581464	-0.734409
0.200000	0.200000	-0.484881	0.717196	-0.664977
0.266667	0.266667	-0.590631	0.687227	-0.283391
0.333333	0.333333	-0.651757	0.507443	0.203671
0.400000	0.400000	-0.663542	0.224895	0.580202
0.466667	0.466667	-0.624366	-0.0968230	0.701849
0.533333	0.533333	-0.535326	-0.390120	0.532819
0.600000	0.600000	-0.399852	-0.593871	0.146648
0.666667	0.666667	-0.223324	-0.661815	-0.301164
0.733333	0.733333	-0.0129609	-0.568864	-0.620699
0.800000	0.800000	0.223915	-0.315344	-0.647359
0.866667	0.866667	0.477577	0.0708468	-0.305840
0.933333	0.933333	0.738882	0.534149	0.329654
1.00000	1.00000	0.998499	0.993338	0.986899

Fig. 2.2-3 Mode shapes and Coordinates of the Hinged, Constant Beam



Coord	First Mode rigid body	Second Mode	Third Mode	Fourth Mode
0.00000	0.00000	0.00000	0.00000	0.00000
0.066666	0.0666667	-0.0567526	0.0582599	-0.0548090
0.133333	0.133333	-0.108299	0.102849	-0.0847653
0.200000	0.200000	-0.144760	0.103761	-0.0385510
0.266667	0.266667	-0.159416	0.0594524	0.0438681
0.333333	0.333333	-0.148481	-0.0140151	0.102800
0.400000	0.400000	-0.110661	-0.0921840	0.0993520
0.466667	0.466667	-0.0466947	-0.149522	0.0312482
0.533333	0.533333	0.0410851	-0.164856	-0.0696861
0.600000	0.600000	0.149206	-0.124921	-0.151979
0.666667	0.666667	0.273503	-0.0260174	-0.164524
0.733333	0.733333	0.409567	0.126213	-0.0757709
0.800000	0.800000	0.553193	0.318904	0.114303
0.866667	0.866667	0.700830	0.539640	0.375812
0.933333	0.933333	0.850027	0.763966	0.670562
1.00000	1.00000	1.00000	1.00000	1.00000

Fig. 2.2-4 Mode shapes and Coordinates of the Hinged, Tapered Beam

2.3 Prediction of the Rotating Natural Frequencies

2.3.1 Predicting the Bending Frequencies of a Rotating Beam given the Non-Rotating Bending Frequencies.

To verify the accuracy of the mathematical rotor blade model described in section 2.2. , we will compare the results of that simulation to those obtained by a different approach for beams with well known geometric properties and later for the Blackhawk rotorblade itself. Since the non-rotating bending frequencies of the Blackhawk rotor blade with free-free boundary conditions are known from the shake test (Ref. 2.-7), we will use a Lagrangian method suggested by Ref. 2.-3 to predict the rotating frequencies and modes. This approach allows us to determine the rotating bending frequencies for any rotational speed, given only the structural properties of the rotor blade or beam that is to be analyzed. There is no restriction as to the stiffness or mass distribution. Only the stiffness and mass matrices must be assembled in order to determine the non-rotating mode shapes or eigenvectors. Both Loewy (Ref. 2.-3) and Yntema (Ref. 2.-2) make the simplifying assumption that a linear height distribution leads to both a linear mass and a linear stiffness distribution. Using the finite element approach will allow us to negate this simplification and calculate beams or systems with a *truly* linear height distribution (resulting in a cubic stiffness distribution) and systems with a *truly* linear stiffness distribution (resulting in a third-root height distribution). As we will see, the calculations using this more exact approach will improve upon the accuracy of the previous results.

The bending deflections of the rotating mode will be expressed in terms of the deflections of the non-rotating modes

$$\underline{w}_i(t) = \sum_n \underline{u}_i^{(n)} q(t)_n \quad (2.3.1-1)$$

where

$\underline{w}_i(t)$ = the i-th rotating mode shape vector

$\underline{u}_i^{(n)}$ = the n-th non-rotating mode shape

$q(t)_n$ =the time and amplitude dependency of the n-th non-rotating mode (and thus also the n-th generalized coordinate in the Lagrangian approach)

Following (Ref. 2.-3) , the kinetic energy terms are expressed as

$$T = \frac{1}{2} \sum_i \left(\dot{\bar{x}}^T \dot{\bar{x}} m_i \right) \quad (2.3.1-2)$$

and after the differentiations demanded by Lagrange's equation

$$\frac{\partial}{\partial t} \left(\frac{\partial T}{\partial \dot{q}_r} \right) - \left(\frac{\partial T}{\partial q_r} \right) + \left(\frac{\partial U}{\partial q_r} \right) = 0 \quad (2.3.1-3)$$

these kinetic terms turn out to be

$$M_{gen} \ddot{q} \quad (2.3.1-4)$$

where M_{gen} is the generalized mass matrix obtained from the static (non-rotating) analysis of the beam, and \ddot{q}_i is the second derivative with respect to time of the generalized coordinate.

The potential energy terms are divided into two parts. The first, U_1 , represents the potential energy stored in the beam due to deformation (elastic properties) and the second, U_2 , represents the work done by centrifugal forces on the lumped masses, m_i , acting through changes in the radial position, x_i , of these masses as the blade bends. This "shortening" Δ_i of the blade at the radial position x_i along the beam coordinate x_0 can be expressed as

$$\Delta_i = \frac{1}{2} \int_0^{x_{oi}} \left(\frac{\partial w_i}{\partial x_0} \right)^2 dx_0 \quad (2.3.1-5)$$

The expression for Δ_i is derived and discussed at length in Ref. 2.-5. The shortening can be approximated with the the following summation:

$$\Delta_i = \frac{1}{2} \sum_{j=1}^i \left(\frac{\partial w_i}{\partial x_o} \right)_j^2 \Delta x_{oj} \quad (2.3.1-6)$$

where $j = 1$ is the position at the root of the beam.

Inserting the above expressions into the potential energy terms

$$U_1 = \frac{1}{2} \sum_n \mathbb{K}_{gen} q^2 \quad (2.3.1-7)$$

$$U_2 = \sum_i m_i x_{oi} \Omega^2 \Delta_i \quad (2.3.1-8)$$

and considering that

$$\mathbb{K}_{gen} = \omega^2 \mathbb{M}_{gen} = \omega^2 \sum_i m_i w_i^{(n)2} \quad (2.3.1-9)^1$$

we obtain the equation for the r -th generalized coordinate (the r -th row of the rotating beam equation) as

$$\mathbb{M}_{gen}^{(r)} \ddot{q}_r + \Omega^2 \sum_i m_i x_{oi} \sum_{j=1}^i q_r \left(\frac{\partial w^{(n)}}{\partial x_o} \right)_j^2 \left(\frac{\partial w^{(r)}}{\partial x_o} \right)_j^2 \Delta x_{oj} + \mathbb{K}_{gen} q_r = 0 \quad (2.3.1-10)$$

Substituting

$$\gamma_{rn} = \sum_i m_i x_{oi} \sum_{j=1}^i \left(\frac{\partial w^{(n)}}{\partial x_o} \right)_j^2 \left(\frac{\partial w^{(r)}}{\partial x_o} \right)_j^2 \Delta x_{oj} \quad (2.3.1-11)$$

yields

$$\mathbb{M}_{gen} \ddot{q} + \Omega^2 \gamma q + \mathbb{K}_{gen} q = 0 \quad (2.3.1-12)$$

The term $\mathbb{K}_{stat} = \mathbb{K}_{gen}$ is the static or non-rotating part of the beams stiffness matrix, and $\mathbb{K}_{dyn} = \Omega^2 \gamma$ is the dynamic part of the stiffness matrix brought on by the centrifugal forces on the lumped masses.

Adding \mathbb{K}_{stat} and \mathbb{K}_{dyn} leads to the well-known problem

¹ if the condition that M is diagonal holds

$$\mathbf{M} \ddot{\mathbf{q}} + \mathbf{K} \mathbf{q} = \mathbf{0} \quad (2.3.1-13)$$

that can be solved by the usual algorithms to obtain the rotating beam modes.

Taking into account the first 5 non-rotating beam modes of a beam subdivided into 20 lumped masses, we obtain a \mathbf{K}_{dyn} that is populated in the upper left hand corner (5x5) with the elements

$$\gamma_{ij} \quad (\text{with } i,j=1\dots 5)$$

2.3.2 Linear Height and Stiffness Distributions

Calculations to verify the algorithm prior to applying it to the UH-60 rotor blade were done for the following examples in order to gain some insight into the order of accuracy. These results were compared to the results of a 5-mode extension performed in Ref. 2-2 for cantilever and hinged beams of constant and linear varying stiffness distributions. As stated earlier, the five and six mode extensions were based upon the assumption that a linear height distribution implied a linear mass *and* a linear stiffness distribution. This analysis introduces results for *truly* linear distributions of the above parameters. For example, the results obtained in Ref. 2-3 are for a beam of linear varying *height* taken from the book by Bisplinghoff Ref. 2-6 whereas the results are compared to those of Yntema (Ref. 2-2), who only examines beams of a constant or linearly varying *stiffness* distribution. The height function of the beam found in Ref. 2-6 is

$$h(\bar{x}) = 2b(1 - \lambda \bar{x}) \quad (2.3.2-1)$$

with $\lambda = 0.2$. Therefore the stiffness is :

$$I = \frac{1}{12} b h^3 = \frac{1}{12} b^2 (1 - \lambda \bar{x})^3 \quad (2.3.2-2)$$

where $\bar{x} = \frac{x}{L}$ is the dimensionless blade coordinate.

The stiffness will only be linear if the higher terms of \bar{x} can be dropped. This cannot be supported for a value of $\lambda = 0.2$. Thus, a height-variation producing a *truly linear* stiffness distribution was used in our examples. Also, in the hopes of obtaining a better estimate for the rotating modes, the first five non-

rotating mode shapes were included, instead of only the first two as in Ref. 2-3. Because the algorithm uses the slopes of the non-rotating mode shapes, the possibility of using a polynomial to obtain the derivatives instead of numerically calculating the slopes by a three-point and five-point differentiation rule was addressed, since a sufficiently exact polynomial can easily be fitted to the first five mode shape vectors. This did, in fact give a better approximation of the slope of the beam at the lumped mass in question, but, as pointed out in Ref. 2-3, the number of mass stations makes a far greater contribution to the convergence of the algorithm towards the correct solution than improving the accuracy of the derivatives.

2.3.3 Determining the Rotating Mode Shapes

After having determined the rotating frequencies by the addition of the dynamic stiffness matrix expressed in terms of the generalized system equations it becomes necessary to do a back-transformation prior to obtaining the mode shapes for the rotating system in the usual Cartesian system coordinates. We will use lowercase to indicate the generalized coordinates and uppercase to indicate the system (Cartesian) coordinates.

We can express the rotating system stiffness matrix, \mathbf{k}_{syst} , in generalized coordinates

$$\mathbf{k}_{\text{syst}} = \mathbf{k}_{\text{gen}} + \mathbf{k}_{\text{dyn}} \quad (2.3.3-1)$$

The diagonalized stiffness matrix, \mathbf{k}_{gen} , was found by transforming the static stiffness matrix, \mathbf{K}_{stat} , by the *system modal matrix*, \mathbf{U} , a matrix composed of the eigenvectors² obtained while solving (2.3.1-13)

$$\mathbf{k}_{\text{gen}} = \mathbf{U}^T \mathbf{K}_{\text{stat}} \mathbf{U} \quad (2.3.3-2)$$

Inserting (2.3.3-1) into (2.3.3-2) we get

² since \mathbf{U} is composed of the eigenvectors of our vibratory system arranged in columns, and these eigenvectors have been normalized prior to placing them into \mathbf{U} , we have an orthonormal matrix. The transformation equation $\mathbf{U}^{-1} \mathbf{K} \mathbf{U}$ can be simplified to $\mathbf{U}^T \mathbf{K} \mathbf{U}$, since $\mathbf{U}^{-1} = \mathbf{U}^T$ for orthonormal Matrices.

$$\mathbf{k}_{\text{syst}} = \mathbf{U}^T \mathbf{K}_{\text{stat}} \mathbf{U} + \mathbf{k}_{\text{dyn}} \quad (2.3.3-3)$$

Transforming (2.3.3-3) into Cartesian coordinates with the system matrix, \mathbf{U} , gives us

$$(\mathbf{U}^T)^{-1} \mathbf{k}_{\text{syst}} (\mathbf{U})^{-1} = \mathbf{K}_{\text{stat}} + (\mathbf{U}^T)^{-1} \mathbf{k}_{\text{dyn}} (\mathbf{U})^{-1} \quad (2.3.3-4)$$

or

$$\mathbf{K}_{\text{syst}} = \mathbf{K}_{\text{stat}} + \mathbf{K}_{\text{dyn}} \quad (2.3.3-5)$$

To find the rotating eigenvectors, we must solve the equation

$$\mathbf{M} \ddot{\mathbf{q}} + \mathbf{K}_{\text{syst}} \mathbf{q} = 0 \quad (2.3.3-6)$$

that leads to a new system matrix, \mathbf{U}_{rot} , that is composed of the rotating eigenvectors. This new system matrix diagonalizes the rotating stiffness matrix, \mathbf{K}_{syst} :

$$\mathbf{U}_{\text{rot}}^T \mathbf{K}_{\text{syst}} \mathbf{U}_{\text{rot}} = \mathbf{k}_{\text{gen,rot}} \quad (2.3.3-7)$$

The rotating and non-rotating normalized deflection curves of a cantilever constant beam for the 1st to 3rd natural frequencies are shown in Fig. 2.3.3-1. For the hinged constant beam these are shown in Fig. 2.3.3-2. The rotational parameter

$$\Psi = \left(\frac{\Omega}{\omega_{n1}} \right)^2 \quad (2.3.3-8)$$

was set at 4 for the cantilever beam and at 2 for the hinged beam. It is seen that the discrepancies between the non-rotating and the rotating mode shapes are small, and that the nodes are virtually coincident.

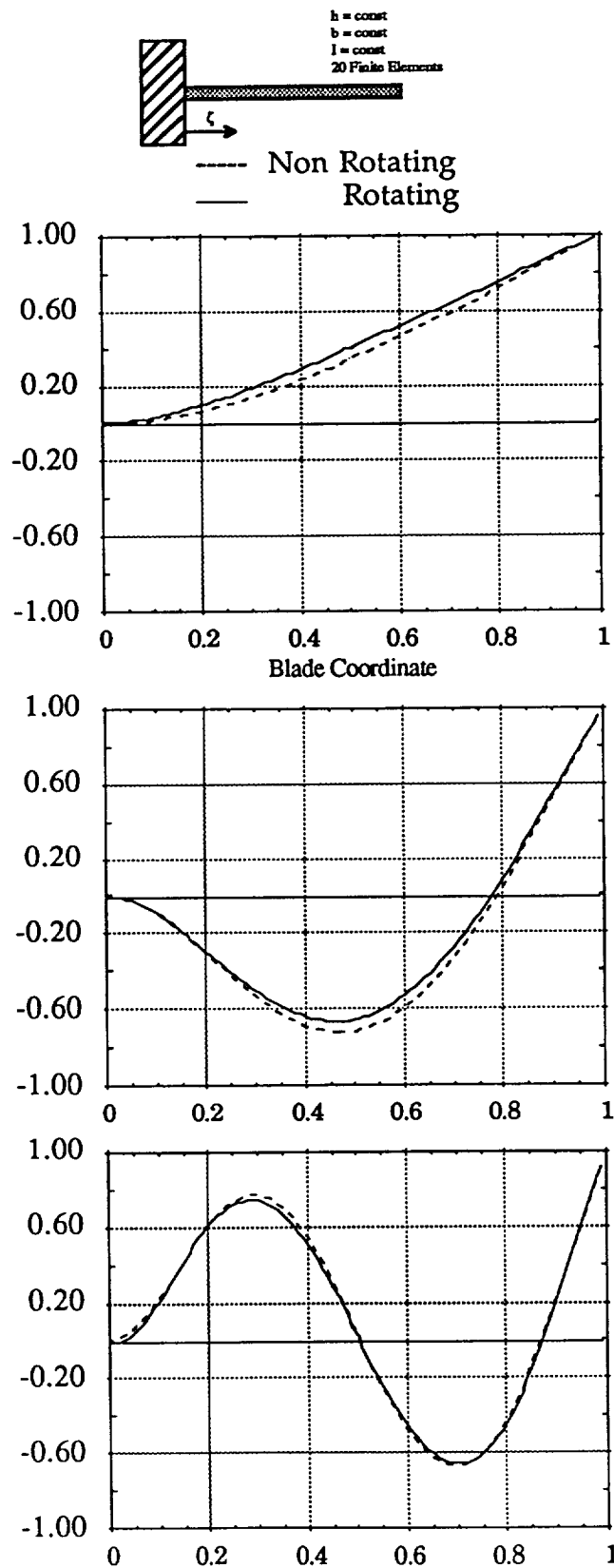


Fig. 2.3.3-1 Rotating/Non-Rotating Cantilever, Constant Beam

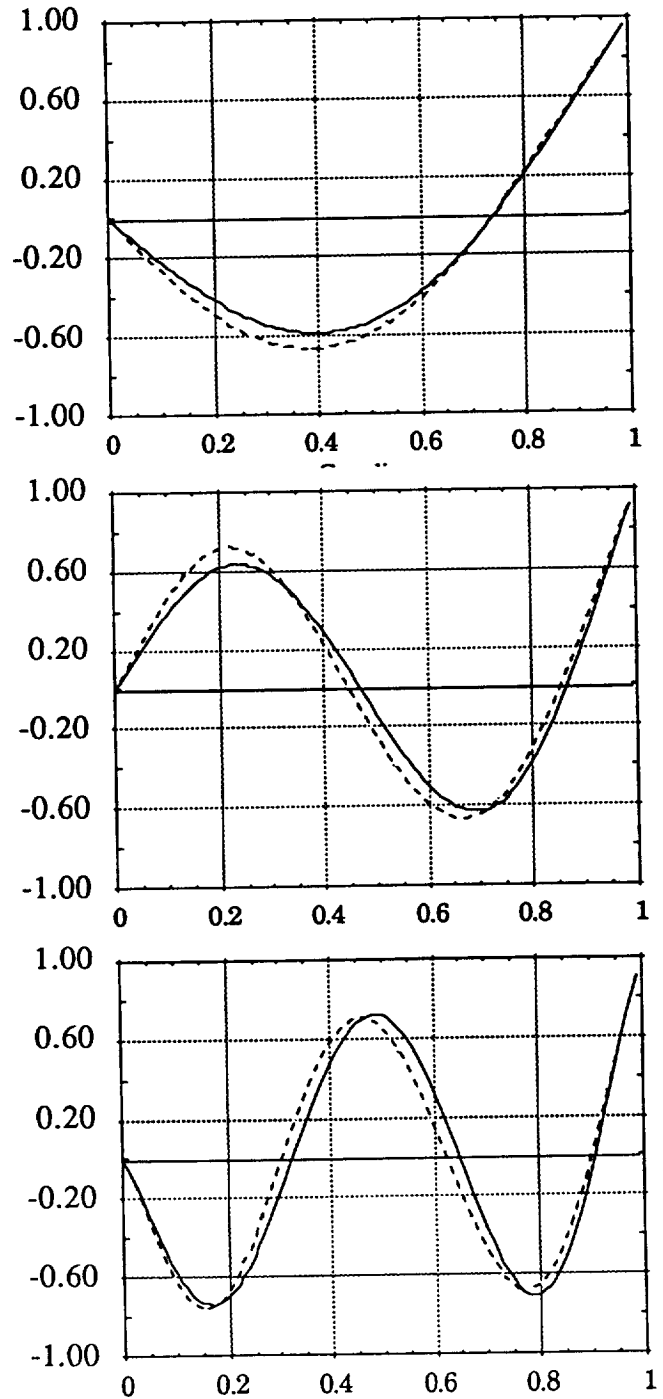
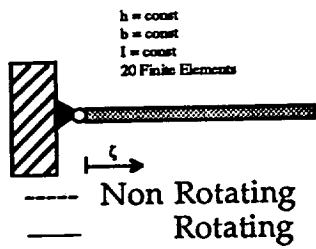


Fig. 2.3.3-2 Rotating/Non-Rotating Hinged, Constant Beam

2.3.4 Natural Frequency as a Function of Rotational Speed

Figs. 2.3.4-1 to 2.3.4-4 give an overview in how the natural frequencies increase with increasing rotational speeds. The factor Ψ relates the square of the first non-rotating frequency ω_{n1} to the square of the frequency that the system is rotated at, Ω . This parameter stays the same, regardless of which mode is being examined.

$$\Psi = \left(\frac{\Omega}{\omega_{n1}} \right)^2 \quad (2.3.3-7)$$

The factor for the abscissa, Φ , shows the magnitude of the change in rotating to non-rotating natural frequency. The denominator of this parameter always holds the non-rotating natural frequency of the mode being examined, ω_{ni} .

$$\Phi = \left(\frac{\omega_{rot i}}{\omega_{n i}} \right)^2 \quad (2.3.4-1)$$

The parameters are squared in order to better assess the reliability of the obtained results when comparing them to Ref. 2.-3. Notice that squaring the parameter also squares the error. The diagram for the cantilever beam with non-constant height distributions (Fig. 2.3.4-2), reaffirms the previously stated concerns. Only when a beam is considered that has a linear height distribution *and* a linear stiffness distribution are examined, does one receive the results stated by Yntema (Ref. 2.-2). This form of beam, having both a linear mass distribution as well as a linear stiffness distribution does not exist for isotropic structures.

The frequency graph for the "tapered" cantilever beam (Fig. 2.3.4-4) shows the frequency increases for a beam of actual linearly decreasing height and linearly decreasing stiffness at a constant width.

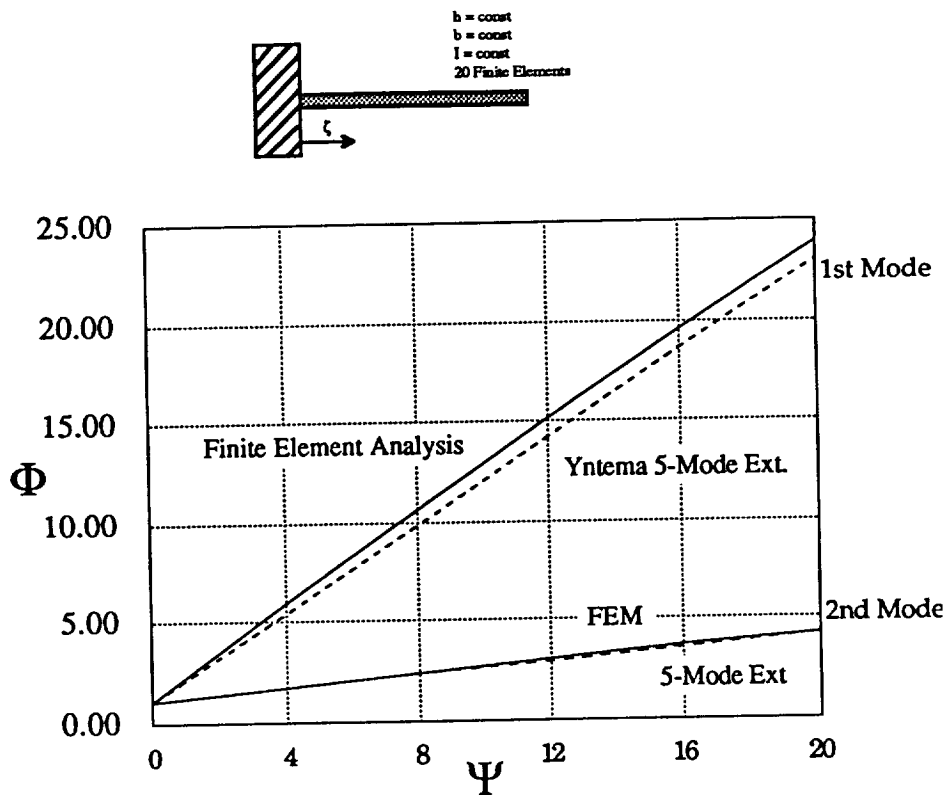


Fig. 2.3.4-1 Rotating, Cantilever Constant Beam

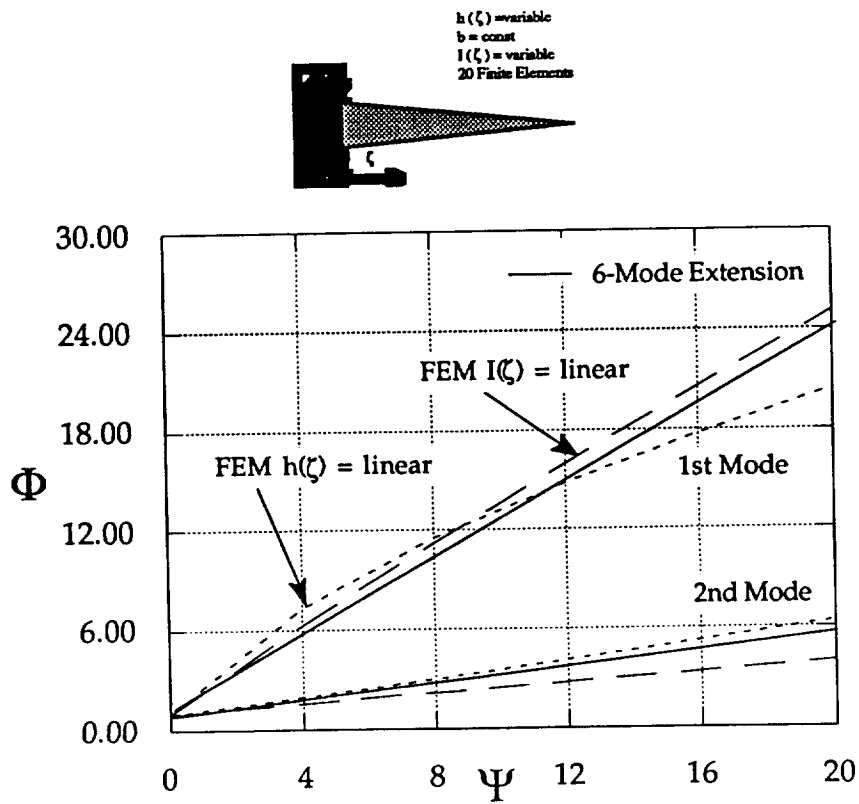


Fig. 2.3.4-2 Rotating, Cantilever Tapered Beam

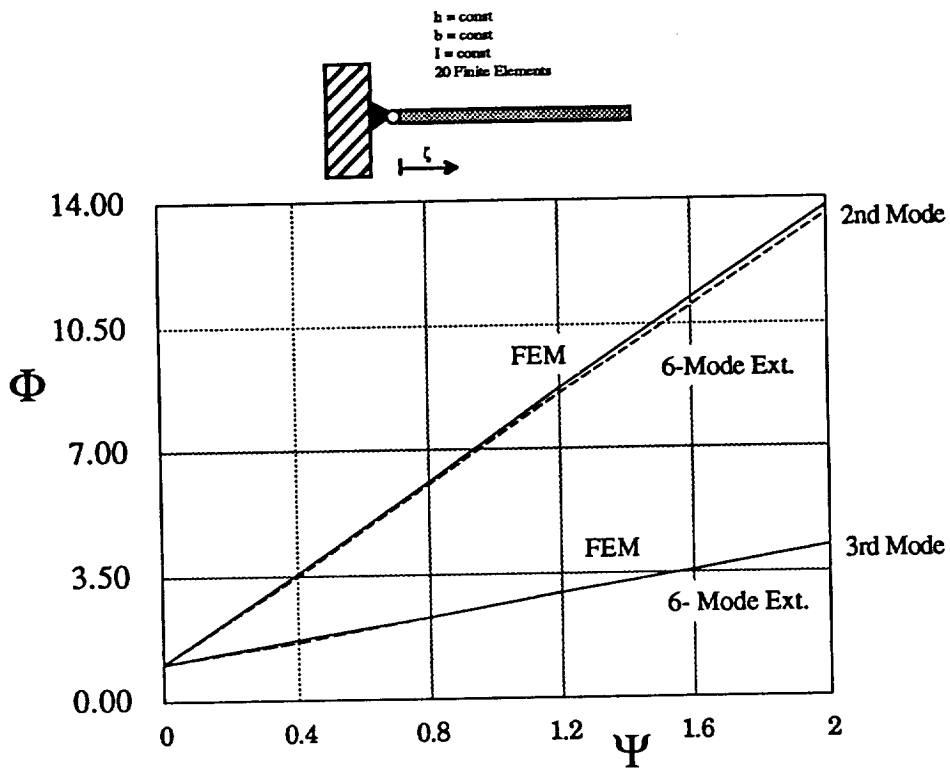


Fig. 2.3.4-3 Rotating, Hinged Constant Beam

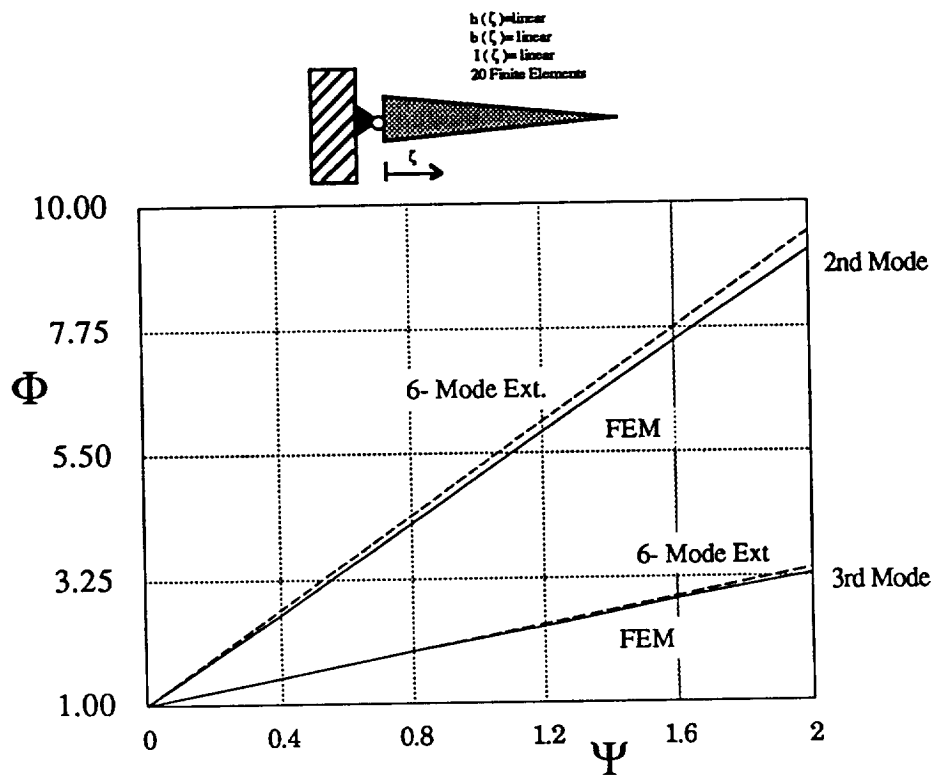


Fig. 2.3.4-4 Rotating, Hinged Tapered Beam

2.3.5 Accuracy and Convergence Characteristics for this Finite Element Application

It is of interest to us how exact our eigenvalues and eigenvectors are, and how confident we can feel about our results. The solutions we have found for the *calculated* ($\tilde{}$) eigenvectors, $\tilde{\Phi}$, and for the *calculated* ($\tilde{}$) eigenvalues, $\tilde{\lambda}$, were calculated by the EISPACK matrix and eigensystem routines (Ref. 2.-8). Of interest would be the convergence of the finite element program as a function of the number of elements used in the discretisation of the beam.

Having made the rather bold assumption that the rotational degrees of freedom were not assigned any rotary inertia, it is of even bigger importance to know more about what effect this simplification has on the calculations in order to be able to judge the effect on the projected rotating modes and frequencies.

Throughout literature (e.g. Ref. 2.-1, Ref. 2.-4, ...) analytic results are found for the mode shapes for constant beams with a constant stiffness along the beam under the assumption of a variety of boundary conditions. We will compare our solutions with the analytic solutions for the cantilever and hinged beams and attempt to show the convergence characteristics for the first three non-rigid body eigenvalues as a function number of elements used. A strategy for determining the quality of a calculated eigenvalue even if the true eigenvalue is unknown is also introduced.

Exact analytic solutions for the hinged-free, free-free and cantilevered beam natural frequencies ω_k are shown in Table 2.3.5-1 using

$$\omega_k = (\lambda_k l)^2 \left(\frac{B}{m\lambda^4} \right)^{0.5} \quad (2.3.5-1)$$

Table 2.3.5-1 Exact Solutions for the Constant Beam

System Type	Eigenvalue Equation	Rigid Body Modes	Values for $\lambda_k l$
Cantilevered	$1 + \cos \lambda l \operatorname{ch} \lambda l = 0$	0	1,8751 / 4,69409 / ... / $(n-0,50)\pi$
Hinged-Free	$(\lambda l) (\operatorname{th} \lambda l - \tan \lambda l) = 0$	1	3,9266 / 7,06858 / ... / $(n+0,25)\pi$
Free-Free	$(\lambda l)^4 (1 - \operatorname{ch} \lambda l \cos \lambda l) = 0$	2	4,73004 / 7.8532 / ... / $(n+0,50)\pi$

The convergence characteristics of the implemented finite element algorithm toward the exact analytical solution are shown in the following figures. Figs. 2.3.5-1a to 2.3.5-c show the convergence of the calculated solution divided by the exact solution of the cantilever beam eigenvalues towards the normalized exact solution (1.0) as a function of number of elements used, while Figs. 2.3.5-2a to 2.3.5-2d show the same for the hinged beam.

Cantilevered Beam

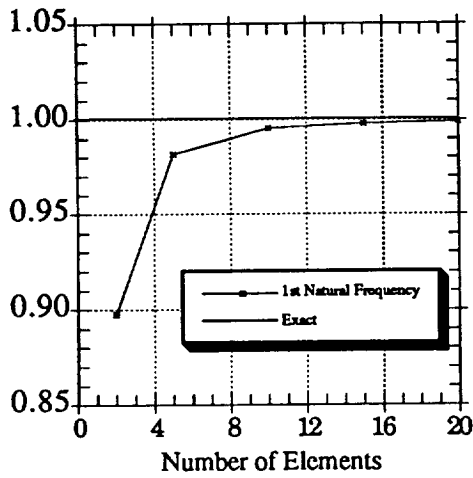


Fig 2.3.5-1a 1st Natural Frequency

Hinged Beam

The 1st natural mode for the hinged beam is the rigid body mode

Fig 2.3.5-2a 1st Natural Frequency

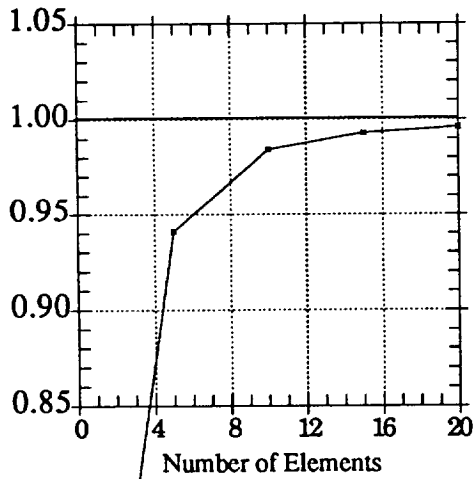


Fig 2.3.5-1b 2nd Natural Frequency

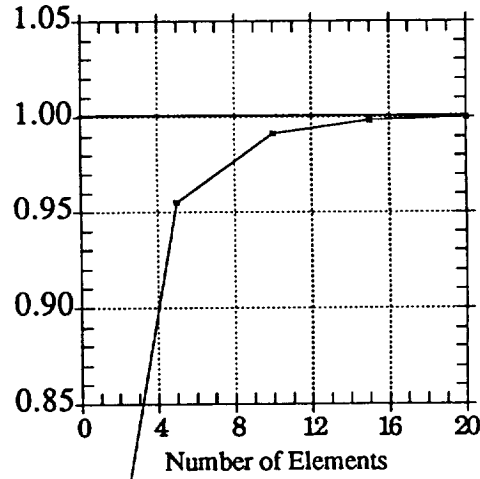


Fig 2.3.5-2b 2nd Natural Frequency

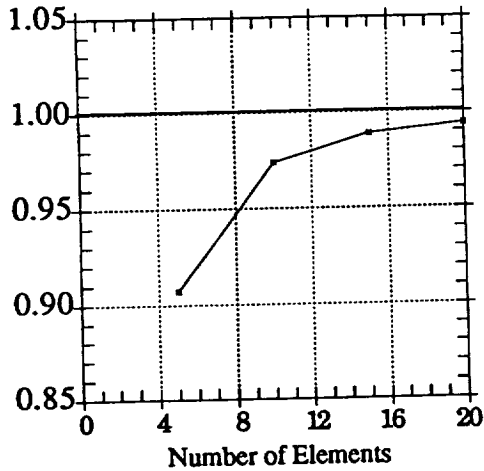


Fig 2.3.5-1c 3rd Natural Frequency

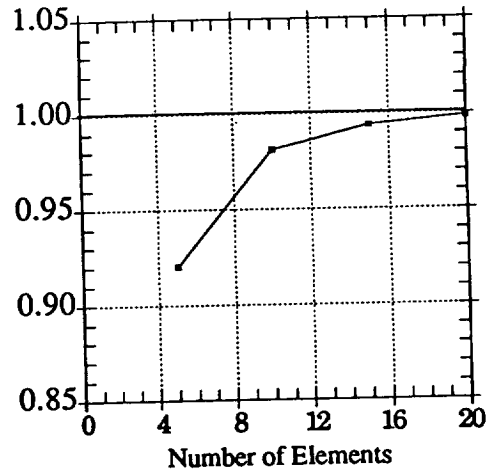


Fig 2.3.5-2c 3rd Natural Frequency

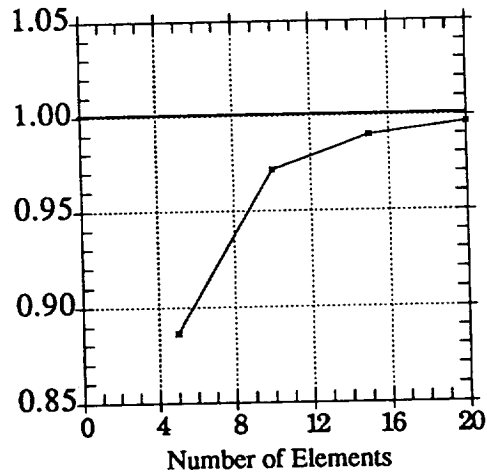


Fig 2.3.5-2d 4th Natural Frequency

The analytical equation for the mode shapes is

$$w_i(x) = \frac{\text{ch } \lambda_i x - \cos \lambda_i x}{\text{ch } \lambda_i l + \cos \lambda_i l} - \frac{\text{sh } \lambda_i x - \sin \lambda_i x}{\text{sh } \lambda_i l + \sin \lambda_i l} \quad (2.3.5-2)$$

for the cantilever beam and

$$w_i(x) = \frac{\text{sh } \lambda_i l \sin \lambda_i x + \text{sh } \lambda_i x \sin \lambda_i l}{2 \text{sh } \lambda_i l \sin \lambda_i l} \quad (2.3.5-3)$$

for the hinged beam

Figs 2.3.5-1a to -2d show that a good accuracy can be obtained by using 20 finite elements on a beam, resulting in having to solve only a 10x10 matrix after

static condensation. Tables for the first few eigenvectors for the calculated beams can be found in Appendix A.

2.4 Comparison of the Finite Element Calculation with the Full-Scale UH-60A Rotor Blade Non-Rotating Modal Analysis Shake Test

2.4.1 NASA Shake Test

A shake test of the UH-60A rotor blade was performed at the NASA Ames Research Center during April 1986 as part of the Phase I Flight Test MTR (Modern Technology Rotor) project. The rotor blade was outfitted with strain gages along the span and a movable piezoelectric accelerometer was used to measure the response at the node points. The data was analyzed to obtain the frequency response function (FRF) of the blade excitation and response. The linearity of the rotor blade system was established by varying that the FRF remained constant for an increasing input force level. The minimal input force level for a constant FRF was found to be 1 pound-force (4.44822 N). An upper boundary can be set at a force level that produces large, non-linear deflections. The Maxwell-Betty theorem was also found to apply. This states that the FRF that gives a response at point i of the structure resulting from a force input at point j is the same one as for a response at point j resulting from an input at point i ($H_{ij} = H_{ji}$) as shown in Fig. 2.4.1-1. This relationship was tested at frequencies of 12.55 Hz and 25.11 Hz and shown to hold .

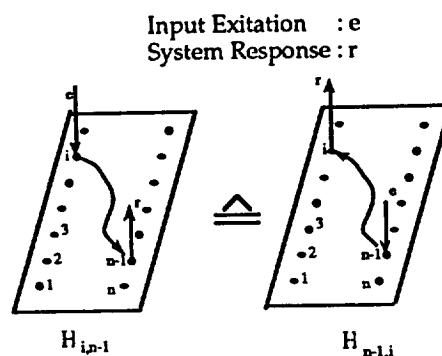


Fig. 2.4.1-1 Maxwell-Betty Theorem

The rigid body modes for the rotor blade suspended in a pseudo free-free manner by bungee chords was found to be 0.8 Hz for the 1st flapping and 0.2 Hz for the 1st torsional modes.

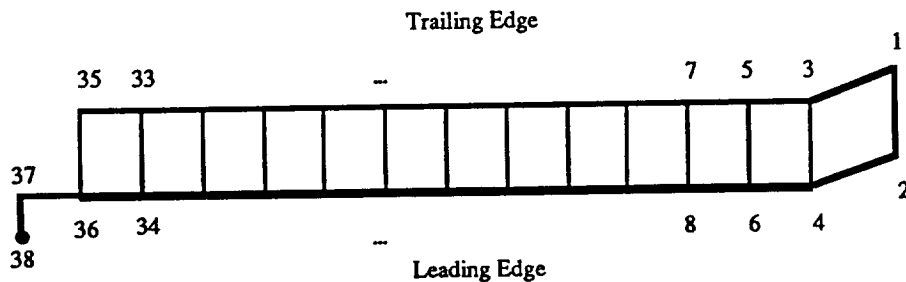


Fig. 2.4.1-2 Accelerometer Measurement Positions

The FRF and the modal data were measured by placing the accelerometer at coordinates 16 in (40.6 cm) apart along the leading and trailing edges and at the node points of each identified mode. The accelerometer measurement positions are shown in Fig. 2.4.1-2. The blade was also examined by CAMRAD (Comprehensive Analytical Model of Rotorcraft Aerodynamics and Dynamics) in a hinged-free configuration and these results were transferred to the shake test free-free boundary conditions by calculating the ratios between the exact free-free and hinged-free solutions and applying them to the CAMRAD hinged-free results (Ref. 2.-7). This may account for some of the large errors found with the CAMRAD program, especially in the higher modes, because the ratios were found by looking at the vibrating beam partial differential equation

$$\frac{\partial^2}{\partial x^2} \left[EI(x) \frac{\partial^2 y(x,t)}{\partial x^2} \right] = -m(x) \frac{\partial^2 y(x,t)}{\partial t^2} \quad (2.4.1-1)$$

for the two boundary conditions and then calculating the ratios. Since the above equation applies only to beams of a constant stiffness and mass distribution there is some error introduced by using it to obtain the ratios of hinged-free to free-free. The shake test identified 5 flapwise modes along with 2 chordwise and 2 torsional modes. The 5 flapwise modes that are examined and compared to our finite element model are given in the form of modal residues at the leading and trailing edge. The residues (given in Appendix B) represent the amplitude of the mode at the point of measurement. The residues of the trailing edge differ from those of the leading edge since the individual modes are not totally uncoupled. To negate this effect we will calculate the residues at the quarter-chord,

supposing that the residues change in a linear fashion across the span of the blade as demonstrated in Fig. 2.4.1-3. When these residues are normalized they display the expected modal shapes.

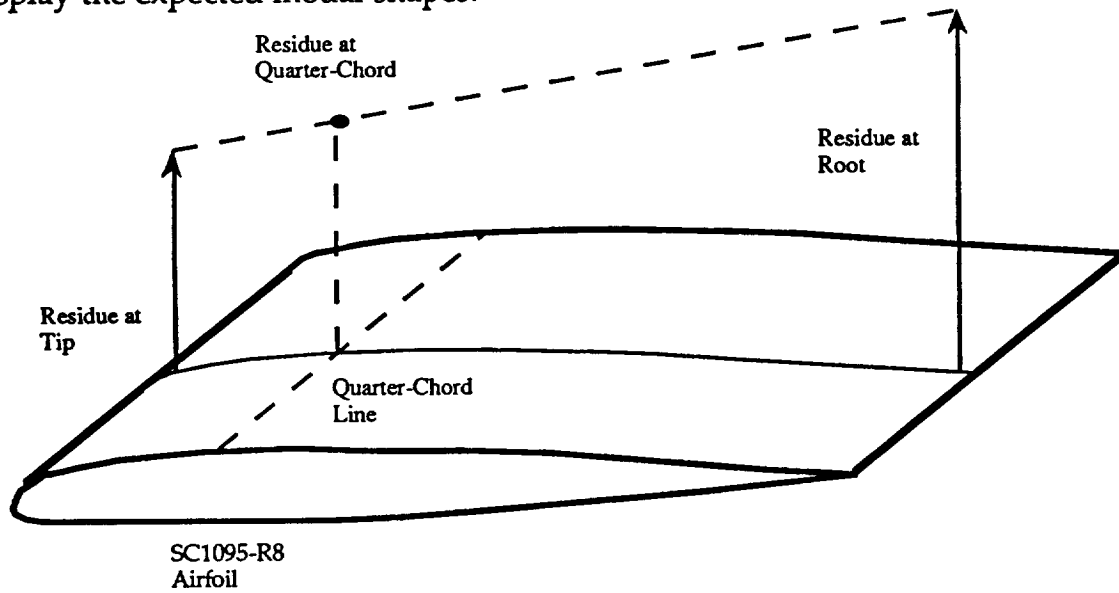


Fig. 2.4.1-3 Residue Calculation

2.4.2 Shake Test Results

2.4.2.1 Rotor Blade Data for Shake Test

The modulus of elasticity, E , for the Blackhawk rotor blade is

$$E = 10^6 \left[\frac{\text{lb}}{\text{in}^2} \right] = 0.68 \cdot 10^{10} \left[\frac{\text{N}}{\text{m}^2} \right]$$

The stiffness and mass distribution are given in Table 2.4.2.1-1 and in Figs. 2.4.2.1-1 and 2.4.2.1-2 and the natural frequencies for out of plane flapping that were measured during the shake test as well as the values calculated by CAMRAD are given in Table 2.4.2.1-2.

Table 2.4.2.1-1 Mass and Stiffness Distributions of the Blackhawk Rotor Blade

Blade Coordinate [cm]	Stiffness [kg m ²]*10 ⁻⁴	Mass [kg/cm]	Blade Coordinate [cm]	Stiffness [kg m ²]*10 ⁻⁴	Mass [kg/cm]
0.00000			448.270	0.979259	0.0108218
0.00000			448.300	0.979259	0.0106078
38.1000			492.690	0.979259	0.0106078
38.1001	2.33351		492.700	0.982316	0.0107505
38.2943	2.33351	0.112691	537.110	0.982316	0.0107505
38.2950	2.33351	1.36373	537.200	0.996582	0.0118713
38.5483	2.33351	1.36373	581.530	0.996582	0.0118713
38.5500	3.74992	0.0488335	581.600	0.996582	0.0134202
82.5483	3.74992	0.0488335	621.920	0.996582	0.0134202
82.6000	3.97410	0.0306311	622.000	0.996582	0.0133489
126.998	3.97410	0.0306311	662.310	0.996582	0.0133489
127.000	1.17083	0.0105365	662.400	0.962955	0.0132776
190.498	1.17083	0.0105365	702.700	0.962955	0.0132776
190.500	0.941556	0.0104651	702.800	0.946651	0.0165791
233.170	0.941556	0.0104651	735.640	0.946651	0.0165791
233.200	0.941556	0.0103938	735.700	0.841694	0.0181280
275.840	0.941556	0.0103938	768.580	0.841694	0.0181280
275.900	0.941556	0.0105365	768.600	0.625666	0.0170683
318.510	0.941556	0.0105365	788.140	0.625666	0.0170683
318.600	0.941556	0.0105365	788.200	0.377030	0.0127884
361.180	0.941556	0.0105365	807.700	0.377030	0.0127884
361.200	0.950727	0.0105365	807.800	0.313852	0.00406581
403.850	0.950727	0.0105365	817.860	0.313852	0.00406581
403.900	0.979259	0.0108218			

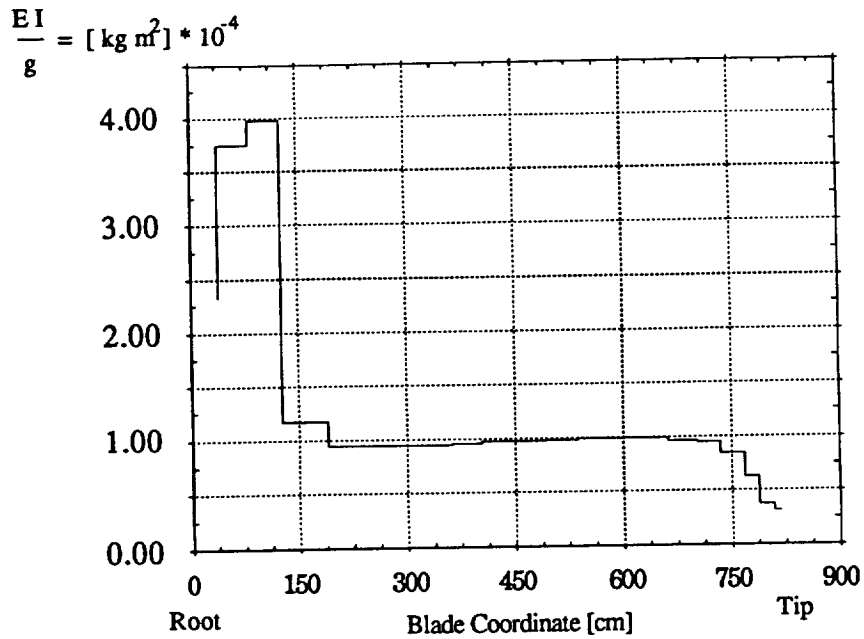


Fig. 2.4.2.1-1 Stiffness Distribution of the Blackhawk Rotor Blade

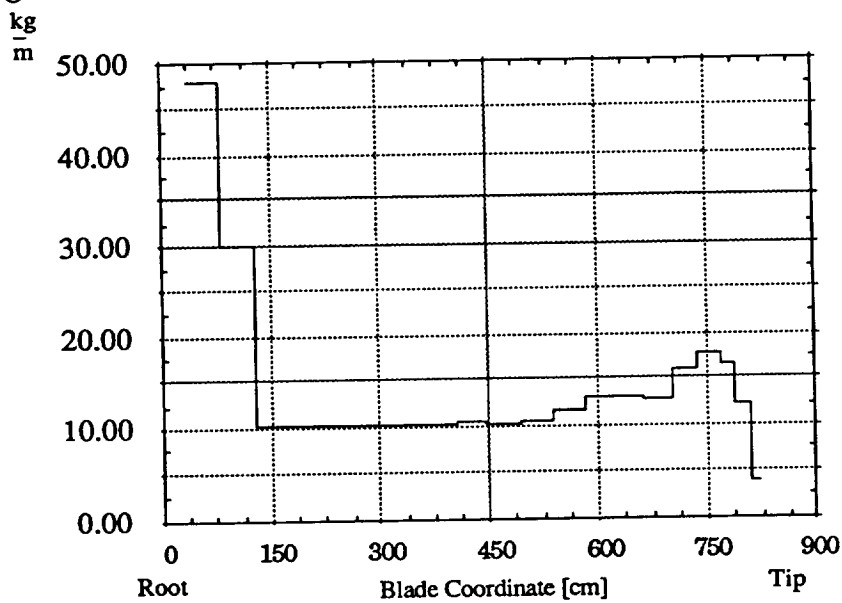


Fig. 2.4.2.1-2 Mass Distribution of the Blackhawk Rotor Blade

Table 2.4.2.2-1 Natural Frequencies, Out-of-Plane Flapping

Mode	Shake Test [Hz]	CAMRAD [Hz]
1st	4.34	4.67
2nd	12.55	12.75
3rd	24.99	25.49
4th	41.63	42.32
5th	63.71	57.75

2.4.3 Results of the Non-Rotating Finite Element Analysis

2.4.3.1 Discretization Technique

The Blade was divided into three large parts in accordance with the degree that the mass and stiffness distributions varied. These parts were then in turn subdivided into finite elements. Three different division schemes (DS) were introduced to investigate the way the solutions converge as a function of the number of elements. The DS are given in Table 2.4.3.1-1 and DS2 for the first normalized cantilever mode is shown in Fig. 2.4.3.1-1.

Table 2.4.3.1-1 Division Schemes

	Scheme 1	Scheme 2	Scheme 3
Number of Elements Part 1 (0...2m)	20	25	35
Number of Elements Part 2 (2...6m)	15	20	30
Number of Elements Part 3(6...7.29m)	20	25	35

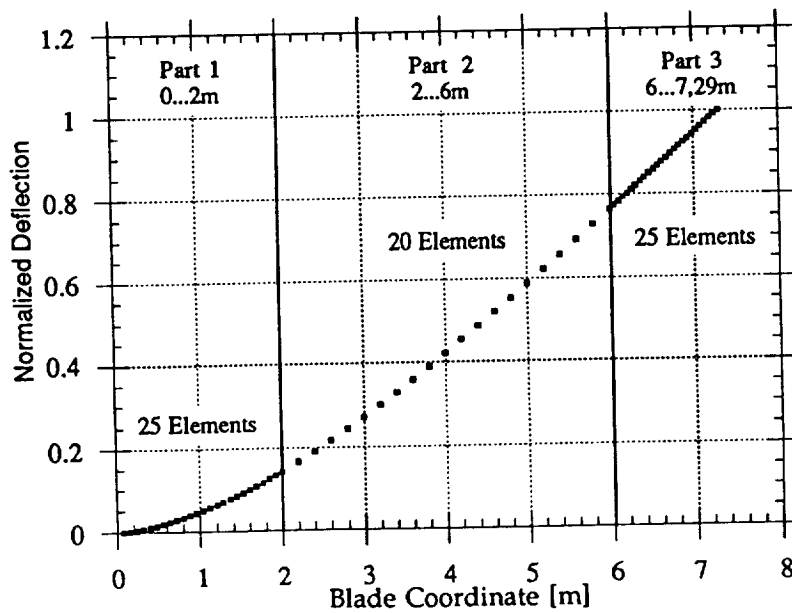


Fig. 2.4.3.1-1 DS2

Results for the different DS and their deviations from the shake test results and CAMRAD are given in Table 2.4.3.1-2 below.

Table 2.4.3.1-2 Results for Different DS

Mode	Nat. Frequency (Shake Test) [Hz]	Nat. Frequency (DS1) [Hz]	Nat. Frequency (DS2) [Hz]	Nat. Frequency (DS3) [Hz]	Change: DS3(FEM)-Test	Change: CAMRAD-Test
1st	4.34	4.46337	4.51864	4.51473	+ 4.02%	+ 6.68%
2nd	12.55	12.91	12.9917	12.9731	+ 3.37%	+ 1.59%
3rd	24.99	25.9137	26.249	26.2149	+ 4.90%	+ 2.00%
4th	41.63	43.3187	43.9606	43.8759	+ 5.39%	+ 1.65%
5th	63.71	65.0184	65.7907	65.6459	+ 3.04%	- 9.35%

It can easily be seen, that the CAMRAD-Program gives us a fairly good estimate of the natural frequencies that can be expected. The error varies, and CAMRAD fails to predict accurate natural frequencies for all higher modes. Even though our Finite Element model accounts for only out-of-plane flapping motion at this time, and disregards the coupling with the torsional and inplane vibrational modes, the results are in very good agreement with the measured data. Including these additional degrees of freedom (or allowing for coupling of the modes) would tend to "soften" the rotor blade and bring down the natural frequencies, and thus, the approach for the measured natural frequencies would be even better.

Of especially great interest would be the inclusion of the torsional modes, since they would be coupled most with the flapping mode due to the twist and swept tip of the blade. In addition, the 1st chordwise natural frequency lies close to the 3rd flapping natural frequency which would also tend to lead to some coupling.

To judge how exact the program would calculate the natural frequencies given an exact value for the first natural frequency, the modulus of elasticity was *adjusted* to supply exactly the first measured natural frequency. Since ω_n is proportional to the square root of E, (2.3.5-1) we can simply set

$$\left(\frac{\omega_{1\text{calc}}}{\omega_{1\text{test}}} \right) = \left(\frac{E}{E_{\text{adj}}} \right)^{0.5} \quad (2.4.3.1-1)$$

and we receive an adjusted E as

$$E_{adj} = 0.628383 \cdot 10^{10} \left[\frac{N}{m^2} \right] = 0.940693 \cdot 10^6 \left[\frac{lb}{in^2} \right] \quad (2.4.3.1-2)$$

Using this adjusted value to simulate a blade less stiffened through modal coupling we find the results of Table 2.4.3.1-3.

Table 2.4.3.1-3 Natural Frequencies Calculated with an Adjusted Modulus of Elasticity

Mode	DS3 $\left(\frac{m_{gen}}{k_{gen}} \right)$	Shake Test [Hz]	Change: DS3(FEM)- Test
1st	4.34	4.34	-----
2nd	12.47	12.55	- 0.59%
3rd	25.23	24.99	+ 0.989%
4th	42.39	41.63	+ 1.84%
5th	63.80	63.71	+ 0.146%

In Figs. 2.4.3.1-3a to 2.4.3.1-3g we introduce the calculated mode shapes of the free-free UH-60A rotor blade along with the normalized modal residues of the shake test. We have used the coordinate system from the shake test used in the free-free analysis (i.e. going from tip to root of the blade, shown in Fig. 2.4.3.1-2) to ease comparison with the test results, but in all other calculations (cantilevered and hinged) we have used the more common coordinate system going from the root of the blade outward. The measured mode shapes (residues) of the shake test were normalized not as usual with the maximum deflection at the beginning or end of the blade, but in such a manner that they coincided at some point along the blade with the calculated mode shapes. This was done, since the modal residues were assumed to vary linearly across the chord of the blade and calculated at quarter chord. The tip of the blade is swept back, and the shaker was attached to the root, and so the quarter-chord modal residues calculated at these points that show the maximum deflection are not considered to be very reliable. These points of coincidence were 4.165 m for the 1st, 3rd and 5th mode, 5.34 m for the 2nd mode and 6.125 m for the 5th mode.

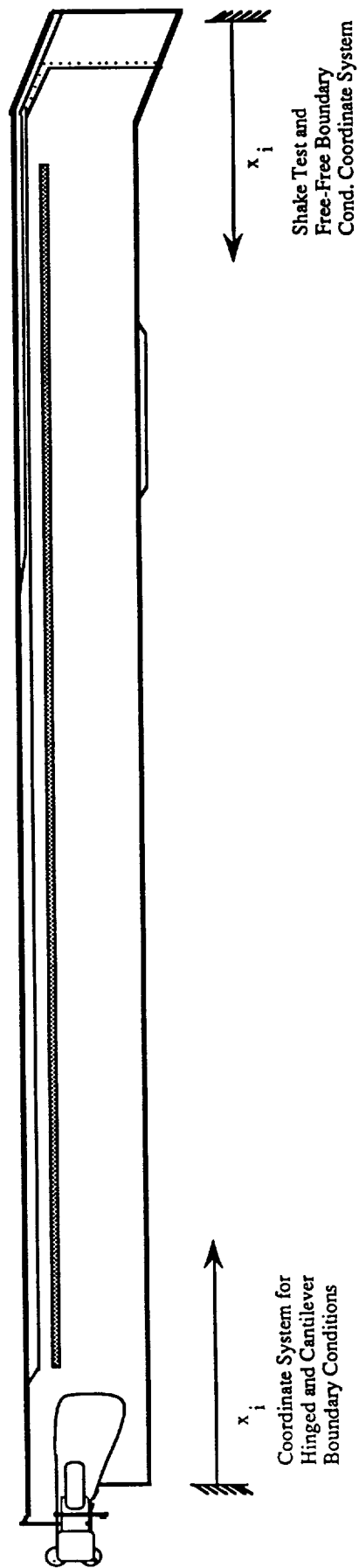


Fig. 2.4.3.1-2 Blackhawk Rotor Blade

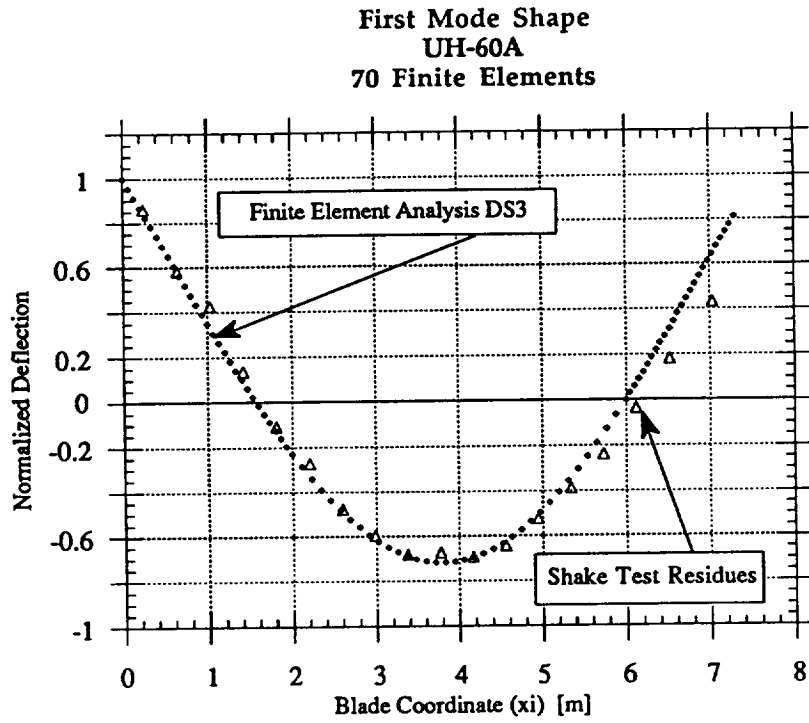


Fig. 2.4.3.1-3a Comparison of Calculated and Measured Flapwise Mode Shapes

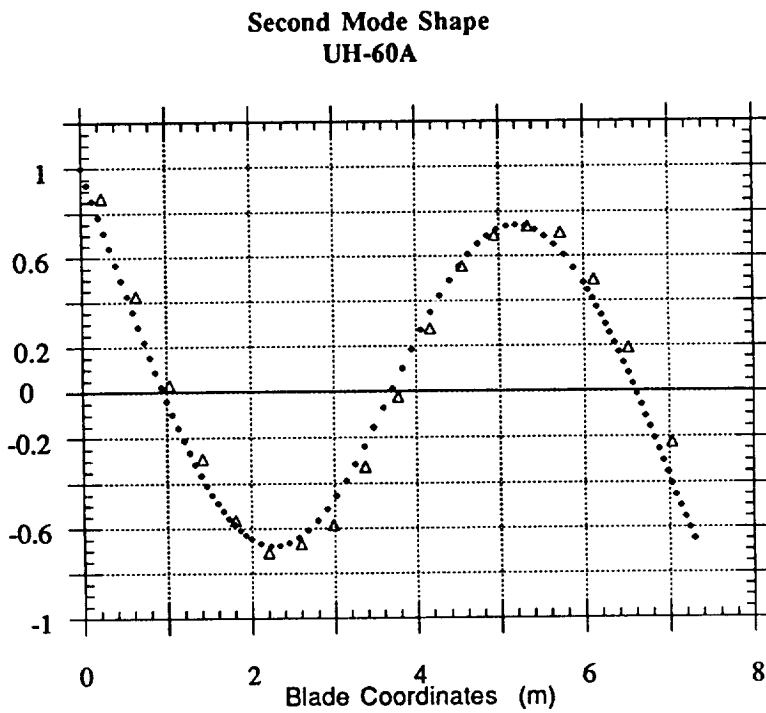


Fig. 2.4.3.1-3b Comparison of Calculated and Measured Flapwise Mode Shapes

Third Mode Shape
UH-60A

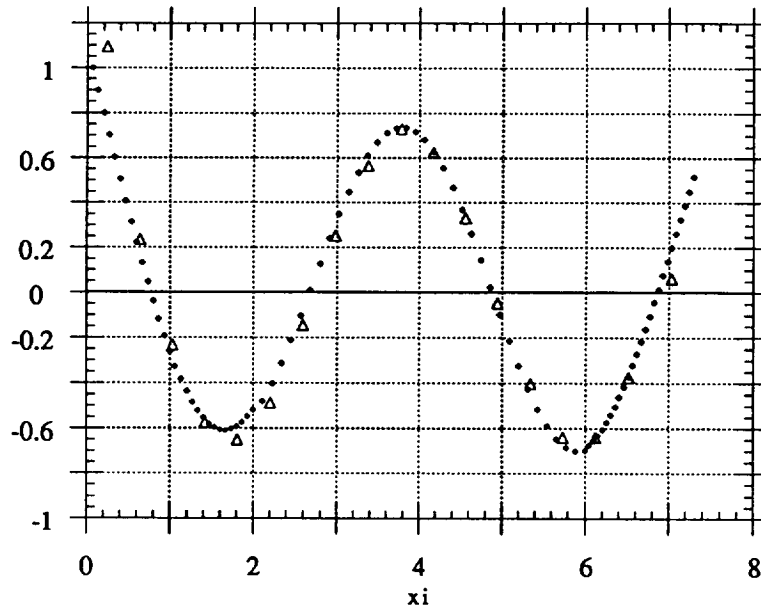


Fig. 2.4.3.1-3c Comparison of Calculated and Measured Flapwise Mode Shapes

Fourth Mode Shape
UH-60A

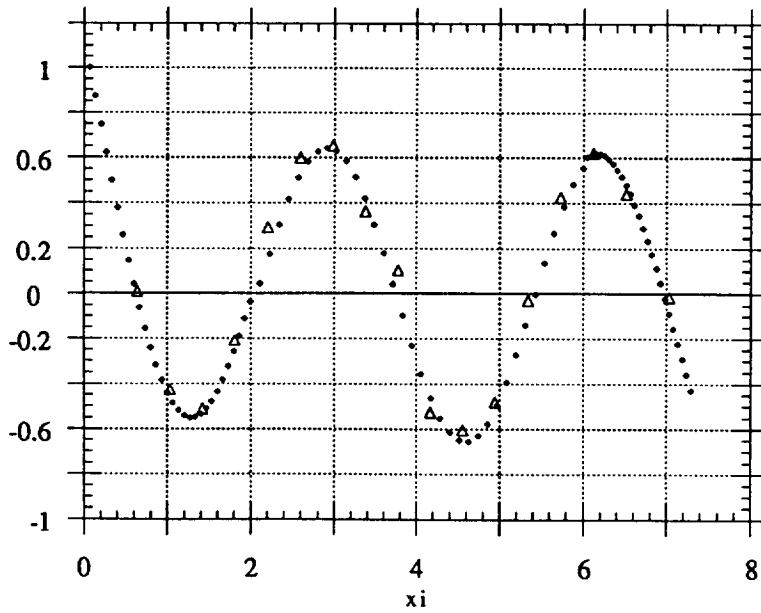


Fig. 2.4.3.1-3d Comparison of Calculated and Measured Flapwise Mode Shapes

Fifth Mode Shape
UH-60A

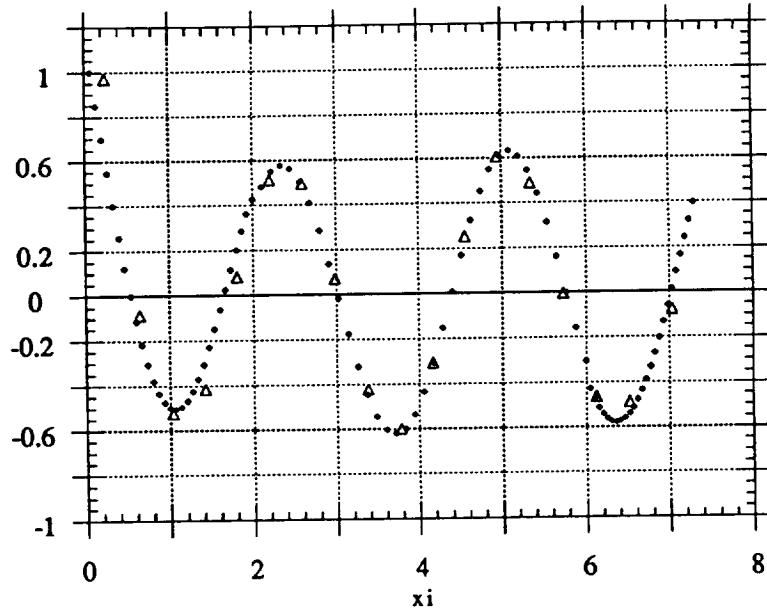


Fig. 2.4.3.1-3e Comparison of Calculated and Measured Flapwise Mode Shapes

Sixth Mode Shape
UH-60A

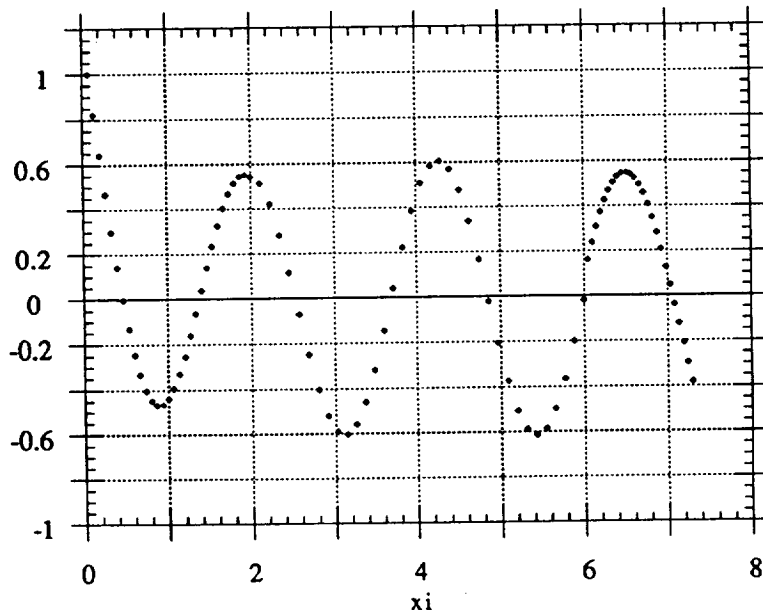


Fig. 2.4.3.1-3f Comparison of Calculated and Measured Flapwise Mode Shapes

**Seventh Mode Shape
UH-60A**

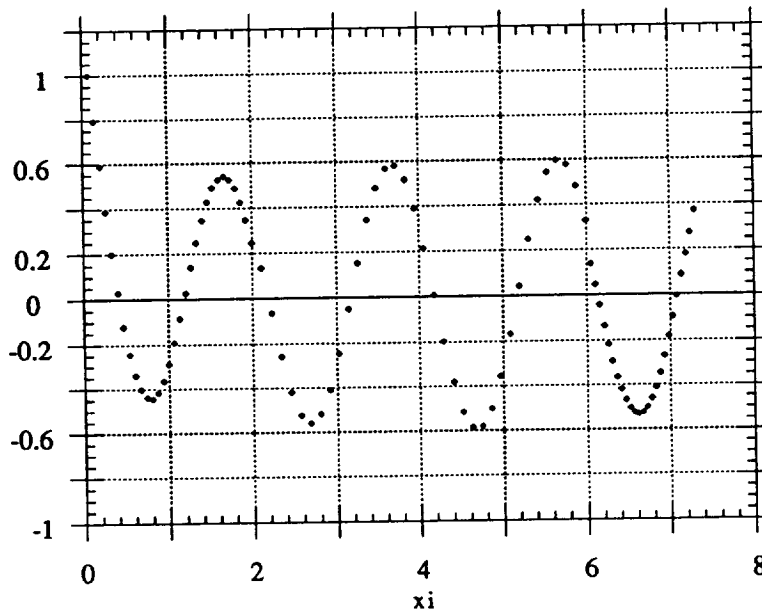


Fig. 2.4.3.1-3g Comparison of Calculated and Measured Flapwise Mode Shapes

The Calculated Data shows a high correlation with the measured mode shapes.

The same comparison is now done for the calculated and measured natural frequencies for the first two inplane (chordwise) modes. Table 2.4.3.1-4 gives the calculated results along with the deviations from the shake test and the calculated mode shapes are shown versus the measured mode shapes in Figs. 2.4.3.1-4a and 2.4.3.1-4b.

Table 2.4.3.1-4 Results for the First Two Inplane Modes

Mode	Shake Test (Hz)	FEM (Hz)	Change: FEM-Test
1st	25.38	26.28	+ 3.5 %
2nd	67.38	73.27	+ 8.7 %

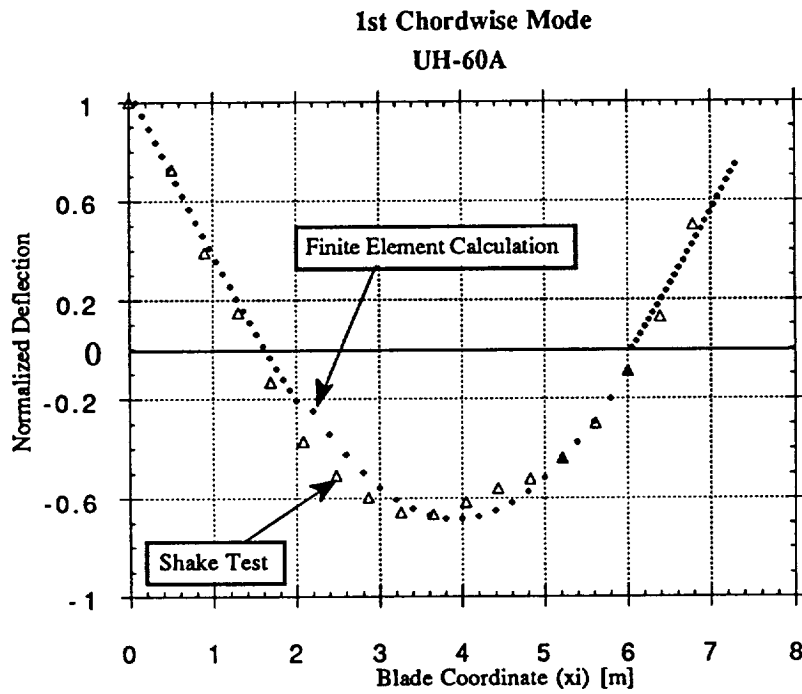


Fig. 2.4.3.1-4a Calculated vs. Measured Inplane Mode

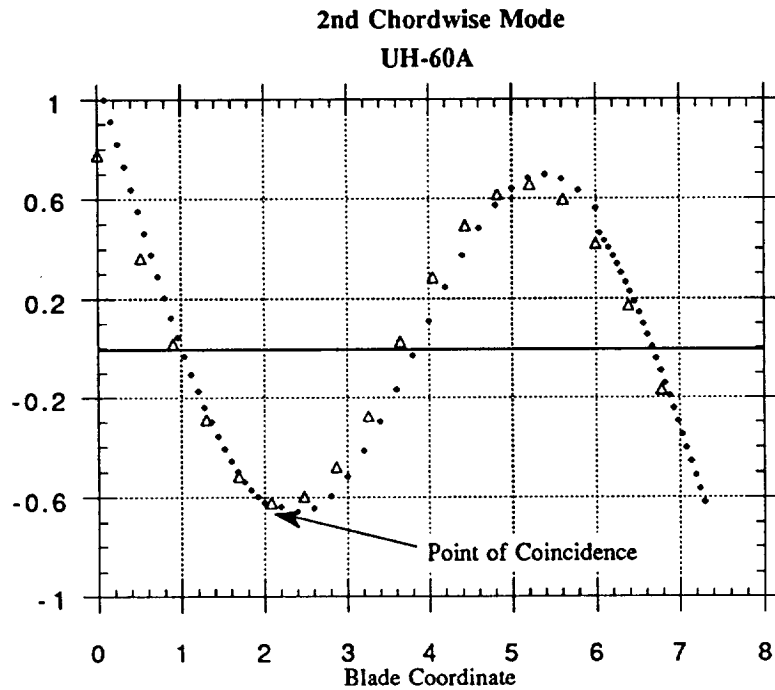


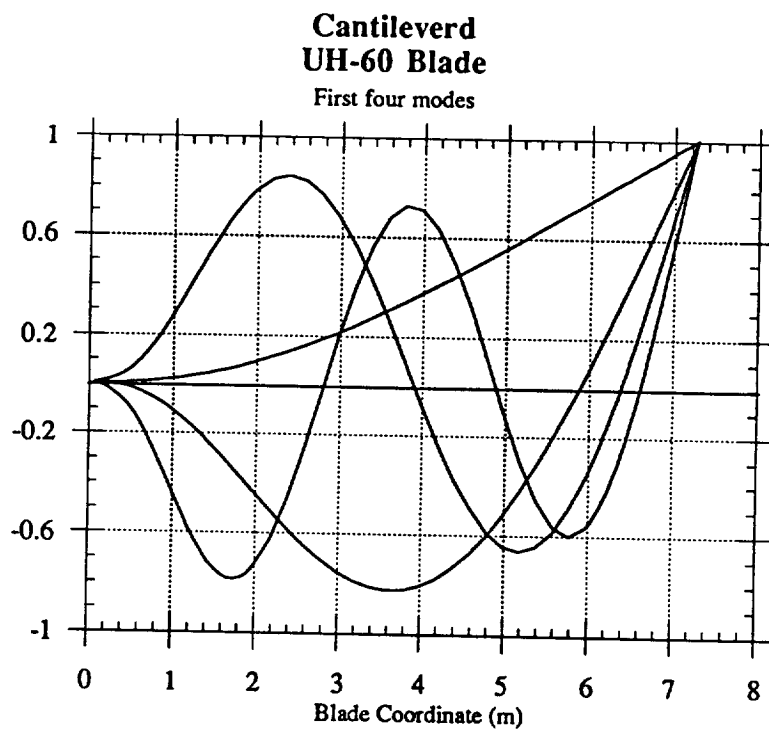
Fig. 2.4.3.1-4b Calculated vs. Measured Inplane Mode

2.4.3.2 Results from other Boundary Conditions

Using DS3, the natural mode shapes and frequencies for other boundary conditions in a non-rotating state were calculated and are introduced in Table 2.4.3.2-1 and Figs. 2.4.3.2-1 and 2.4.3.2-2

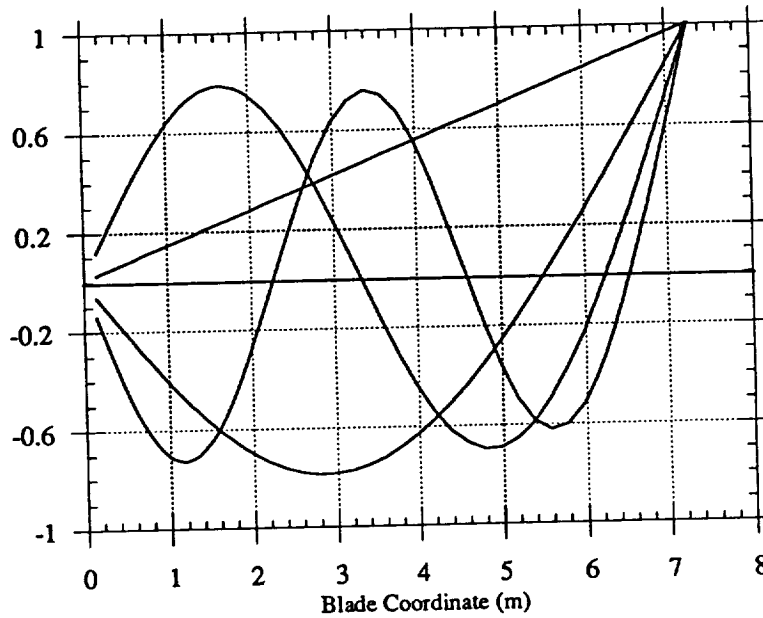
Table 2.4.3.2-1 Non-Rotating Results for DS3

Mode	Hinged-Free [Hz]	Cantilevered [Hz]
1st	rigid body	2.52586
2nd	10.889	17.2904
3rd	40.6414	48.07
4th	75.1265	93.7772
5th	128.8254	152.615



Figs. 2.4.3.2-1 First Four Modes, Non-Rotating, Cantilevered Blade

**Hinged-Free
UH-60 Blade**
First four modes



Figs. 2.4.3.2-2 First Four Modes, Non-Rotating, Hinged Blade

2.4.4 Rotating Results

2.4.4.1 Increase of the Natural Frequencies

Having ascertained a high level of accuracy and convergence of our finite element model, we will now use this model to predict the rotating natural frequencies for the UH-60A Blackhawk Rotor Blade for the cases of hinged-free and cantilevered boundary conditions.

The relationship between the speed of rotation and the increase of the natural frequencies will again be displayed in the familiar fashion using the dimensionless parameters

$$\Psi = \left(\frac{\Omega}{\omega_{n1}} \right)^2 \quad (2.3.3-7)$$

$$\Phi = \left(\frac{\omega_{rot}}{\omega_{ni}} \right)^2 \quad (2.3.4-1)$$

Figs. 2.4.4.1-1 and 2.4.4.1-2 show the increase of the first and second natural frequency for the cantilevered and hinged rotor blade as the speed of rotation increases.

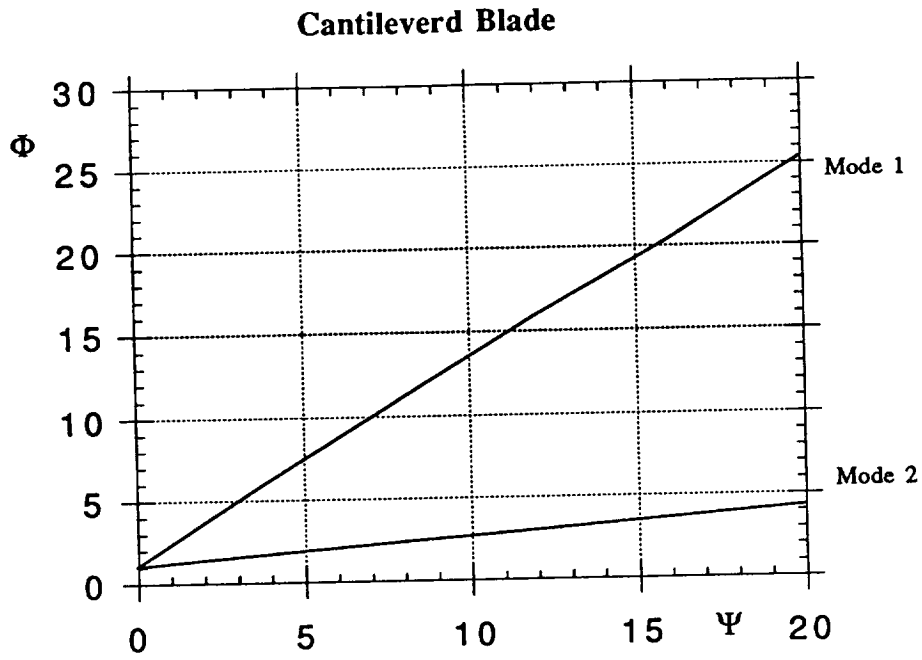


Fig. 2.4.4.1-1 Increase of Natural Frequency vs. Rotational Speed

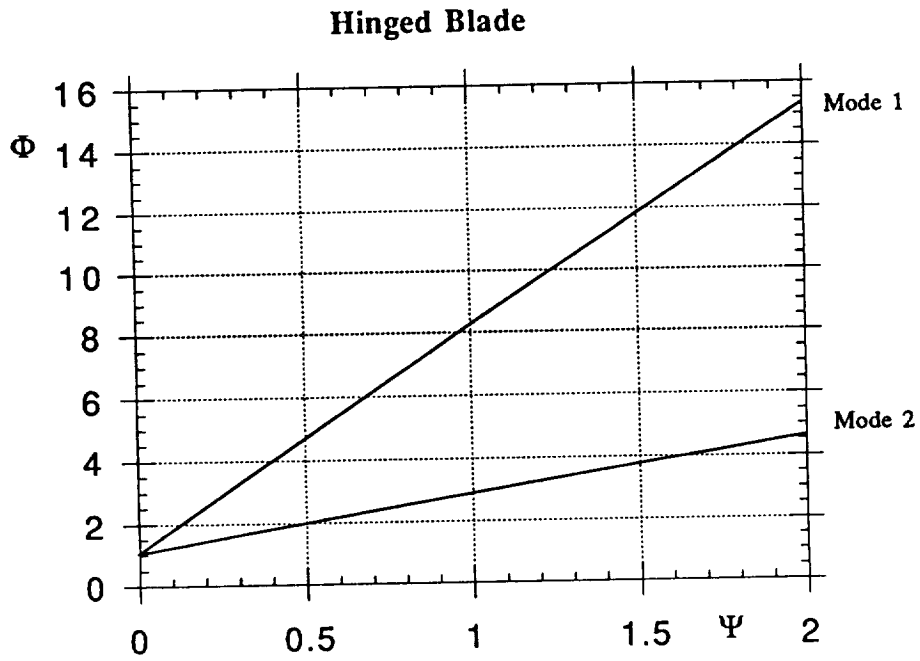


Fig. 2.4.4.1-2 Increase of Natural Frequency vs. Rotational Speed

2.4.4.2 Comparison between Rotating and Non-Rotating Predicted Mode Shapes

Having verified that our non rotating calculated mode shapes show high correlation with the measured residues, we can calculate the rotating mode shapes and examine the change between the non rotating and rotating mode shapes. Figs. 2.4.4.2-1 to 2.4.4.2-4 show the change of the cantilevered natural mode shape of the UH-60A Rotor Blade in a non-rotating and rotating state, and Figs. 2.4.4.2-5 to 2.4.4.2-8 show the same for the hinged Blade. The rotational parameters were set to $\Psi = 12$ for the cantilever blade and to $\Psi = 1.6$ for the hinged blade. The abscissa shows the non-normalized blade coordinate in meters.

Cantilevered

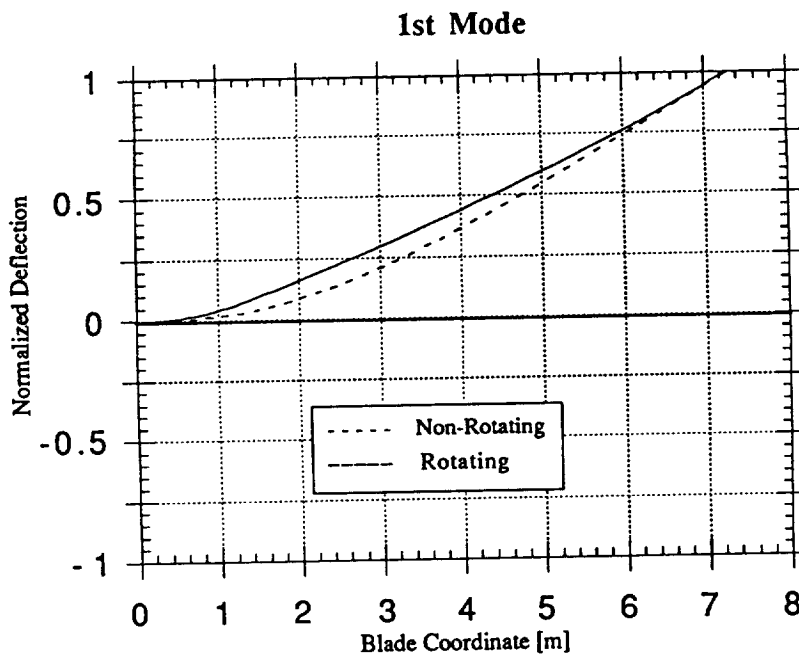


Fig. 2.4.4.2-1 Rotating vs. Non-Rotating Mode Shape

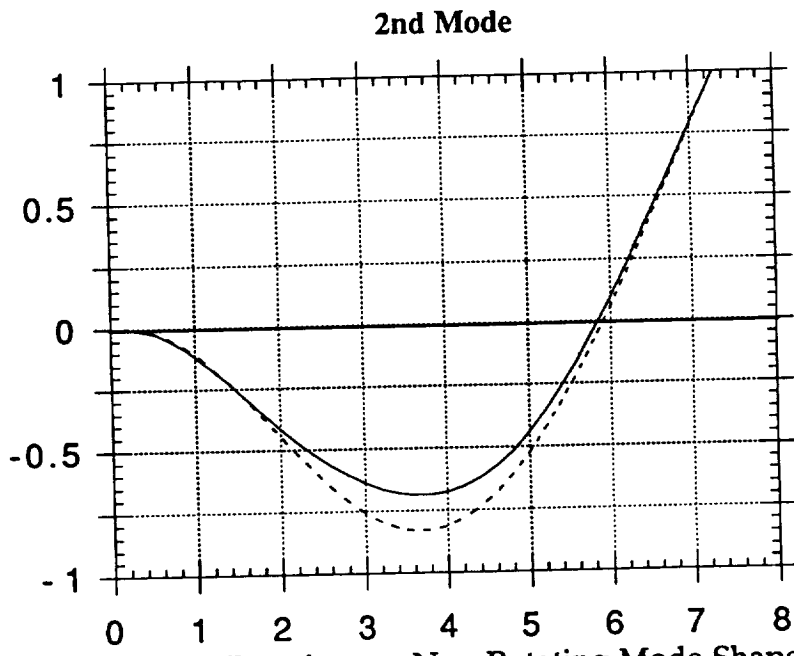


Fig. 2.4.4.2-2 Rotating vs. Non-Rotating Mode Shape

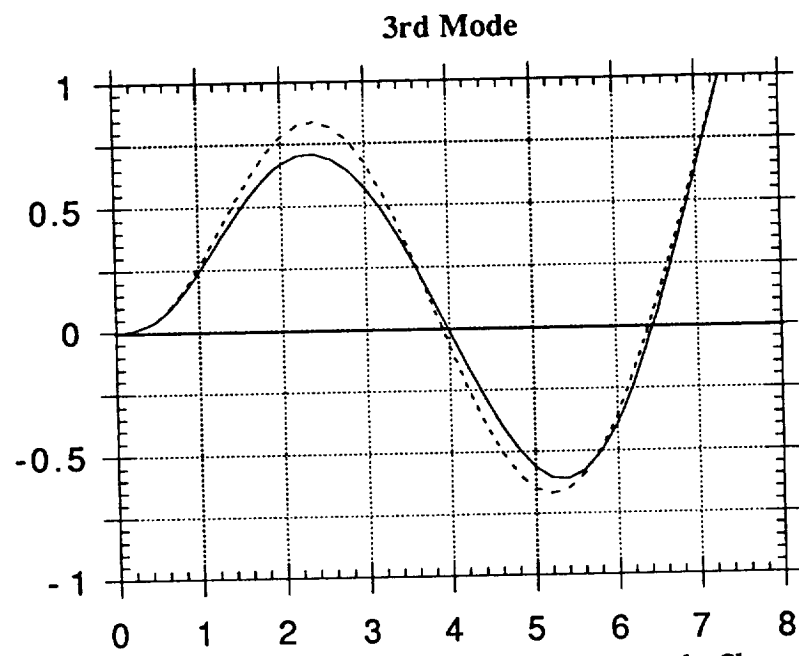


Fig. 2.4.4.2-3 Rotating vs. Non-Rotating Mode Shape

4th Mode

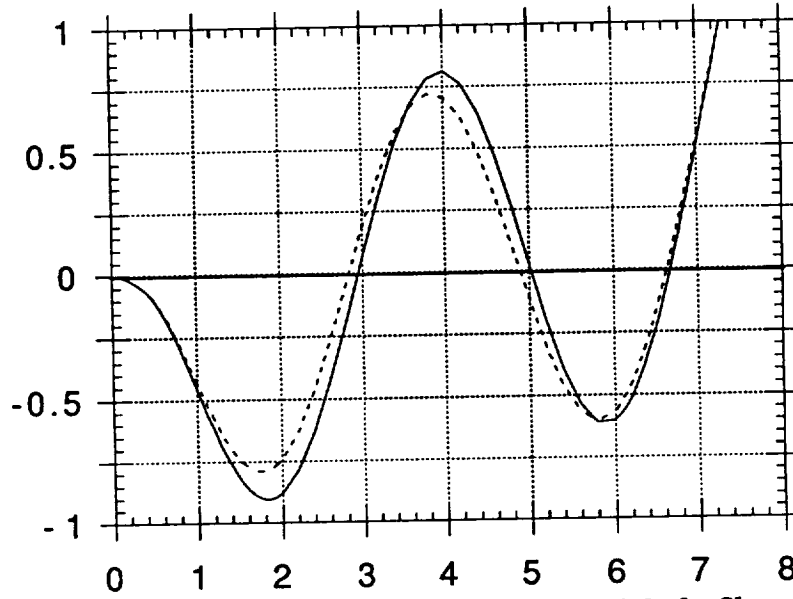


Fig. 2.4.4.2-4 Rotating vs. Non-Rotating Mode Shape

Hinged

The first mode is the rigid-body mode,

2nd Mode

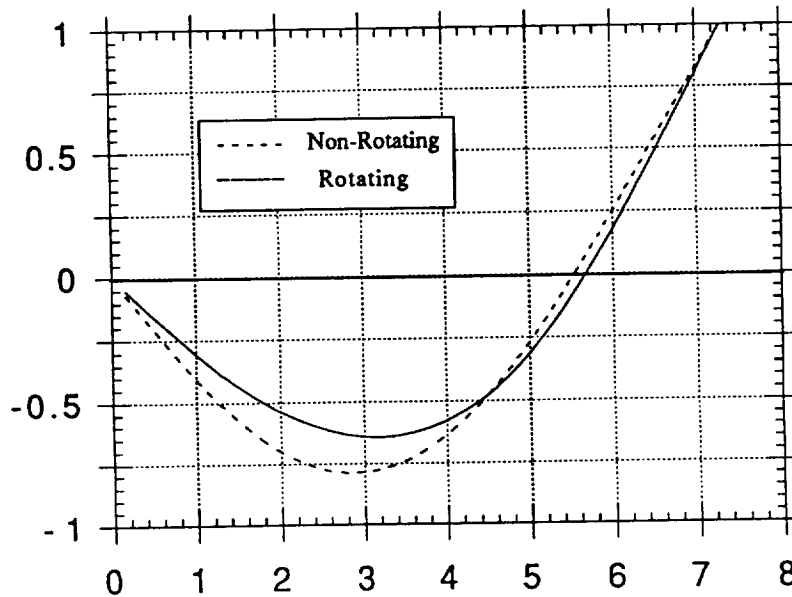


Fig. 2.4.4.2-5 Rotating vs. Non-Rotating Mode Shape

3rd Mode

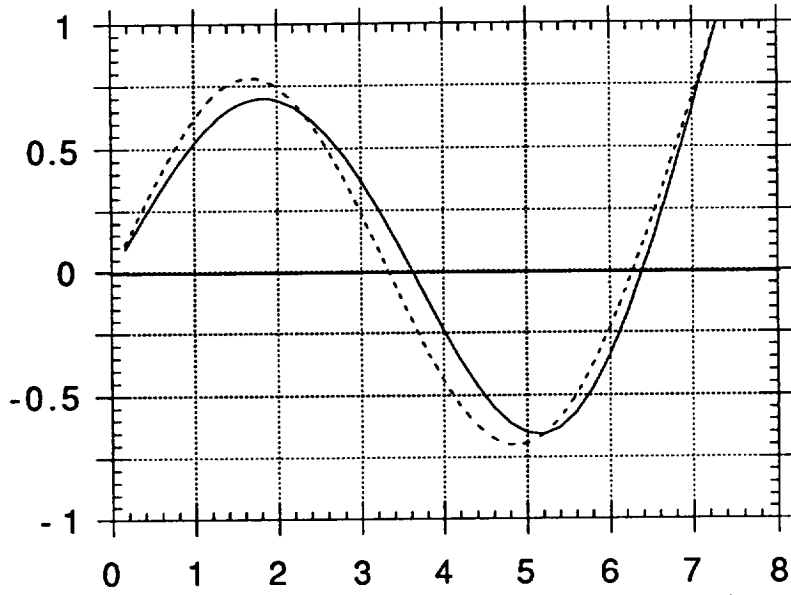


Fig. 2.4.4.2-6 Rotating vs. Non-Rotating Mode Shape

4th Mode

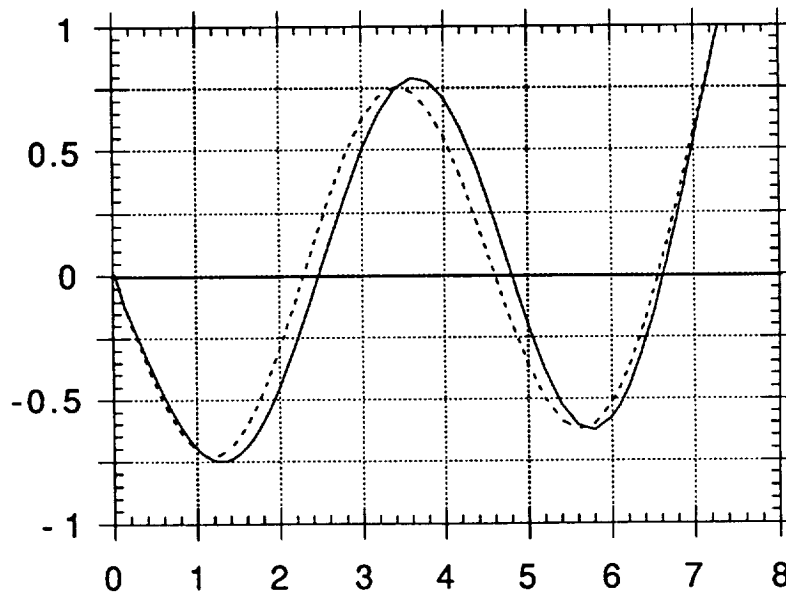


Fig. 2.4.4.2-7 Rotating vs. Non-Rotating Mode Shape

5th Mode

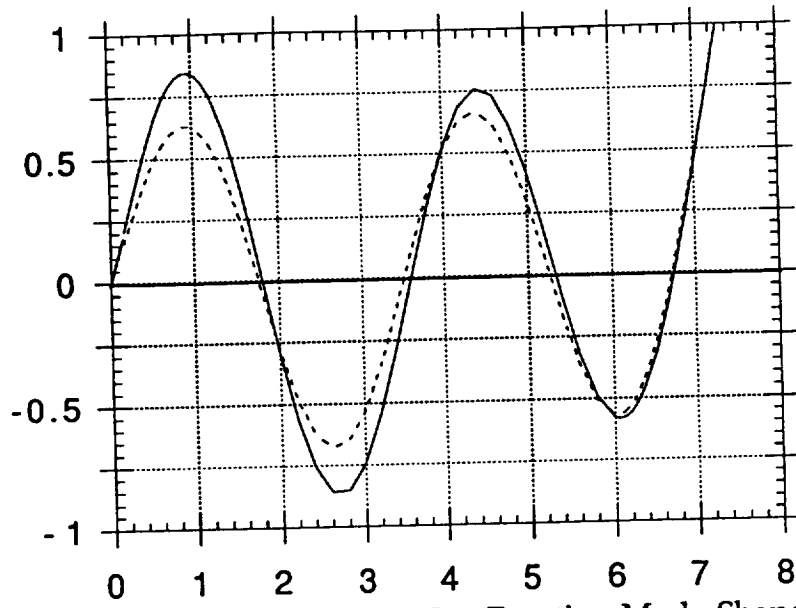


Fig. 2.4.4.2-8 Rotating vs. Non-Rotating Mode Shape

3. Spectral Analysis of the UH 60A Flight Records

3.1 Introduction

After obtaining an estimate of the rotating natural frequencies and modes of the Blackhawk helicopter rotor blade, a first attempt was made to detect these natural frequencies in the flight test records. This flight test data was obtained by computer down-link from the Tilt Rotor Engineering Data System (TRENDS), a database of the NASA-Ames Research Center. The highly instrumented Flight Test Phase 1 (Ref. 3.1) of the Blackhawk Program provided a multitude of dynamic and vibrational data that was available for downloading. The data pertaining to the vibrational and rotor characteristics available at TRENDS is listed in Table 3.1-2.

The steady-state response of the rotor system will be at frequencies corresponding to the period of the aerodynamic driving forces. These non-linear excitation functions have frequencies that are integer multiples of the rotational speed of the rotor blade ($\frac{1}{\text{rev}}, \frac{2}{\text{rev}}, \frac{3}{\text{rev}}, \dots = 1P, 2P, \dots$). The resulting spectral densities of the histories of the responses to this aerodynamic forcing function will be composed mainly of frequency contributions having the periodicity of $1P, 2P, \dots$, leaving the relatively small contributions of the transient natural modes "buried" in the data. During a control input of the pilot, it is hoped that these transient responses are excited to a measurable degree. So what we would need in order to uncover transients hidden in the histories is a flight test that contained well documented control inputs along with the response of the rotor blade to these input. It should be stressed at this point that this analysis does not constitute an in-depth evaluation of the existing database, but it was hoped that by a careful selection of available flights and vibrational parameters, those datasets would be found that showed the greatest promise of disclosing the desired information. The results from this first examination of the database may also show future researchers how to better choose and find relevant datasets in the database.

Scanning the project database (See Ref 3.-2) for descriptions of the different flight tests performed, flight 31 was chosen for further evaluation since this flight

was conducted to show effects of sinusoid control inputs. The flightlog is shown in table 3.1-1 below.

Table 3.1-1 : Log, Flight 31

AIRCRAFT: 748	SINE SWEEP CONTROL INPUTS	T/O GW: 18224
FLIGHT: 31	LOCATION: AEFA	CG: 362.5
FLT DATE: 22 MAY 87	COUNTERS: 3101- 3130	HRS TO INSP: 0.0
DIRECTOR: BUCK	PILOTS: CASON AND WEBRE	FLT TIME: 1.2
FLIGHT INFO: FLIGHT 31 WAS A SPECIAL FLIGHT THAT WAS NOT PART OF THE NASA PHASE I TEST PLAN. THIS FLIGHT CONSISTED OF SINUSOIDAL CONTROL INPUTS THROUGH ALL AXES (LONG., LAT., PEDAL, AND COLLECTIVE), AT TWO AIRSPEEDS: HOVER AND 120 KIASB.		
CONFIGURATION: LASSIE AND BALLAST CART INSTALLED		
FLIGHT NOTES: PARAMETERS KNOWN NOT TO BE WORKING: ALL PARAMETERS WERE THOUGHT TO BE FUNCTIONING.		
COUNTER TYPES: MULTI AXIS SINE SWEEP CONTROL INPUTS.		
ANALOG TAPES: ITH748031.DAT		
DIGITAL TAPES: ITH748031.01X THROUGH ITH748031.30X		
VAX DATASETS: YES PLEASE.		

The available vibrational and rotor parameters are shown in Table 3.1-2 , along with their units. AZMRT, AZMRR, MRBR5, MRBR6 and MRBR7 were examined and finally AZMRT was chosen for the spectral analysis, since it showed the greatest change in magnitude and intensity after a control input, even though this parameter would be expected to show the greatest amount of noise. An additional factor in the selection of AZMRT was that it showed more intense and sharper peaks at multiples of the vibrational speed all the way up to 10P, whereas the other vibrational parameters only showed distinct peaks up to 5P. This is demonstrated in Fig. 3.1-1. by showing the spectral density function available directly from TRENDS for the vibrational parameters.

Table 3.1-2 Available Parameters

Rotor Parameters			
Item	Description	Units	Sampling Freq. [Hz]
AXMRT	Tip accel. edgewise	G's	517/1
AZMRR	Root acceleration flapping	G's	516/1
AZMRT	Tip accel. flapping	G's	516/1
MRALSS	MR link load aft	Lbs	
MRBR5	MR rear bending 50% radius	PSI	516/1
MRBR6	MRrearbending 60% radius	PSI	516/1
MRBR7	MRrearbending 70% radius	PSI	516/1
MREB5	MR edgewise bending 50% rad.	IN-LB	516/1
MREB7	MR edgewise bending 70% rad.	IN-LB	516/1
MREBX1	MR root edgewise	IN-LB	
MRFLAP	MR flapping	Deg	516/1
MRFLSS	MR link load forward	Lbs	
MRLAG	MR lead-lag	Degs	516/1
MRLSS	MR link load lateral	Lbs	
MRNB5	MR normal 50% radius	IN-LB	516/1
MRNB6	MR normal bend. 60% radius	IN-LB	516/1
MRNB7	MR normal bend. 70% radius	IN-LB	516/1
MRNBX1	MR root normal bending	IN-LB	516/1
MRPITCH	MR pitch	Degs	516/1
MRPR	MR pushrod load	Lbs	516/1
MRSEBL	MR shaft bending	In-lb	516/1
Aircraft Parameters			
Item	Description	Units	Freq
COLLSTK	Control position, collective	Inches	32/1
LATSTK	Control position, lateral	Inches	32/1
LONGSTK	Control position, longitudinal	Inches	32/1

UH-60A A/C 748 PHASE I TESTS
 FLT 31: SINE SWEEP CONTROL INPUTS
 CTR 3106: HOVER, LAT STICK SINE SWEEPS

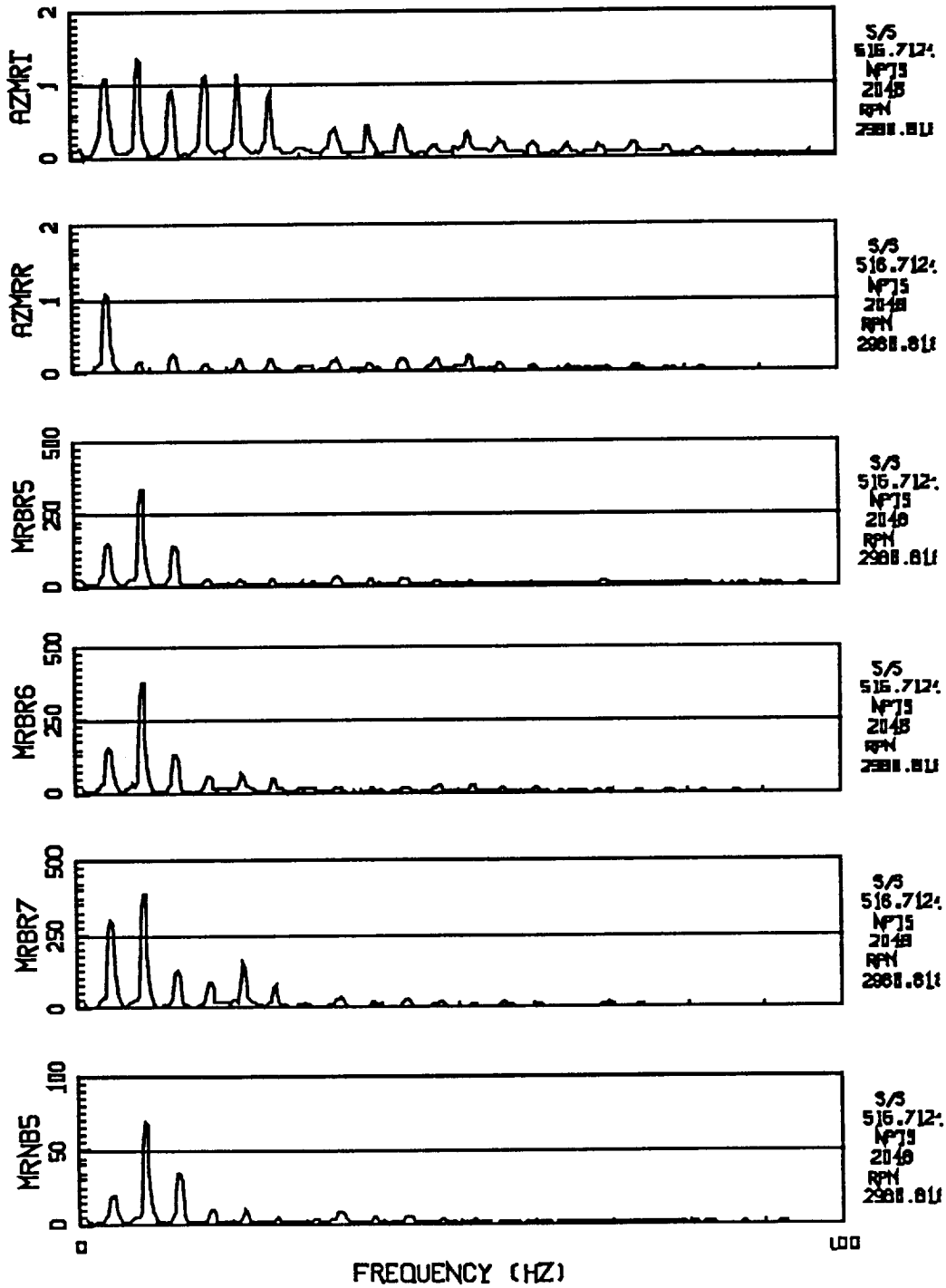


Fig 3.1-1 Spectral Density Distribution for Vibrational Parameters

Flight 31 is subdivided into 14 datasets of about 23 second each numbered with counters 04-18. These counters were scanned and counters 08 and 10 were chosen for further evaluation. Fig 3.1-2 and Fig 3.1-3 show excerpts of these counters for the parameters AZMRT, the main control inputs (COLLSTK - control position, collective and LONGSTK - Control position, longitudinal), as well as the rotational speed of the rotor, RPMMR. The units for these parameters can be found in Table 3.1-2.

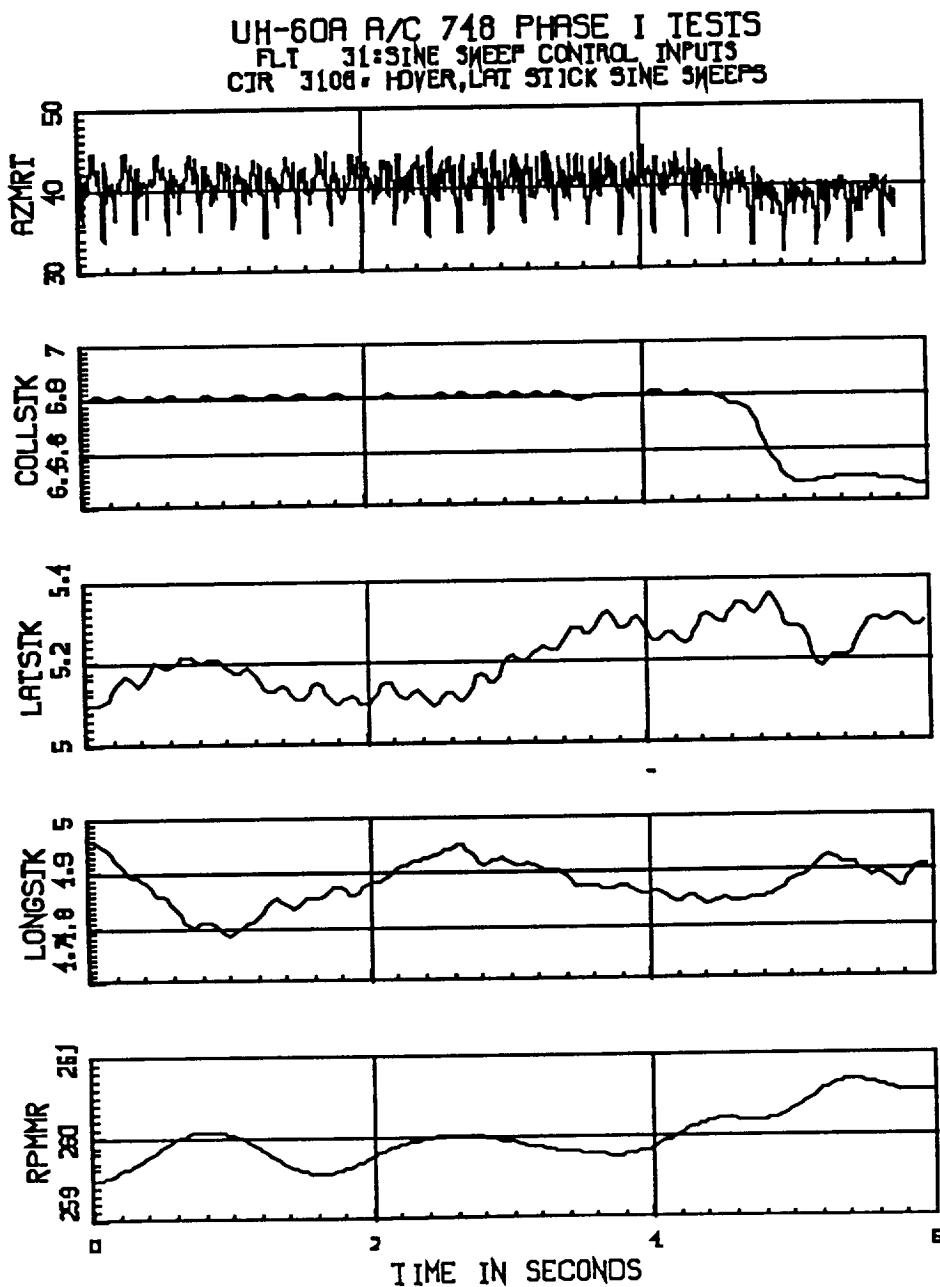


Fig. 3.1-2 Counter 08, Flight 31 (3108)

UH-60A A/C 748 PHASE I TESTS
 FLT 31: SINE SWEEP CONTROL INPUTS
 CTR 3110: HOVER, COL STICK SINE SWEEPS

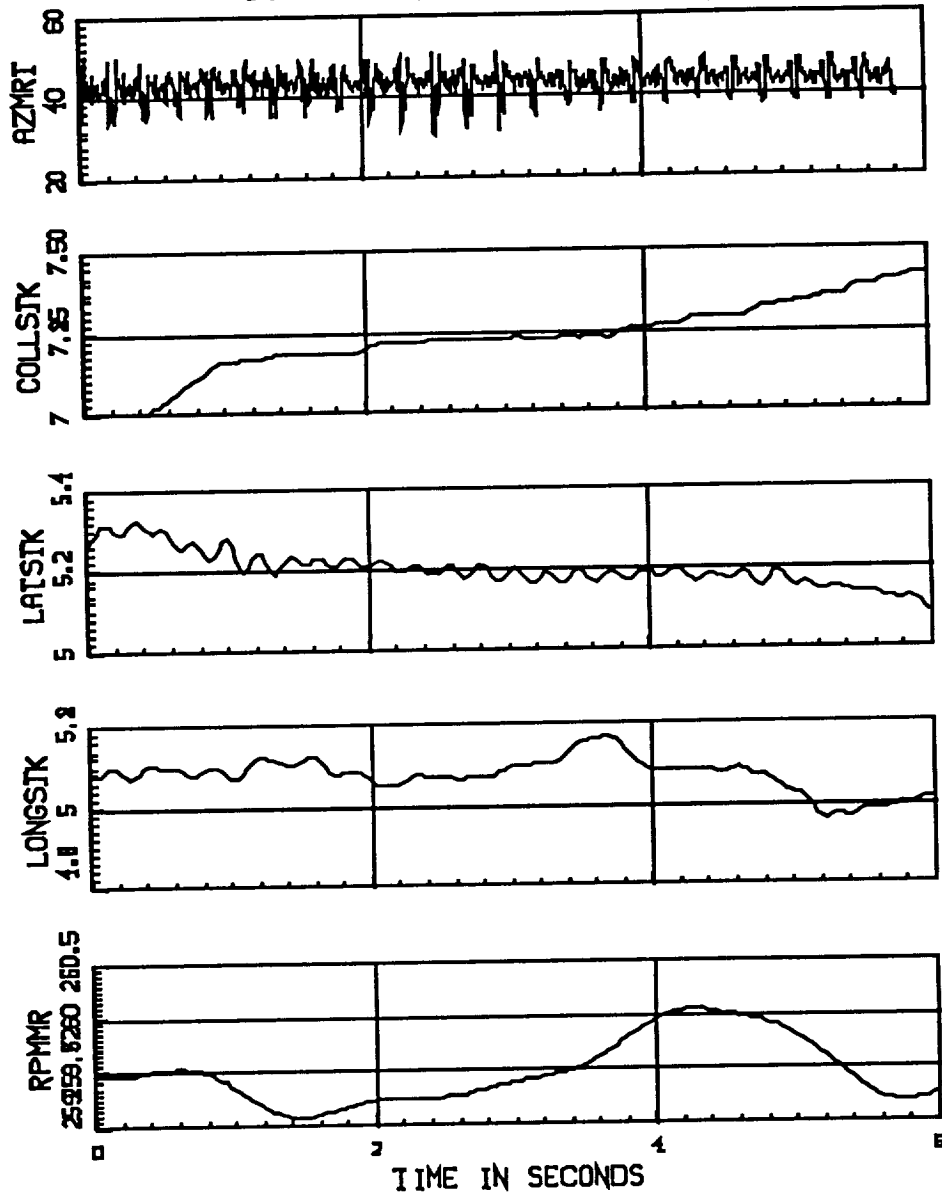


Fig. 3.1-2 Counter 10, Flight 31 (3110)

3.2 Projected Natural Frequencies

Using the Finite Element Program outlined in the previous chapters we calculate the first and Second rotating natural frequencies of the rotor blade at the given rotational speed interval to be :

Table 3.2-1 Rotating Natural Frequencies of the Rotor Blade

Counter	Rot. Speed (RPM)	ω_{n1} (Hz)	ω_{n2} (Hz)
3108	258.0 - 261.0	15.95 - 16.05	40.79 - 40.89
3110	258.5 - 261.5	15.97 - 16.07	40.81 - 40.93

It would of course be impossible to measure the natural frequencies as exact as they are given in Table 3.2-1, the main objective is to show that the natural frequency does not perturb much as the rotational speed varies.

3.3 Analysis Procedure

3.3.1 Obtaining the Spectral Density Distribution

Power spectral densities (PSD's) of various intervals of the response histories and their ratios were calculated (See also Ref 3.-3, 3.-4).

Power spectral density distributions or spectras are defined by the Fourier Transforms of their correlation functions:

$$S_{xx}(\omega) = \frac{1}{2\pi} \int_{-\infty}^{+\infty} R_{xx}(\tau) e^{-i\omega\tau} d\tau \quad (3.3.1-1)$$

However, utilizing the discrete fourier transform (DFT) it is not necessary to calculate the explicit term for the correlation function, since the spectral density can be expressed directly by multiplying the fourier transform by its complex conjugate. This can be shown by considering the discrete formulation of the spectral density function, where S_k is the DFT of the autocorrelation function R_r .³

³ A discrete series can always be written as an addition of sine and cosine terms:

$$x(t) = a_0 + \sum_{k=1}^{\infty} a_k \cos\left(\frac{2\pi kt}{T}\right) + b_k \sin\left(\frac{2\pi kt}{T}\right)$$

$$S_k = \frac{1}{N} \sum_{r=0}^{N-1} R_r \exp\left(-i\frac{2\pi kt}{N}\right) \quad (3.3.1-2)$$

R_r is an estimate of the correlation function defined by

$$R_r = \frac{1}{N} \sum_{s=0}^{N-1} x_s x_{s+r} \quad (r=0,1,2,\dots, N-1) \quad (3.3.1-3)$$

Inserting (3.3.1-3) into (3.3.1-1) and rearranging terms leads to

$$S_k = \frac{1}{N^2} \sum_{r=0}^{N-1} \sum_{s=0}^{N-1} x_s \exp\left(i\frac{2\pi ks}{N}\right) x_{s+r} \exp\left(-i\frac{2\pi k(s+r)}{N}\right) \quad (3.3.1-4)$$

The terms with the variable integer r can be grouped together and we can rewrite the expression as

$$S_k = \frac{1}{N} \sum_{s=0}^{N-1} x_s \exp\left(i\frac{2\pi ks}{N}\right) \left\{ \frac{1}{N} \sum_{r=0}^{N-1} x_{s+r} \exp\left(-i\frac{2\pi k(s+r)}{N}\right) \right\} \quad (3.3.1-5)$$

and introducing the new variable $t=(s+r)$

$$S_k = \frac{1}{N} \sum_{s=0}^{N-1} x_s \exp\left(i\frac{2\pi ks}{N}\right) \cdot \frac{1}{N} \sum_{t=s}^{(N-1)+s} x_t \exp\left(-i\frac{2\pi kt}{N}\right) \quad (3.3.1-6)$$

If we assume x_r to be periodic with period N (an assumption that has to be made in order to apply the DFT) , then $x_{N+s}=x_s$. Thus the second term of (3.3.1-6) is simply the DFT of $x(s)$, $X(s)$. The first term is similar to X_s , with the exception of the sign of the exponent. This represents X_s^* , the complex conjugate of X_s . This shows that the PSD can be simply calculated from the DFT by

where $a_k\{b_k\} = \frac{1}{T} \int_0^T x(t) \cos(\sin)\left(\frac{2\pi kt}{T}\right) dt$ or using complex notation for the Fourier

Transform, $X_k = a_k + i b_k$, it can be written as:

$$X_k = \frac{1}{T} \int_0^T x(t) \exp\left(-i\left(\frac{2\pi kt}{T}\right)\right) dt$$

$$S_k = X_s^* X_s$$

(3.3.1-7)

The DFT can easily be calculated by existing code for the Fast Fourier Transformation (FFT).

3.3.2 Ideal Boxcar Filters in the Frequency Domain

Ideal Boxcar filters of varying frequency bands were applied to the spectra obtained by the FFT, in order to suppress the steady state excitation of 1P, 2P and up. This approach did not lead to any practical results, because of the smearing of the peaks and the noise level inherent in the data. This analysis technique was found to be not applicable and quickly discarded.

3.3.3 Mapping to the Z-Plane

We are dealing with a discrete time series when we are evaluating the measurement data from the flight test. The continuous time (CT) function $s(t)$ is now transformed into a discrete time (DT) function, $s(nT)$ with values defined only for $t = n \cdot T$, where n is an integer and T is the sampling rate. CT signals can be transformed to the (complex) frequency domain by the Fourier and Laplace transforms. The result of the transformation usually provides us with additional insight into the operation of the system. For some systems that do not meet the conditions required by the Fourier transform, the Laplace transform is used, which involves the transformation into the $s = \sigma + i\omega$ plane. The Fourier transform is a special case of the Laplace transform for $\sigma=0$, that is, for input systems that can be represented as a superposition of sinusoidal waveforms. DT signals can also be represented by a Fourier transform, but instead of using the Laplace transform, the z-transform is used.

We can introduce the z transform by setting up the relation between the the complex s plane and the complex z plane

$$z \equiv e^{(sT)} \quad (3.3.3-1)$$

This function is a mapping of points in the s plane to points in the z plane. In circuit and control theory, values of s that cause a system transfer function to become zero or infinity (poles) provide information about the systems response to signals with a given frequency value. The mapping of the s plane into the z plane is as follows. The $i\omega$ axis of the s plane ($\sigma=0$) corresponds to $z = \exp(-i\omega T)$.

This is a circle of unit radius in the z plane. As ωT varies from $-\pi$ to $+\pi$, this generates a circular path in the z plane from $z=-1$ (-180°) to $z=+1$ ($+180^\circ$). Thus the z transform takes a strip in the s plane between $(-\frac{\pi}{T}) < \omega < (\frac{\pi}{T})$ and maps it into the unit circle of the z plane. The left-hand side of the s plane is mapped *into* the unit circle ($s < 0, |z| < 1$). The right hand side of the s plane is mapped *outside* of the unit circle ($s > 0, |z| > 1$). If an analog system has poles only in the left-hand s plane, it is stable, and its poles will map inside the unit circle in the z plane as well. This mapping is shown in Fig 3.3.3-1.

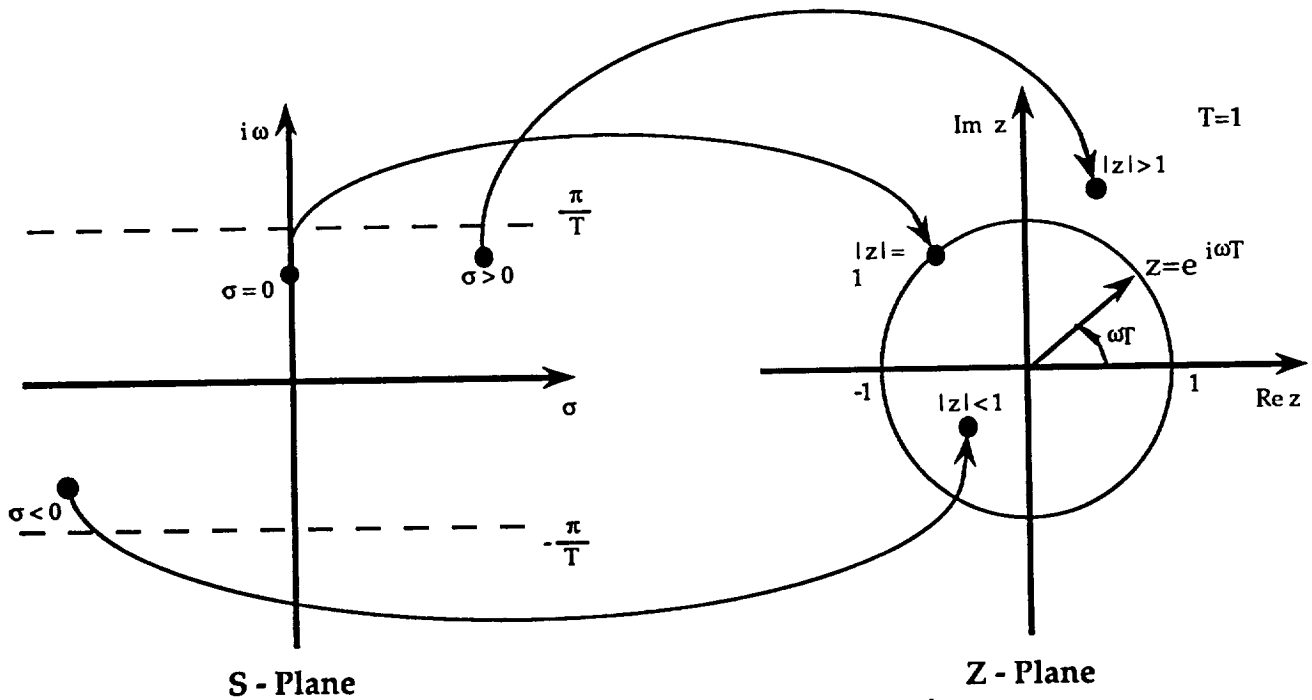


Fig 3.3.3-1. Mapping from the S Plane to the Z Plane

3.3.4 Digital Filter Design

In the second part of the spectral analysis of the flight data, digital filters are used to filter out the high energy spectras of the first few excitation frequencies. The design of such a digital filter (Ref 3.-5) begins with the specifications of an analog filter. The parameters for a filter are the cutoff frequency f_c , the stopband frequency f_s and the characteristics of the stop and passbands. These characteristics are used to generate the analog transfer function, $H(s)$, which is then converted to a digital filter transfer function, $H(z)$. This

conversion is done by a *bilinear transformation*, (BLT) . Once the analog filter characteristics have been defined, the BLT is initiated by

$$s = K \frac{1-z^{-1}}{1+z^{-1}} \quad (3.3.4-1)$$

where $s = \sigma + i\omega$. Depending on the manner in which the BLT is obtained , K can assume the values of 1, $\frac{1}{T}$ or $\frac{2}{T}$. We will use $\frac{1}{T}$. Solving (3.3.4-1) for z leads to

$$z = \frac{1+\sigma T}{1-\sigma T} = \dots = \frac{(1+\sigma T) + i\omega T}{(1-\sigma T) - i\omega T} \quad (3.3.4-2)$$

The phase, ϕ , and magnitude, $|z|$, of z are

$$|z| = \left[\frac{(1+\sigma T)^2 + (\omega T)^2}{(1-\sigma T)^2 + (\omega T)^2} \right]^{0.5} \quad (3.3.4-3)$$

and

$$\phi(z) = \tan^{-1} \frac{2\omega T}{1-(\sigma T)^2-(\omega T)^2} \quad (3.3.4-4)$$

The infinite-length i axis is mapped (nonlinearly) onto the unit circle, introducing a distortion of the frequency response. The distortion is in form of a relocation of the relevant frequencies: cutoff and stopbands. The general shape of the response is essentially unaffected, that is an analog lowpass filter will remain a digital lowpass filter, but with different cutoff and stopband frequencies. This shifting of the frequencies is shown in Fig. 3.3.4-1. The shifting of the frequencies during the transformation can be corrected by designing the analog filter to account for the warping due to the transformation. Then, when transformed, the frequencies will be at their desired locations. This prewarping can be accomplished by comparing the imaginary parts of the following equation that shows the relationship of $\omega=2\pi f$ in the s plane and the angle of z , $2\pi \Omega$ in the z plane, by evaluating z on the unit circle ($z = \exp(i 2 \pi \Omega)$) and inserting into (3.3.4-1):

$$\begin{aligned} s &= \frac{1}{T} \frac{1-e^{-i2\pi\Omega}}{1+e^{-i2\pi\Omega}} = \frac{1}{T} \frac{e^{i\pi\Omega} - e^{-i\pi\Omega}}{e^{i\pi\Omega} + e^{-i\pi\Omega}} \\ &= \frac{1}{T} \frac{i \sin \pi\Omega}{\cos \pi\Omega} = \frac{1}{T} i \tan \pi\Omega = \sigma + i\omega \quad (3.3.4-5) \end{aligned}$$

Comparing the imaginary parts gives us this nonlinear relation as

$$\omega = \frac{1}{T} \tan (\pi \Omega) \quad (3.3.4-6a)$$

or solved for Ω :

$$\Omega = \frac{1}{\pi} \arctan (\omega T) \quad (3.3.4-6b)$$

Thus to design a filter suitable for filtering DT data, the frequency component ω that you wish to filter must be expressed in the z domain variable Ω .

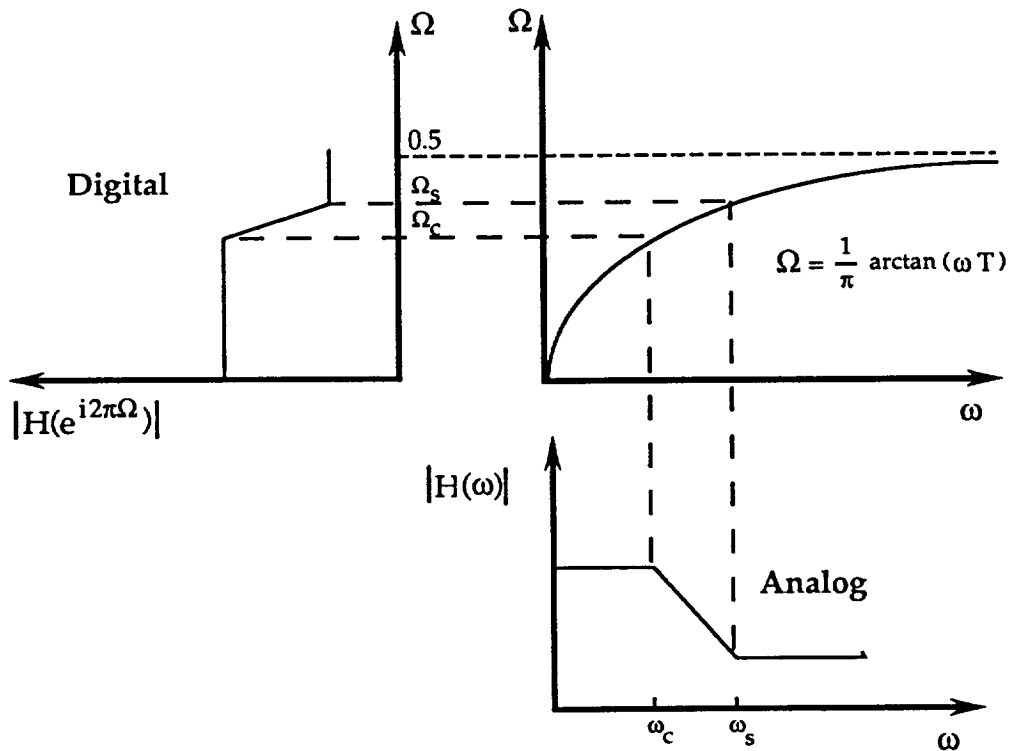


Fig. 3.3.4-1 Frequency Warping during the Z-Transform

3.3.5 Power Spectral Ratios

A section of the history of AZMRT that had little or no control inputs immediately before or during its interval was chosen to represent a steady state response. A spectral density of this steady state response was calculated and

related to an interval of the history that had a control input present or active, and the ratio of these were calculated. The sampling frequency, f_{samp} , of the data was 516.669 Hz, and so the spectra that could be examined was limited by the Nyquist frequency, $f_n = \frac{f_{\text{samp}}}{2} \cong 250$ Hz. This limitation was of no great importance, since the frequency band of interest was the interval from 0 to 50 Hz, containing the first two natural frequencies of the rotor system that we hoped were excited through a control input.

The first counter evaluated was 3110 and the time interval spanning 0 to 3.32 seconds (1200 datapoints) was taken to be the steady-state response. The history is shown in Fig.3.3.5-1a. Its spectral density is shown in Fig. 3.3.5-1b on a linear scale and in Fig. 3.3.5-1c on a logarithmic scale. The units for a power spectral density are [mean square/unit of frequency].

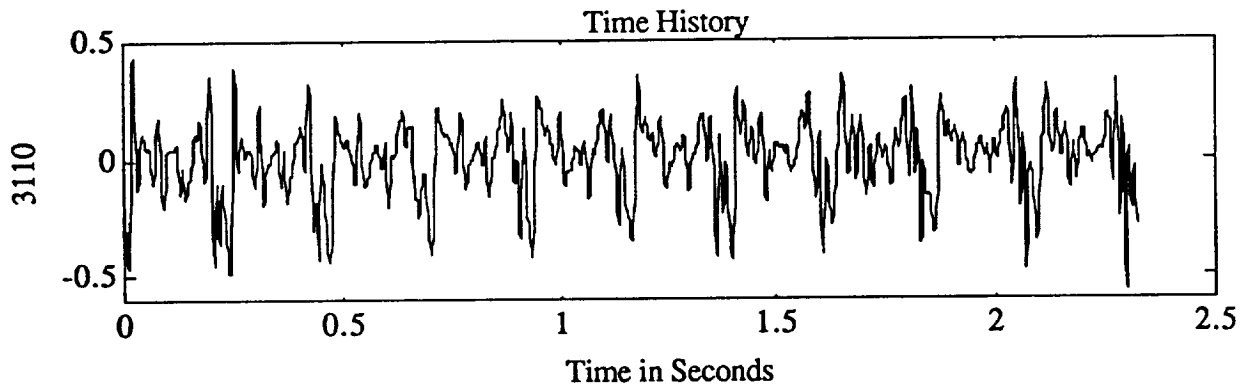


Fig 3.3.5-1a. Steady State Response (Ctr.3110)

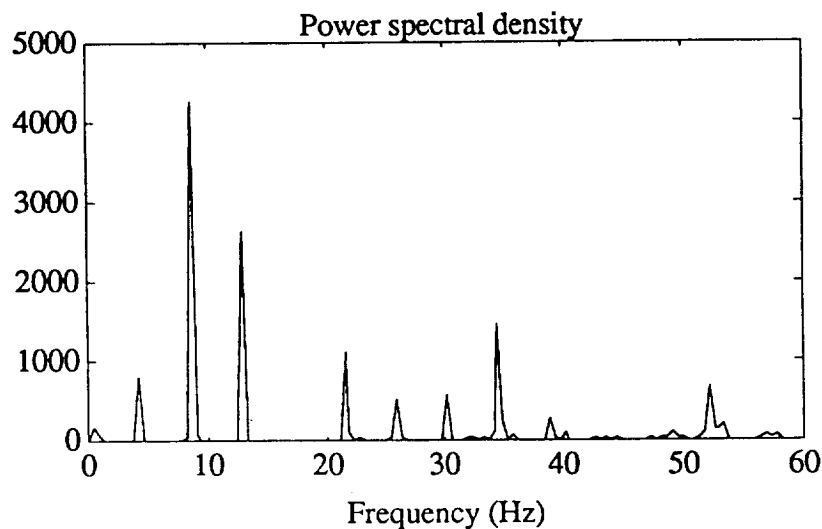


Fig 3.3.5-1a. Power Spectral Density of the Steady State Response (Ctr.3110)

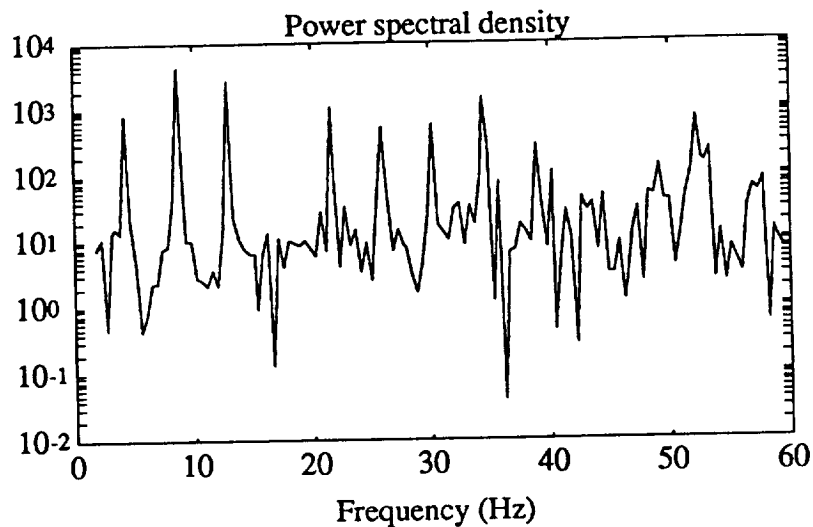


Fig 3.3.5-1b. Power Spectral Density of the Steady State Response (Ctr.3110)

Four different subsets (a) to d) of counter 3110 were selected that showed promise of containing some transient response to the control inputs. The datasets examined are depicted in Fig. 3.3.5-2. These datasets were spectrally analyzed and the ratio of these to the steady-state response were calculated. Fig. 3.3.5-3 shows the PSD of dataset a) on a linear scale, while Fig. 3.3.5-4 shows the same PSD on a logarithmic scale. Calculating the ratios of these datasets in a linear representation to the steady-state response is of course equivalent to a subtraction of these spectras on a logarithmic scale.

Fig. 3.3.5-5 to 3.3.5-9 show the ratios of the response spectras of the subsets a) to d) of counter 3110, with the ordinate showing the magnitude of increase in relation to the steady state response plotted against the frequency .

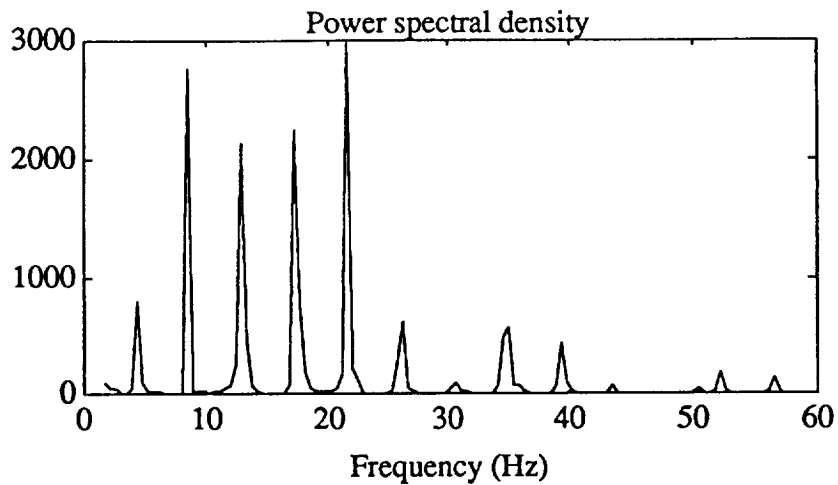


Fig. 3.3.5-3. PSD of Dataset a) (3110)

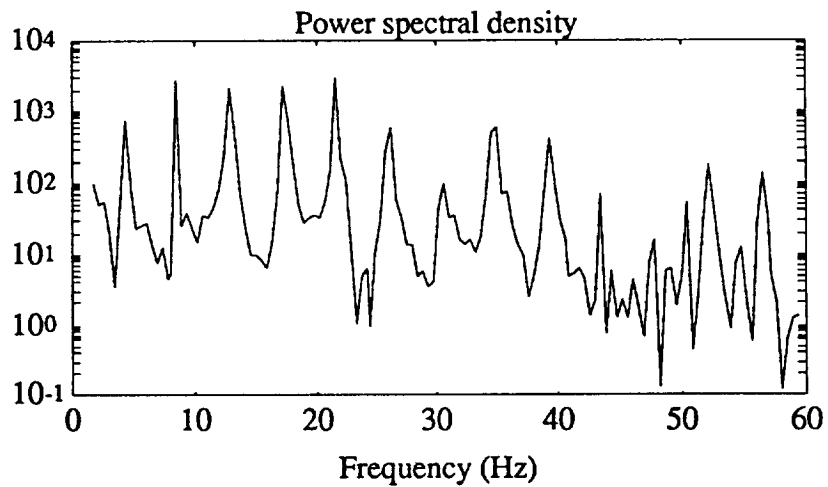


Fig. 3.3.5-4. PSD of Dataset a) (3110)

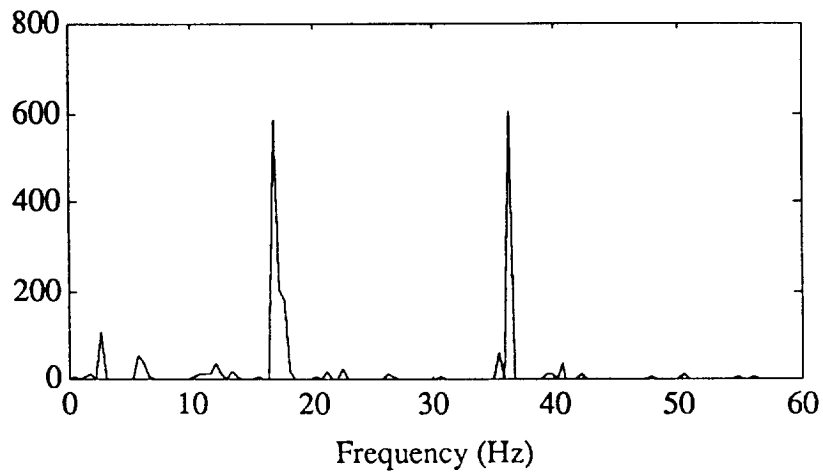


Fig. 3.3.5-5 Ratio of the PSD of a) to the Steady State Response (3110)

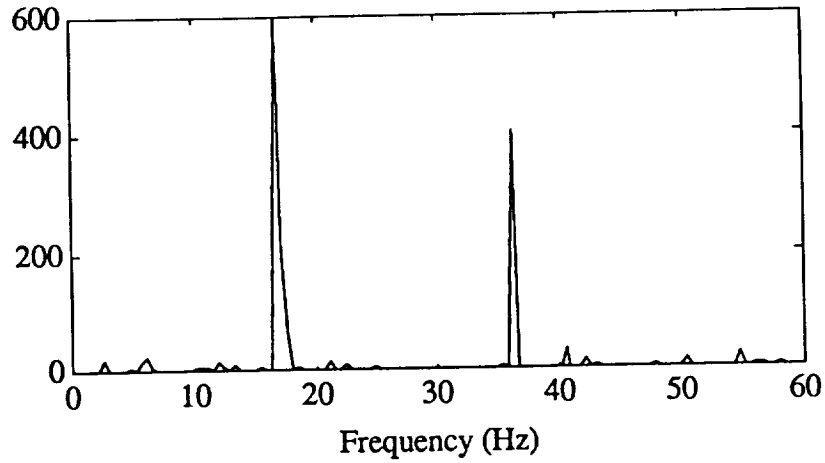


Fig. 3.3.5-6 Ratio of the PSD of b) to the Steady State Response (3110)

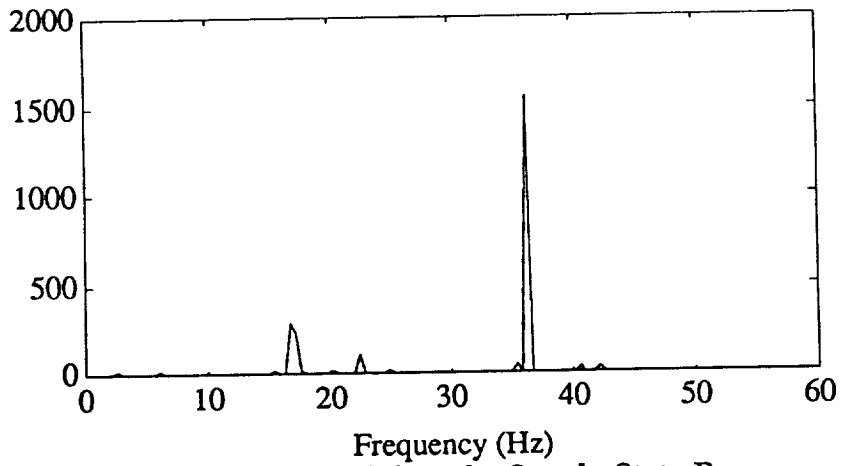


Fig. 3.3.5-7 Ratio of the PSD of c) to the Steady State Response (3110)

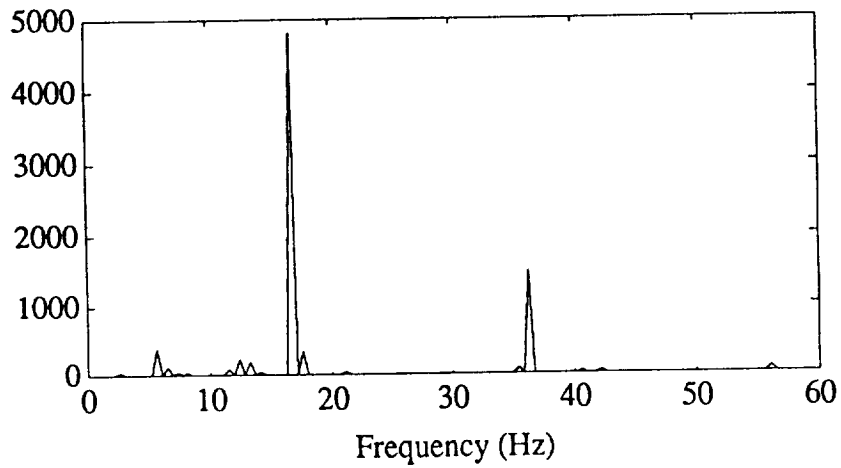


Fig. 3.3.5-8 Ratio of the PSD of d) to the Steady State Response (3110)

Figs. 3.3.5-5 to 3.3.5-7 all showed two peaks in the ratios of the PSD in a frequency ranges of 17.2-17.4 Hz and 36.5-36.8 Hz that were on the order of 600 to 5000 greater than at steady state. Increases at 1P, 2P and higher were also found due to an increase of energy at these intervals because of an increase in the aerodynamic forcing functions. 17.3 Hz is an integer multiple of the rotational speed (4P) but the increase in the PSD is far greater than the increases at 1P, 2P and 3P. The first natural mode was predicted at about 16 Hz, and it can be assumed that these peaks represent the transient responses of the excited first natural mode superposed with the expected excitation at 4P. The fact that the 4P excitation should be smaller in magnitude than the 1P, 2P and 3P excitation supports this observation. Fig.3.3.5-8 is missing this characteristic peak and the histories responsible for these PSD's are seen to be a steady state responses at a new energy level with the transients damped out. Table 3.3.5-1 shows the predicted first natural frequency of the rotor blade and the frequencies at which the peaks in the ratio of the PSD's were located along with the deviation.

Table 3.3.5-1 Predicted and suspected Location of the First Natural Frequency

Predicted Nat. Freq. [Hz] (1st/2nd)	Dataset	Location of Peak [Hz] (1st/2nd)	Deviation [%] (1st / 2nd)
16 / 40.9	a)	17.22 / 36.60	7.60 / -10.51
16 / 40.9	b)	17.23 / 35.91	7.70 / -13.19
16 / 40.9	c)	17.19 / 35.70	7.44 / -12.71
16 / 40.9	d)	17.10 / 36.60	8.87 / -10.51

The deviations remain at a more or less constant level which would point to a constant error in the rotating mode predictions.

The next counter evaluated was number 3108. The analysis technique was the same as for the previous counter. In an attempt to find and identify the second natural mode predicted at 40.9 Hz in this counter and to better examine the frequency band above 30 HZ, the frequency components at 1P, 2P... were removed by applying digital filters to the data.

The filtering scheme involved a Butterworth lowpass filter at 3 Hz and a highpass at 50 Hz, the other filters were designed as stopband filters of varying

bandwidths and intensities of the Butterworth (BW) and Chebycheff (CH) types. The combination of filters that showed the best results are shown in Table 3.3.5-2 and Fig 3.3.5-10.

Table 3.3.5-2 Filter Combination

Filter Type	Order	Bandwidth [Hz]	Passband Ripple	Times Filterd	Gain [dB]
Highp. BW	6	0 - 3	-	1	-
BW	3	2.04 - 4.04	-	2	-16.8
BW	5	6.83 - 10.83	-	2	-32.9
CH	6	12.12 - 14.12	0.5	3	-17.5
BW	5	16.90 - 18.40	-	3	-9.3
CH	8	19.82 - 23.82	0.5	2	-29.8
CH	8	24.11 - 28.11	0.5	2	-29.1
BW	6	37.1 - 41.1	-	1	-9.4
Lowp. CH	10	50 - ∞	0.1	1	

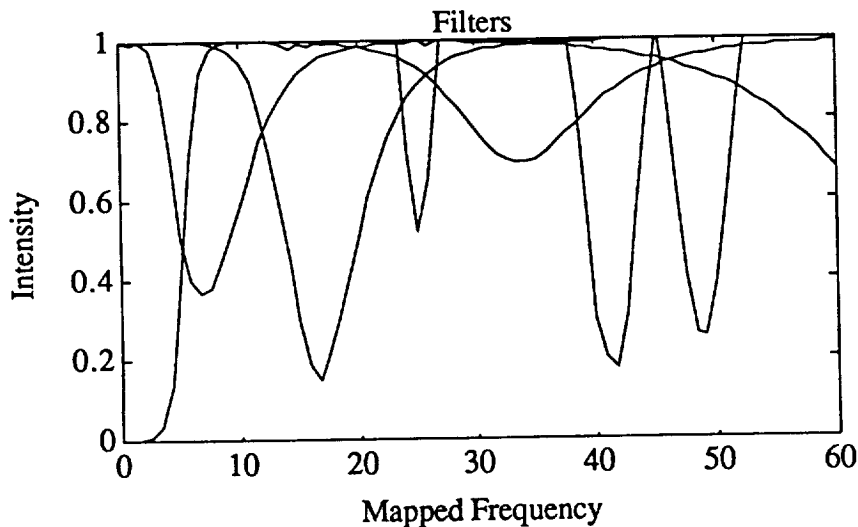


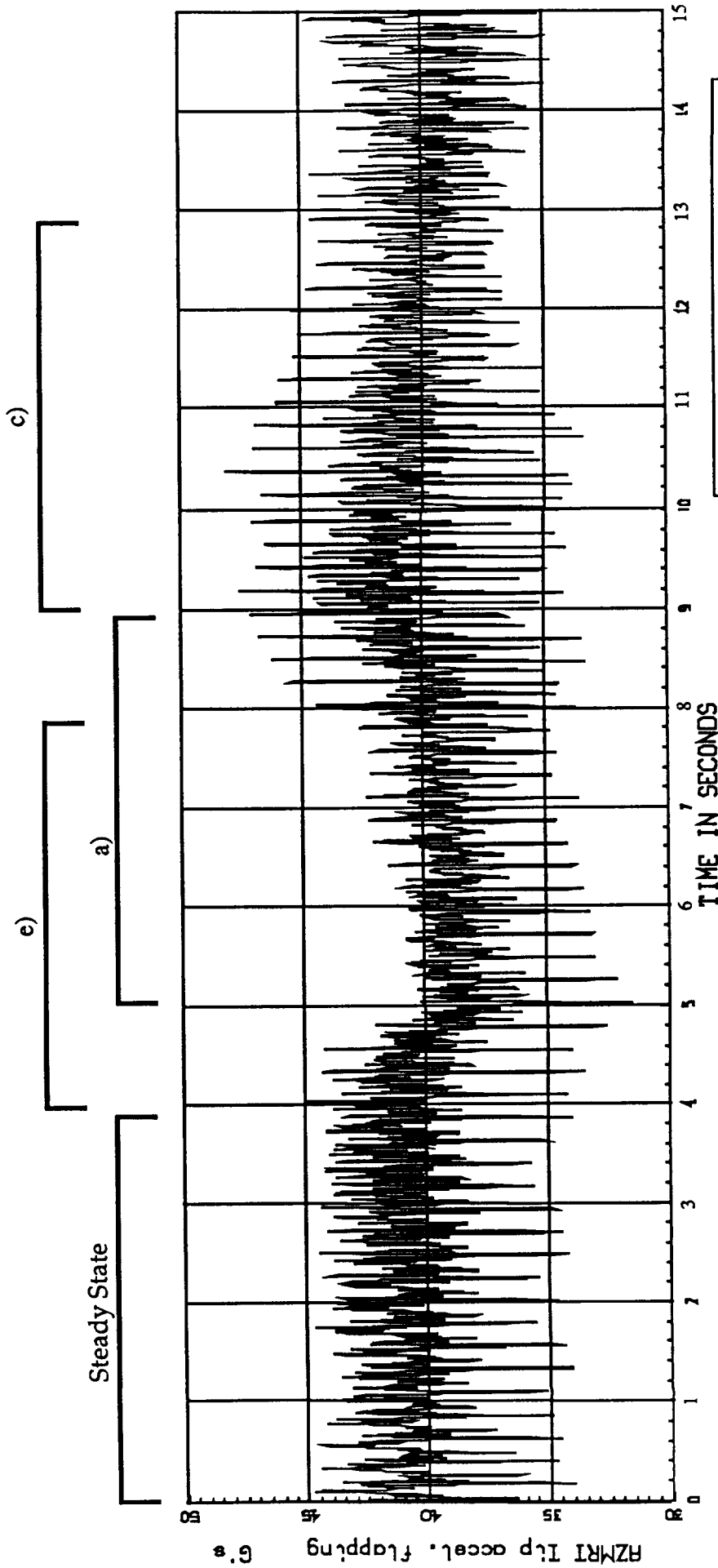
Fig. 3.3.5-10 Filter Combination

This time a larger time interval from 0 to 3.87 sec (2000 datapoints), was chosen to represent the steady-state response, since the second natural mode would tend to be damped out fairly quickly. Examining longer histories increases the chances of having some transient response of the second mode present in the data. The interval shown in Fig. 3.3.5-11a and Fig. 3.3.5-11b were filtered and then

examined for transient responses. This steady-state response is shown in Fig. 3.3.5-12a. Its spectral density is shown in Fig. 3.3.5-12b on a linear scale and in Fig. 3.3.5-12c on a logarithmic scale.

Again, the ratio of the transient response to the steady-state was calculated and plotted against the frequency. These ratios are shown in Figs. 3.3.5-13 to 3.3.5-18.

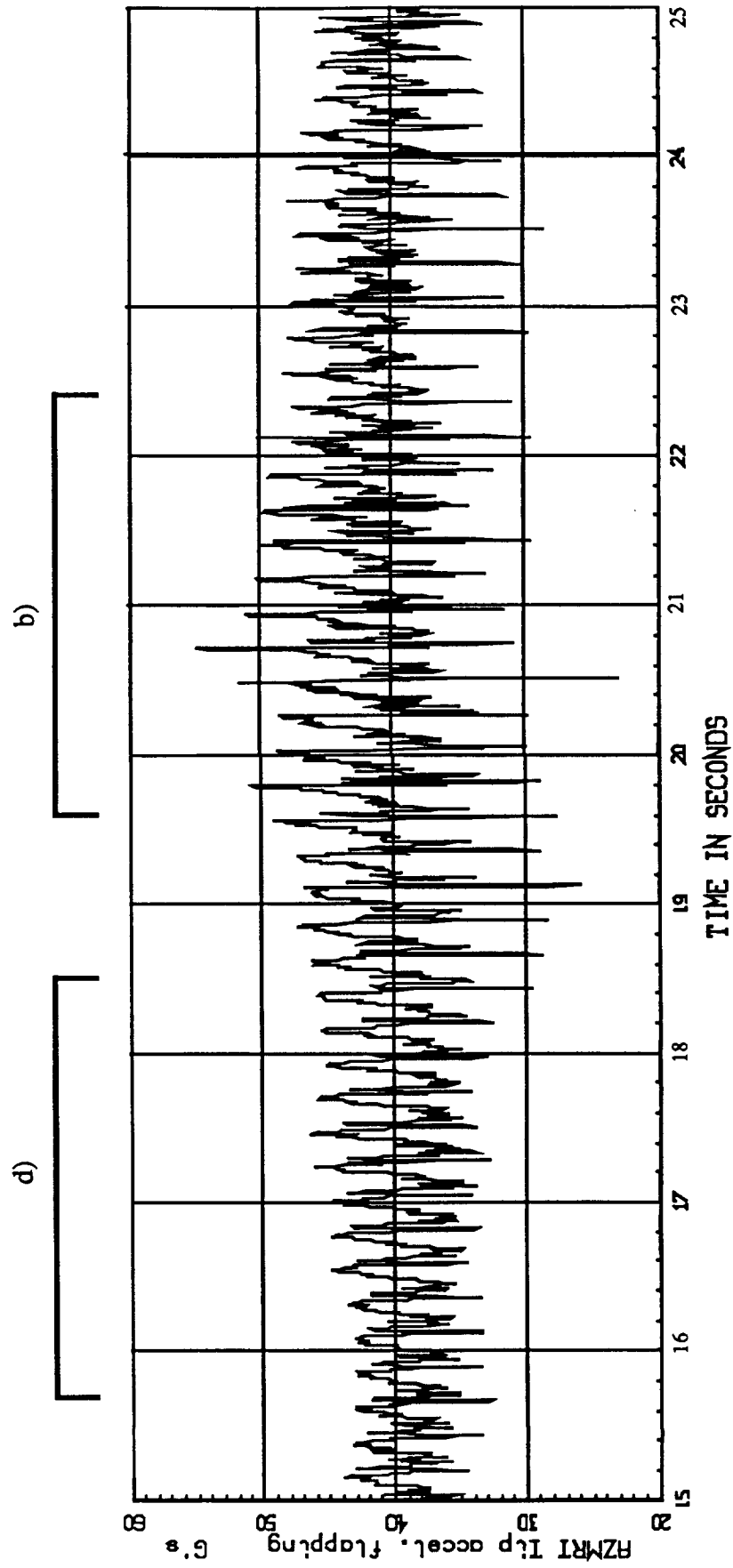
Flight 31, Counter 08
AZMRT



UH-60A A/C 748 PHASE I TESTS
FLT 31:81ME SWEET CONTROL INPUTS
CTR 3108: HOVER, LFT STICK SINE SWEEPS

Fig C.4.5-11a Examined Datasets

Flight 31, Counter 08
AZMRT



UH-60A A/C 748 PHASE I TESTS
FLT 31: 81NE SINEEP CONTROL INPUTS
CTR 3108: HOVER, LAT STICK SINE SINEEPS

Fig C.4.5-11b Examined Datasets

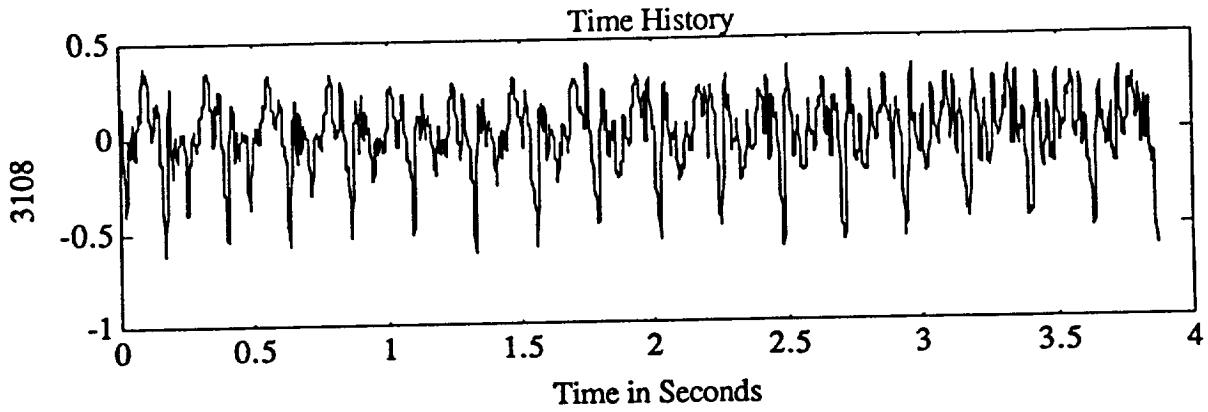


Fig 3.3.5-12a. Steady State Response (Ctr.3108)

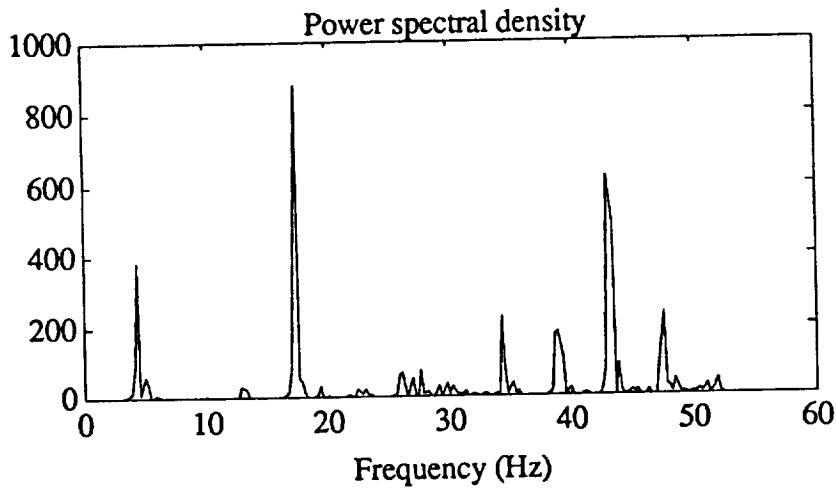


Fig 3.3.5-12b. PSD of the Filterd Steady State Response (Ctr.3108)

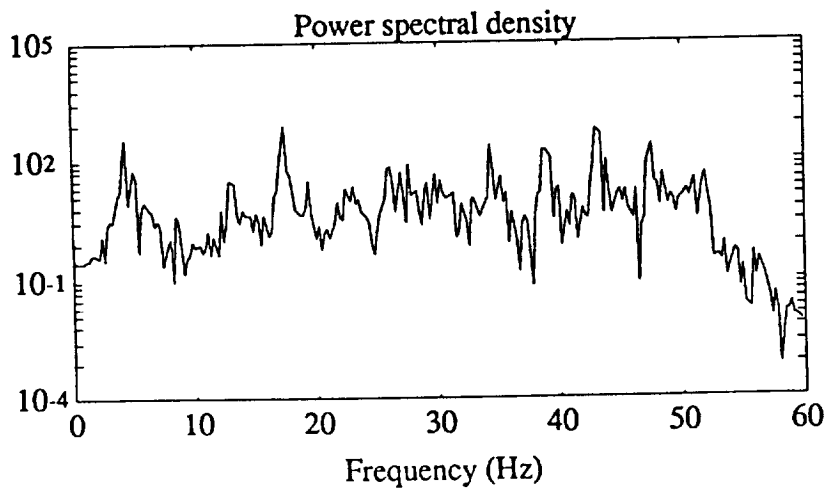


Fig 3.3.5-12c. PSD of the Filterd Steady State Response (Ctr.3108)

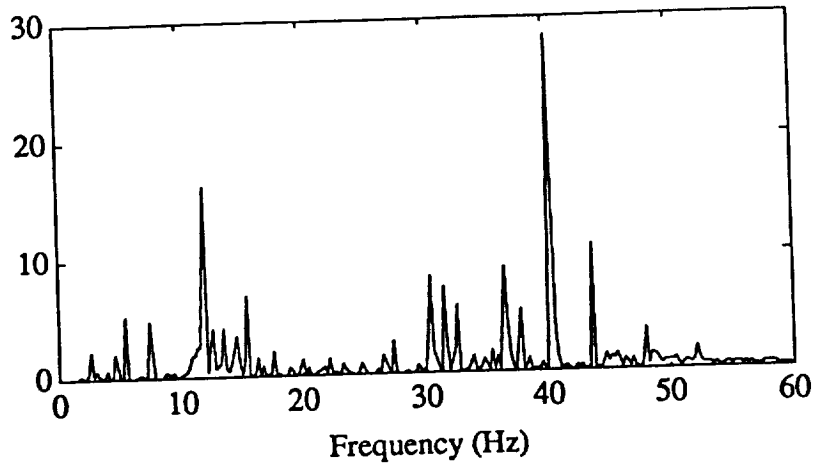


Fig. 3.3.5-13 Ratio of the PSD of a) to the Steady State Response (3108)

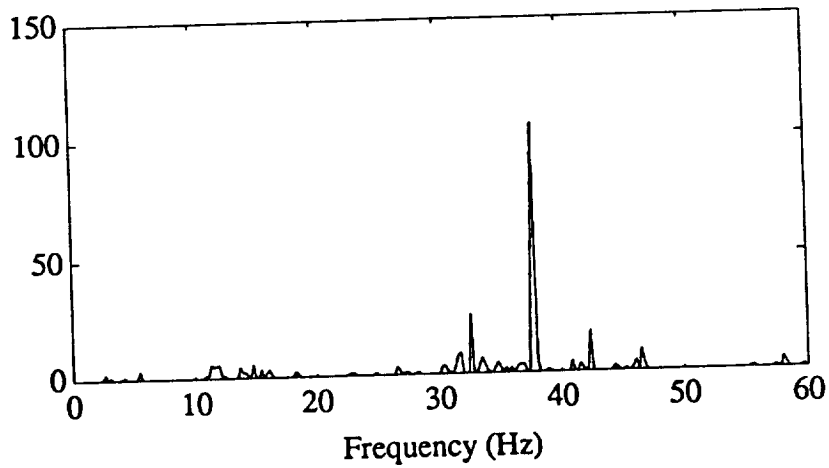


Fig. 3.3.5-14 Ratio of the PSD of b) to the Steady State Response (3108)

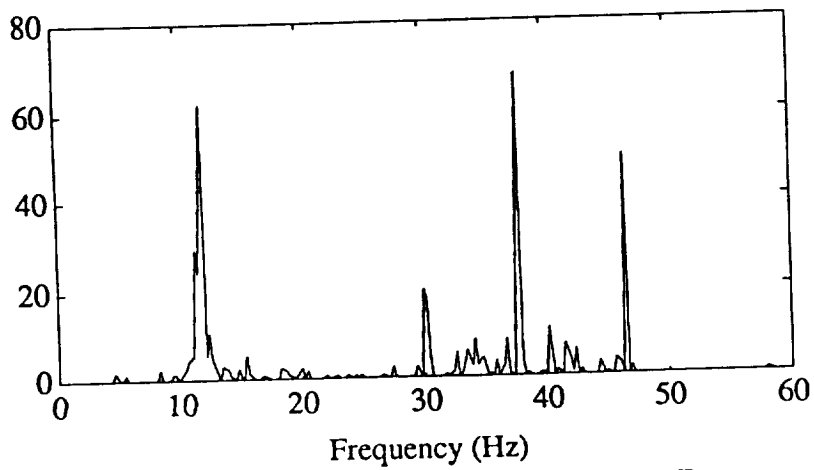


Fig. 3.3.5-15 Ratio of the PSD of c) to the Steady State Response (3108)

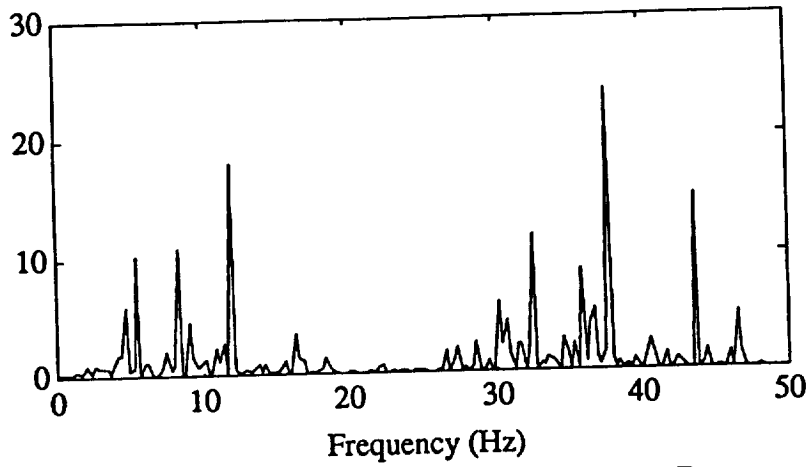


Fig. 3.3.5-16 Ratio of the PSD of d) to the Steady State Response (3108)

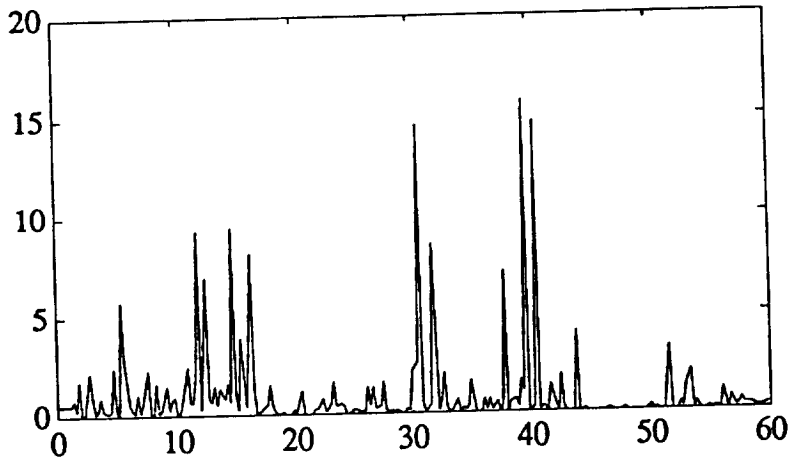


Fig. 3.3.5-17 Ratio of the PSD of e) to the Steady State Response (3108)

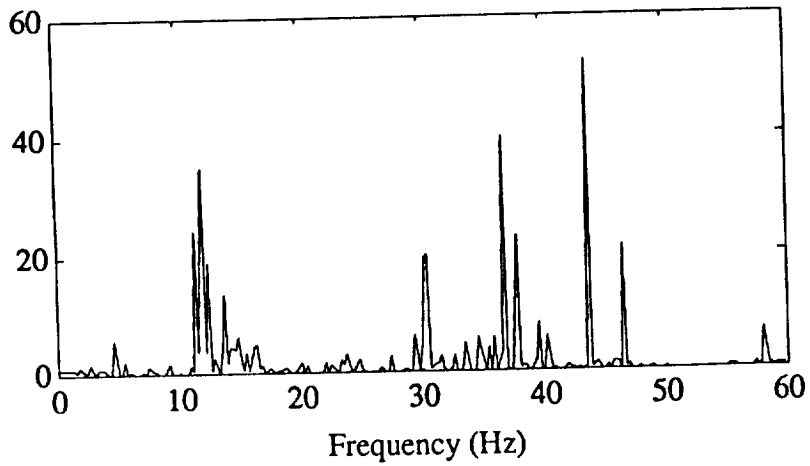


Fig. 3.3.5-18 Ratio of the PSD of f) to the Steady State Response (3108)

Discussion of the Power Spectral Density Ratios

All examined spectra ratios show a peak at the frequency interval of 37.9 to 40.7 Hz, except for the data subset f) that had a peak at 43.9 Hz. The magnitude increase is less than the increase for the previous dataset, since the filter at the 37-41 Hz band damped both the steady state and the transient responses with a gain of -9.4 dB. The increase turned out to be on the order of 15 to 100 opposed to the increase at counter 3110 of 600-5000. Again, the second natural frequency was expected to be at 40.9 Hz, and it can be assumed that the peaks visible in Figs. 3.3.5-13 to 3.3.5-18 are a result of this natural mode being excited. Table 3.3.6-1 shows the found and expected second natural frequency.

Table 3.3.6-1 Predicted and Measured 2nd Natural Frequency

Predicted Nat. Freq. (2 nd)	Dataset	Location of Peak (2 nd)	Deviation [%] (2 nd)
40.9	a)	40.56	-0.83
40.9	b)	37.97	-7.16
40.9	c)	38.24	-6.50
40.9	d)	37.97	-7.16
40.9	e)	39.65	-3.06
40.9	f)	43.92	7.38

Once again it is important to note that not all examined histories exhibited a peak in the frequency band of 39 to 41 Hz, but showed increases only in the frequency bands of 1P, 2P and up at varying intensities and power levels. This again would correspond to a new steady state response at a new energy level.

The results of the spectral energy analysis show great promise in being used to identify the transients of the natural modes buried in the response histories and warrant further examination. This analysis showed a definite presence of the first natural mode at about 17.2 Hz. The second mode was placed at 36.6 Hz for counter 3110 and at 37.9 Hz for counter 3108. Examining further counters in future research would lead to even better results, especially if the counters were cross-compared in some way. Another possibility would be to construct a transfer function for the assumed steady state response and one for the transient response and to draw conclusions from the different numerator

polynominals, since the denominator polynominals would have to be the same for the same system.

A reason that the predictions of the rotating natural modes are too high in general could be explained by Fig. 3.3.6-2. As the damping increases, the natural modes shift slightly to the lower end of the spectrum. Our analysis neglects damping effects, but in the case of the flight test measurements, aerodynamic as well as structural damping is present and may account for a phase shift.

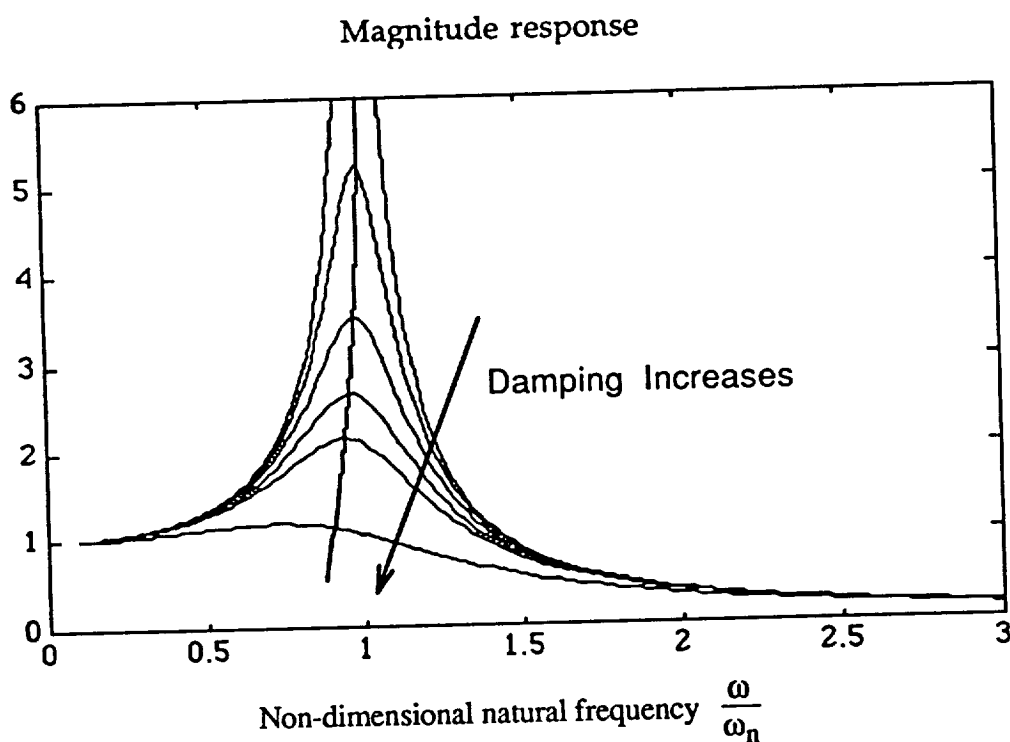
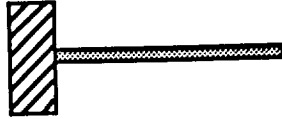


Fig. 3.3.6-2 Magnitude of Frequency - Response as a Function of Damping

Appendix A

Tables of the First Eigenvectors of Beams with Different Boundary
Conditions and Geometric Properties

Cantilevered Constant Beam



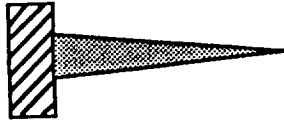
Coord	First Mode	Second Mode	Third Mode
0.0	0.00000	0.00000	0.00000
0.1	0.0167628	-0.0928322	0.229821
0.2	0.0638290	-0.301486	0.610493
0.3	0.136403	-0.527415	0.767384
0.4	0.229766	-0.685807	0.537735
0.5	0.339372	-0.717123	0.0292471
0.6	0.460966	-0.594037	-0.471250
0.7	0.590711	-0.322196	-0.666258
0.8	0.725340	0.0654301	-0.410146
0.9	0.862316	0.520821	0.216292
1.0	1.00000	1.00000	1.00000

Hinged Constant Beam



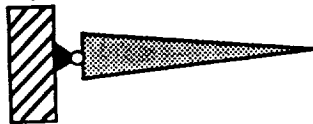
Coordinate	First Mode Rigid Body	Second Mode	Third Mode	Fourth Mode
0.00000	0.00000	0.00000	0.00000	0.00000
0.066667	0.066667	-0.176168	0.312006	-0.427397
0.133333	0.133333	-0.342705	0.581464	-0.734409
0.200000	0.200000	-0.484881	0.717196	-0.664977
0.266667	0.266667	-0.590631	0.687227	-0.283391
0.333333	0.333333	-0.651757	0.507443	0.203671
0.400000	0.400000	-0.663542	0.224895	0.580202
0.466667	0.466667	-0.624366	-0.0968230	0.701849
0.533333	0.533333	-0.535326	-0.390120	0.532819
0.600000	0.600000	-0.399852	-0.593871	0.146648
0.666667	0.666667	-0.223324	-0.661815	-0.301164
0.733333	0.733333	-0.0129609	-0.568864	-0.620699
0.800000	0.800000	0.223915	-0.315344	-0.647359
0.866667	0.866667	0.477577	0.0708468	-0.305840
0.933333	0.933333	0.738882	0.534149	0.329654
1.00000	1.00000	0.998499	0.993338	0.986899

Cantilevered Tapered Beam



Coor	First Mode (tapered)	Second Mode (tapered)	Third Mode (tapered)
0.0	0.00154295	-0.0156330	0.00672200
0.1	0.0147688	-0.0360000	0.0565879
0.2	0.0577830	-0.125706	0.174609
0.3	0.126396	-0.220433	0.201682
0.4	0.216554	-0.272842	0.0921422
0.5	0.324336	-0.251821	-0.0906786
0.6	0.445950	-0.141774	-0.232354
0.7	0.577741	0.0581017	-0.218733
0.8	0.716185	0.334526	0.0192293
0.9	0.857889	0.660860	0.467178
1.0	1.00000	1.00000	1.00000

Hinged Tapered Beam



Coord	First Mode Rigid Body	Second Mode	Third Mode	Fourth Mode
0.00000	0.00000	0.00000	0.00000	0.00000
0.066667	0.0666667	-0.0567526	0.0582599	-0.0548090
0.133333	0.133333	-0.108299	0.102849	-0.0847653
0.200000	0.200000	-0.144760	0.103761	-0.0385510
0.266667	0.266667	-0.159416	0.0594524	0.0438681
0.333333	0.333333	-0.148481	-0.0140151	0.102800
0.400000	0.400000	-0.110661	-0.0921840	0.0993520
0.466667	0.466667	-0.0466947	-0.149522	0.0312482
0.533333	0.533333	0.0410851	-0.164856	-0.0696861
0.600000	0.600000	0.149206	-0.124921	-0.151979
0.666667	0.666667	0.273503	-0.0260174	-0.164524
0.733333	0.733333	0.409567	0.126213	-0.0757709
0.800000	0.800000	0.553193	0.318904	0.114303
0.866667	0.866667	0.700830	0.539640	0.375812
0.933333	0.933333	0.850027	0.763966	0.670562
1.00000	1.00000	1.00000	1.00000	1.00000

Appendix B

Measured Residuals of the NASA - Shake Test
(1st 5 Flapping Modes)

1st Flap			
Accelerometer position	Residue (m=milli)	Accelerometer position	Residue (m=milli)
1	2.443	21	-1.611
2	1.520	22	-1.349
3	1.605	23	-1.362
4	1.046	24	-1.291
5	870.050m	25	-1.198
6	864.000m	26	-1.024
7	340.000m	27	-843.000m
8	259.000m	28	-776.000m
9	-113.000m	29	-480.300m
10	-259.110m	30	-484.000m
11	-468.700m	31	36.956m
12	-587.690m	32	-108.000m
13	-932.680m	33	358.937m
14	-986.740m	34	370.200m
15	-1.370	35	932.668m
16	-1.164	36	858.222m
17	-1.336	37	1.319
18	-1.407	38	
19	-1.409		
20	-1.361		

2nd Flap			
Accelerometer position	Residue (m=milli)	Accelerometer position	Residue (m=milli)
1	-1.810	21	-265.000m
2	-2.692	22	-955.800m
3	-610.000m	23	-1.015
4	-1.413	24	-1.773
5	440.500m	25	-1.441
6	-262.500m	26	-2.153
7	1.339	27	-1.722
8	661.246m	28	-2.219
9	2.256	29	-1.454
10	1.392	30	-2.192
11	2.500	31	-852.000m
12	1.857	32	-1.595
13	2.490	33	32.00m
14	1.718	34	-721.930m
15	2.210	35	1.053
16	1.485	36	499.600m
17	1.420	37	1.068
18	766.500m	38	-1.178
19	600.000m		
20	-115.430m		

3rd Flap			
Accelerometer position	Residue (m=milli)	Accelerometer position	Residue (m=milli)
1	4.040	21	1.715
2	3.530	22	2.220
3	976.000 m	23	552.00 m
4	726.000 m	24	1.297
5	-710.700 m	25	-856.000 m
6	-802.000 m	26	76.000 m
7	-1.864	27	-2.294
8	-1.940	28	-1.029
9	-2.240	29	-3.217
10	-2.153	30	-1.772
11	-1.736	31	-3.389
12	-1.605	32	-1.710
13	-705.000 m	33	-2.245
14	-407.000 m	34	-913.000 m
15	614.000 m	35	-895.000 m
16	926.000 m	36	572.000 m
17	1.589	37	741.7000 m
18	1.982	38	-2.132
19	2.175		
20	2.525		

4th Flap			
Accelerometer position	Residue (m=milli)	Accelerometer position	Residue (m=milli)
1	3.140	21	-2.306
2	2.356	22	-700.000m
3	1.660	23	-2.219
4	527.000m	24	-936.000m
5	393.000m	25	-2.763
6	-1.319	26	-420.000m
7	5.000m	27	-1.862
8	-1.425	28	534.000m
9	416.000m	29	-1.013
10	724.000m	30	1.521
11	1.530	31	-706.000m
12	306.000m	32	1.960
13	1.602	33	-1.250
14	1.132	34	1.642
15	1.408	35	-2.210
16	1.351	36	698.000m
17	425.000m	37	414.000m
18	874.000m	38	
19	-966.000m		
20	35.500m		

5th Flap			
Accelerometer position	Residue (m=milli)	Accelerometer position	Residue (m=milli)
1	-2.500	21	1.243
2	-2.983	22	783.000m
3	1.250	23	-1.081
4	-78.000m	24	-636.000m
5	3.040	25	-2.641
6	1.042	26	-1.497
7	2.880	27	-2.510
8	681.000m	28	-1.074
9	1.190	29	-1.060
10	-718.000m	30	370.000m
11	-408.000m	31	419.000m
12	-1.870	32	1.691
13	-498.000m	33	258.000m
14	-1.774	34	1.829
15	830.000m	35	-1.077
16	-559.000m	36	659.000m
17	2.349	37	709.000m
18	888.000m	38	
19	2.681		
20	1.466		

Appendix C

Finite Element Program for Rotating Structures
Example for Hinged UH- 60A Rotor Blade

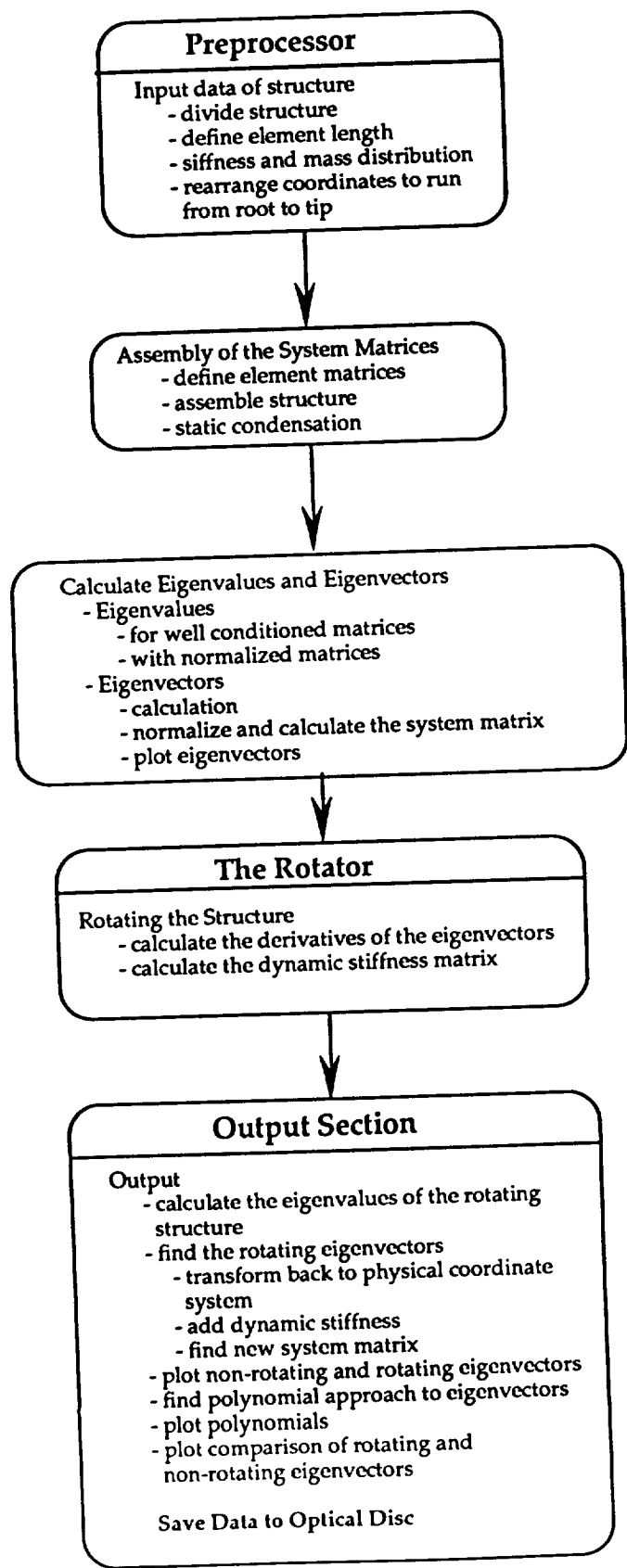
The Finite Element Program was written on a NeXT computer using the MATHEMATICA language (see Ref. C-6). The authors native language was German, so some of the internal variables are mnemonics derived from German. These are listed below to enhance understanding of the code. The variables used in the code are consistent to those in the report, Greek symbols are spelled out. All other variables are self-explanatory or are defined in the comments. Three different fonts were used in the listing to help discern between input, output and comments:

Code Text
Comment
 Output Text

Variables:

anzahl	parameter governing the amount of plots
PSI	rotational parameter Ψ
elementlaenge	length of the finite element
elementlaengez	as above, in reference frame "z"
ort	location along the blade or beam
mquerz, mquer	mass distribution [$\frac{kg}{m}$]
ne, n	number of elements
kele, kstr	part of the element (ele) and the structure (str) stiffness matrix
mele, mstr	see above, with mass matrix
schleife	loop variable
aktele	current element
zwischen, zw	an intermediate result
letztespalte	last column
kuudach	\hat{K}_{uu} , reduced stiffness matrix
mue	μ
teiler	divisor
bild	picture
nust	numerical derivative of u, the eigenvector
mnust	matrix of the above
lges	total length

Structure of Example Program



PREPROCESSOR BEGINNING

Th. Breitfeld 1990

DATA

Parameter

anzahl=5;

number of modes to be considered : modes

modes=5

PSI=1.6;

Structuredata

The Blade is divided into 3 Parts

Part 1 : 0....2.0 m (n1 Elements)

Part 2 : 2.0....6.0 m (n2 Elements)

Part 3 : 6.0 7.29 m (n3 Elements)

Tip of Blade: xi=0

of Elements : n

l1=1.29

l2=4

l3=2

Print[l1+l2+l3]

n1=25

n2=20

n3=25

n=n1+n2+n3

ne=n;

Lengths of the Single Elements

Part 1 (tip...)

ii=0;

Do[

ii=ii+1;

elementlaenge[ii]=l1/n1;

,{n1}]

Part 2

Do[

ii=ii+1;

elementlaenge[ii]=l2/n2;

,{n2}]

Part 3 (...root)

Do[

ii=ii+1;

elementlaenge[ii]=l3/n3;

,{n3}]

Coordinate Table xi (Tip....Root)

ii=.

Table[xi[ii]=0,{ii,1,n}];

xi[1]=N[elementlaenge[1]];

ort=1;

Do[

ort=ort+1;

xi[ort]=(xi[ort-1]+N[elementlaenge[ort]]);

,{n-1}]

Stiffness Tables [cm⁴]

ii=1;

"TIP VALUE";

While[xi[ii] <= .1016 , {i[ii]=308 10⁽⁻⁸⁾ , ii++}]
While[xi[ii] <= .2972 , {i[ii]=370 10⁽⁻⁸⁾ , ii++}]
While[xi[ii] <= .4928 , {i[ii]=614 10⁽⁻⁸⁾ , ii++}]
While[xi[ii] <= .8222 , {i[ii]=826 10⁽⁻⁸⁾ , ii++}]
While[xi[ii] <= 1.1516 , {i[ii]=929 10⁽⁻⁸⁾ , ii++}]
While[xi[ii] <= 1.5555 , {i[ii]=945 10⁽⁻⁸⁾ , ii++}]
While[xi[ii] <= 1.9594 , {i[ii]=978 10⁽⁻⁸⁾ , ii++}]
While[xi[ii] <= 2.3633 , {i[ii]=978 10⁽⁻⁸⁾ , ii++}]
While[xi[ii] <= 2.8075 , {i[ii]=978 10⁽⁻⁸⁾ , ii++}]
While[xi[ii] <= 3.2517 , {i[ii]=964 10⁽⁻⁸⁾ , ii++}]
While[xi[ii] <= 3.6959 , {i[ii]=961 10⁽⁻⁸⁾ , ii++}]
While[xi[ii] <= 4.1401 , {i[ii]=961 10⁽⁻⁸⁾ , ii++}]
While[xi[ii] <= 4.5668 , {i[ii]=933 10⁽⁻⁸⁾ , ii++}]
While[xi[ii] <= 4.9935 , {i[ii]=924 10⁽⁻⁸⁾ , ii++}]
While[xi[ii] <= 5.4202 , {i[ii]=924 10⁽⁻⁸⁾ , ii++}]
While[xi[ii] <= 5.8469 , {i[ii]=924 10⁽⁻⁸⁾ , ii++}]
While[xi[ii] <= 6.2736 , {i[ii]=924 10⁽⁻⁸⁾ , ii++}]
While[xi[ii] <= 6.9086 , {i[ii]=1149 10⁽⁻⁸⁾ , ii++}]
While[xi[ii] <= 7.3531 , {i[ii]=3900 10⁽⁻⁸⁾ , ii++}]

"ROOT VALUE";

Mass Tables [kg/m]

ii=1;

"TIP VALUE";

While[xi[ii] <= .1016 , {mquer[ii]=3.99 , ii++}]
While[xi[ii] <= .2972 , {mquer[ii]=12.55 , ii++}]
While[xi[ii] <= .4928 , {mquer[ii]=16.75 , ii++}]
While[xi[ii] <= .8222 , {mquer[ii]=17.79 , ii++}]
While[xi[ii] <= 1.1516 , {mquer[ii]=16.27 , ii++}]
While[xi[ii] <= 1.5555 , {mquer[ii]=13.03 , ii++}]
While[xi[ii] <= 1.9594 , {mquer[ii]=13.1 , ii++}]
While[xi[ii] <= 2.3633 , {mquer[ii]=13.17 , ii++}]
While[xi[ii] <= 2.8075 , {mquer[ii]=11.65 , ii++}]
While[xi[ii] <= 3.2517 , {mquer[ii]=10.55 , ii++}]
While[xi[ii] <= 3.6959 , {mquer[ii]=10.41 , ii++}]
While[xi[ii] <= 4.1401 , {mquer[ii]=10.62 , ii++}]
While[xi[ii] <= 4.5668 , {mquer[ii]=10.34 , ii++}]
While[xi[ii] <= 4.9935 , {mquer[ii]=10.34 , ii++}]
While[xi[ii] <= 5.4202 , {mquer[ii]=10.34 , ii++}]
While[xi[ii] <= 5.8469 , {mquer[ii]=10.20 , ii++}]
While[xi[ii] <= 6.2736 , {mquer[ii]=10.27 , ii++}]
While[xi[ii] <= 6.9086 , {mquer[ii]=10.34 , ii++}]
While[xi[ii] <= 7.3531 , {mquer[ii]=30.06 , ii++}]

"ROOT VALUE";

Testdata

ro=7800

ii=0;

Do[

ii=ii+1;

e[ii]=0.68 10¹¹;

,{n}]

The Coordinate Shuffler

xi - tip.....root changes to xi - root...tip

x -root...tip

ii=.

Table[x[ii]=0,{ii,1,n}];

ii=0;

Do[

ii=ii+1;

x[ii]=(l1+l2+l3)-xi[ne-ii];

,{n-1}]

x[ne]= l1+l2+l3;

ii=0;

Do[

ii=ii+1;

xi[ii]=x[ii];

,{n}]

Renumber the values for stiffness and mass and elementlength...

ii=0;

Do[

ii=ii+1;

iz[ii]=i[ne+1-ii];

mquerz[ii]=mquer[ne+1-ii];

elementlaengez[ii]=elementlaenge[ne+1-ii];

,{n}]

Back to the org. names

ii=0;

Do[

ii=ii+1;

i[ii]=iz[ii];

mquer[ii]=mquerz[ii];

elementlaenge[ii]=elementlaengez[ii];

,{n}]

Hinged-Free

dof=n 2 +1

ne=n;

PREPROCESSOR END

Assembly of the FEM-Stiffnessmatrix

Element stiffness matrix

ne= number of the element

" 4x4 matrix ";

```
kel=Array[kele,{4,4}];
```

```
kele[1,1]=12 a  
kele[1,2]=6 elementlaenge[aktele]a  
kele[1,3]=-12 a  
kele[1,4]=6 elementlaenge[aktele]a  
kele[2,2]=4 elementlaenge[aktele] elementlaenge[aktele] a  
kele[2,3]=-6 elementlaenge[aktele]a  
kele[2,4]=2 elementlaenge[aktele] elementlaenge[aktele]a  
kele[3,3]=12 a  
kele[3,4]=-6 elementlaenge[aktele]a  
kele[4,4]=4 elementlaenge[aktele] elementlaenge[aktele]a;  
run=1;
```

```
Do[  
  run=run+1;  
  ll=run-1;  
  schleife=0;  
  Do[  
    schleife=schleife+1;  
    kel[[run,schleife]]=kel[[schleife,run]];  
    ,{ll};  
  ],{3}];
```

Assembly of the Structure

Set kstr to zero

```
kstr=Array[kst,{dof,dof}];
```

```
run=0;
```

```
schleife=0;
```

```
Do[
```

```
  schleife=0;
```

```
  run=run+1;
```

```
  Do[
```

```
    schleife=schleife+1;
```

```
    kstr[[run,schleife]]=0;
```

```
  ],{dof}
```

```
  ],{dof}];
```

first element (hinged boundary conditions)

```
aktele=1;
```

```
a=e[aktele] i[aktele]/(elementlaenge[aktele]^3);
```

```
kstr[[1,1]]=kel[[2,2]]
```

```
kstr[[1,2]]=kel[[2,3]]
```

```
kstr[[1,3]]=kel[[2,4]]
```

```
kstr[[2,2]]=kel[[3,3]]
```

```
kstr[[2,3]]=kel[[3,4]]
```

```
kstr[[3,3]]=kel[[4,4]];
```

second until n-th element

```
run=1;
faktor=-2;
Do[
    run=run+1;
    aktele=run;
    faktor=faktor+1;
    index=aktele+faktor+1;
    a=e[aktele] i[aktele]/(elementlaenge[aktele]^3);
    kstr[[index,index]]=kstr[[index,index]]+kel[[1,1]];
    kstr[[index,index+1]]=kstr[[index,index+1]]+kel[[1,2]];
    kstr[[index,index+2]]=kstr[[index,index+2]]+kel[[1,3]];
    kstr[[index,index+3]]=kstr[[index,index+3]]+kel[[1,4]];
    kstr[[index+1,index+1]]=kstr[[index+1,index+1]]+kel[[2,2]];
    kstr[[index+1,index+2]]=kstr[[index+1,index+2]]+kel[[2,3]];
    kstr[[index+1,index+3]]=kstr[[index+1,index+3]]+kel[[2,4]];
    kstr[[index+2,index+2]]=kstr[[index+2,index+2]]+kel[[3,3]];
    kstr[[index+2,index+3]]=kstr[[index+2,index+3]]+kel[[3,4]];
    kstr[[index+3,index+3]]=kstr[[index+3,index+3]]+kel[[4,4]];
    ,(ne-1)]
Symmetry
matrix=kstr;
zwischen=Transpose[matrix];
matrix=matrix+zwischen;
ii=0;
Do[
    ii=ii+1;
    matrix[[ii,ii]]=matrix[[ii,ii]]-zwischen[[ii,ii]];
    ,(dof)];
kstr=matrix;
Assembly of the mass matrix
Set mel to zero
run=0;
schleife=0;
Do[
    schleife=0;
    run=run+1;
    Do[
        schleife=schleife+1;
        mel[[run,schleife]]=0;
        ,(4)]
    ,(4)];
aktele=.;
mel[[1,1]]=mquer[aktele] elementlaenge[aktele]/2;
mel[[3,3]]=mquer[aktele] elementlaenge[aktele]/2;
set mstr to zero
mstr=Array[mst,{dof,dof}];
```

```

run=0;
schleife=0;
Do[
    schleife=0;
    run=run+1;
    Do[
        schleife=schleife+1;
        mstr[[run,schleife]]=0;
    ,(dof)]
,(dof)];
first element (Cantilever boundary conditions)
aktele=1;
mstr[[1,1]]=mel[[2,2]]
mstr[[2,2]]=mel[[3,3]];
second until n-th element
run=1;
faktor=-2;
Do[
    run=run+1;
    aktele=run;
    faktor=faktor+1;
    index=aktele+faktor+1;
    mstr[[index,index]]=mstr[[index,index]]+mel[[1,1]];
    mstr[[index+1,index+1]]=mstr[[index+1,index+1]]+mel[[2,2]];
    mstr[[index+2,index+2]]=mstr[[index+2,index+2]]+mel[[3,3]];
    mstr[[index+3,index+3]]=mstr[[index+3,index+3]]+mel[[4,4]];
,(ne-1)];
Static Condensation
Massmatrix
Rearrange the DOFs
(Rearrange Elements Naturally And Transform Equations
to Reduced Stiffness matrices)
m=Array[mm,{dof,dof}];
run=0;
schleife=0;
Do[
    schleife=0;
    run=run+1;
    Do[
        schleife=schleife+1;
        m[[run,schleife]]=0;
    ,(dof)]
,(dof)];
columns
run=1;
index=1;
Do[
    m[[index]]=mstr[[run+1]];
    index=index+1;
    run=run+2

```

```

,{(dof+1)/2-1});
rows
run=0;
Do[
    run=run+1;
    m[[run,run]]=m[[run,(2 run)]];
    m[[run,(2 run)]] = 0;
,(((dof+1)/2)-1)]
Structurematrix
rearrange the DOFs
k=Array[kk,{dof,dof};
run=0;
schleife=0;
Do[
    schleife=0;
    run=run+1;
    Do[
        schleife=schleife+1;
        k[[run,schleife]]=0;
    ,{dof}]
,{dof}];
rows, colls
letztespalte=kstr[[dof]];
run=0;
Do[
    run=run+1;
    k[[((dof+1)/2-1)+run]]=kstr[[2 run -1]];
    k[[run]]=kstr[[2 run)];
,((dof-1)/2)];
k[[dof]]=letztespalte;
kstr=Transpose[k];
letztespalte=kstr[[dof]];
run=0;
Do[
    run=run+1;
    k[[((dof+1)/2-1)+run]]=kstr[[2 run -1]];
    k[[run]]=kstr[[2 run)];
,((dof-1)/2)];
k[[dof]]=letztespalte;
k=Transpose[k];
Condensation
Massmatrix
remove zeros
ii=0;
Do[
    ii=ii+1;
    list=m[[ii]];
    zw=Partition[list,(dof-1)/2];
    m[[ii]]=zw[[1]];

```

```

,((dof-1)/2});
ii=;
m=Table[m[[ii]],{ii,1,(dof-1)/2}];
Stiffness matrix
zw=Array[zz,{dof,dof}];
the following variables correspond to those in chapter 2.1.5 in their notation
kuu=Array[uu,{(dof-1)/2,(dof-1)/2}];
kuf=Array[uf,{(dof+1)/2,(dof-1)/2}];
kfu=Array[fu,{(dof-1)/2,(dof+1)/2}];
kff=Array[ff,{(dof+1)/2,(dof+1)/2}];
ii=0;
Do[
    ii=ii+1;
    zw[[ii]]=Partition[k[[ii]],(dof-1)/2];
,{dof}];
ii=0;
Do[
    ii=ii+1;
    kuu[[ii]]=zw[[ii]][[1]];
,{(dof-1)/2}];

ii=0;
Do[
    ii=ii+1;
    kuf[[ii]]=zw[[ii+(dof-1)/2]][[1]];
,{(dof+1)/2}];
ii=0;
Do[
    ii=ii+1;
    rot[[ii]]=RotateLeft[k[[ii]],(dof-1)/2];
    zw[[ii]]=Partition[rot[[ii]],(dof+1)/2];
,{dof}];
ii=0;
Do[
    ii=ii+1;
    kfu[[ii]]=zw[[ii]][[1]];
,{(dof-1)/2}];
ii=0;
Do[
    ii=ii+1;
    kff[[ii]]=zw[[((dof-1)/2)+ii]][[1]];
,{(dof+1)/2}];
The reduced Stiffness matrix;
kuudach= kuu- Transpose[kuf] . Inverse[kff] . kuf;
k=kuudach;
dof=(dof-1)/2;

```

Search for the Eigenvalues

Normal Apprch (well conditioned matrix)

```
mm=Inverse[m];
```

```
eig=Eigenvalues[k . mm];
```

```
eig^.5;
```

With the normalized matrices

the letter "n" or the preposition "norm" depicts a normalized entity...

```
matrix=.
```

```
matrix=k
```

```
dmatrix= matrix Transpose[matrix]
```

```
lamdas=Eigenvalues[dmatrix]
```

```
qnorm=Max[lamdas]
```

```
knorm=qnorm^.5
```

```
nk=matrix 1/knorm
```

```
Min[Abs[Eigenvalues[nk]]]
```

if this value is << 1 ,then the matrix is indeed singular

```
matrix=.
```

```
matrix=m
```

```
dmatrix= matrix Transpose[matrix]
```

```
lamdas=Eigenvalues[dmatrix]
```

```
qnorm=Max[lamdas]
```

```
mnorm=qnorm^.5
```

```
nm=matrix 1/mnorm;
```

```
nmm=Inverse[nm];
```

```
nk . nmm;
```

```
mue=Eigenvalues[%];
```

```
lamq=mue knorm/mnorm;
```

```
%.5
```

lower eigenvalues (roots) belong to the lower eigenfunctions

```
roots=lamq;
```

Reinsertion of the Eigenvalues into the matrices

```
lamq=.
```

```
eigprob=k - lamq IdentityMatrix[dof] m;
```

```
ii=0;
```

```
Do[
```

```
  ii=ii+1;
```

```
  lamq=roots[[dof+1-ii]];
```

```
  {d,p}=Eigensystem [eigprob];
```

```
  y=Table[0,{dof}];
```

"the lowest term of "d" must be found, sothe correct position of y is set to 1 "

```
  pos=0;
```

```
  jj=1;
```

```
  tst=Abs[d];
```

```
    Do[
```

```
      If[{tst[{jj]}]==Min[tst],pos=jj,pos=pos];
```

```
      jj=jj+1;
```

```
    ],{dof}];
```

```

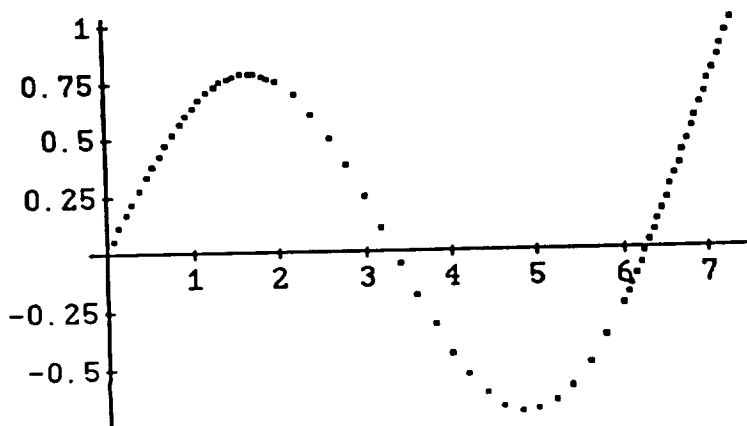
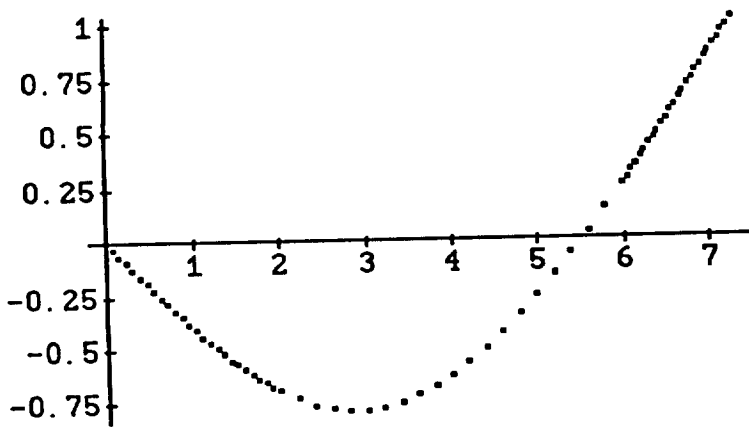
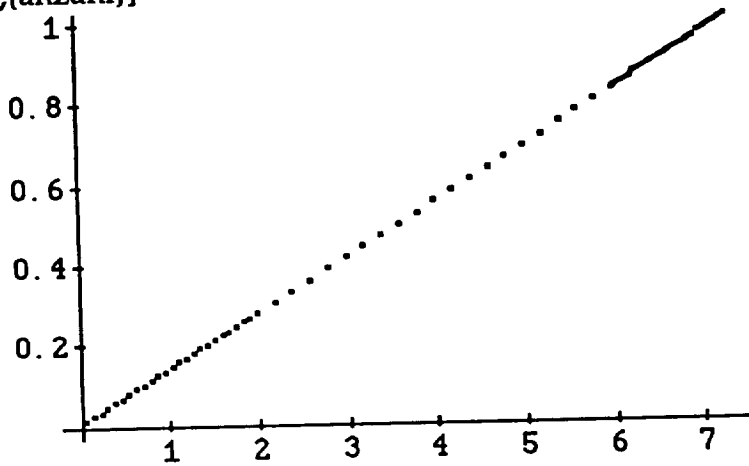
        y[[pos]]=1;
        u[ii]=y . p;
,{dof}
"Normalizing the eigenvectors"
run=0
Do[
    run=run+1;
    If[Abs[Max[u[run]]]>Abs[Min[u[run]]],teiler=Max[u[run]],teiler=Min[u[run]]
];
    u[run]=u[run] 1/teiler;
,{n}
precede the eigenvectors with a zero (for better plotting):
ii=0;
Do[
    ii=ii+1;
    akt=u[ii];
    uplot[ii]={0,akt};
    uplot[ii]=Flatten[uplot[ii]];
,{dof}];
Variables to this point;
u(i)          - normalised eigenvektors
uplot(i)      - normalised eigenvektors w/0 at beginning (for plotting)
polyu(i)      - polynomial apprch for the above
m             - kondensed mass matrix
k             -kondensed stiffness matrix
roots         - squares of the eigenfrequencies (==lamq)
dof           -degrees of freedom
n             -number of finite elements(==dof)
anzahl        -plotting parameter
Generalised Stiffness and Mass Matrix
ii=.
evek=Table[u[ii],[ii,1,dof]];
U=MatrixForm[evek];
UNORM=Transpose[evek];
mgen=Transpose[UNORM] . m . UNORM;
kgen=Transpose[UNORM] . k . UNORM;
omegaqu=Table[kgen[[nn,nn]]/mgen[[nn,nn]],{nn,1,n}];
% ^(.5)
draw the eigenvectors
run=0;
Do[
    run=run+1;
    "coordinate of the current element";
    xi[1]=elementlaenge[1];
    ort=1;
        Do[
            ort=ort+1;
            xi[ort]=xi[ort-1]+elementlaenge[ort];
        ,{n-1}];
    datapairs=Table[coords,{n}];

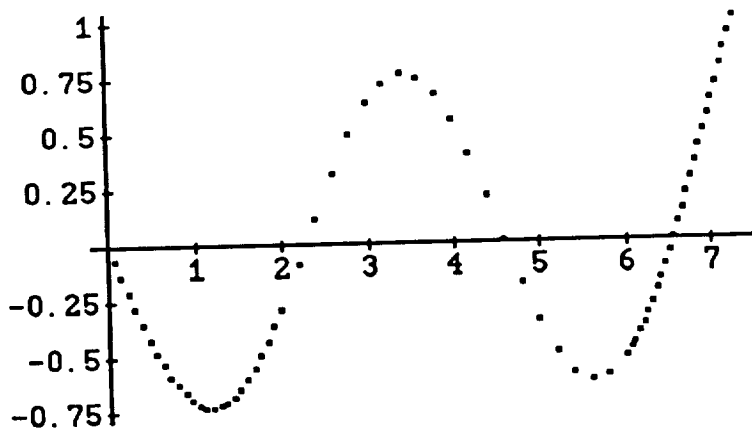
```

```

ii=0;
Do[
  ii=ii+1;
  datapairs[[ii]]={xi[ii],u[run][[ii]]};
  bild[run]=ListPlot[datapairs];
  ,{anzahl}]

```





and so on ...

The ROTATOR

The Derivatives of the Eigenvektors
 Procedure for obtaining the numerical derivatives

```

ii=0;
Do[
  ii=ii+1;
  mnust=Array[nust,{dof,dof}];
  deltax=1/n;
  "first";
  nust[ii,1]=u[ii][[1]] / ( xi[1]/lges);
  "last";
  nust[ii,dof]=(u[ii][[dof]]-u[ii][[dof-1]]) / ( xi[dof]/lges-xi[dof-1]/lges);
  "others";
  run=1;
  Do[
    run=run+1;
    nust[ii,run]=(u[ii][[run+1]]-u[ii][[run-1]]) / ( xi[run+1]/lges-xi[run-1]/lges);
    ,{dof-2}];
  ax[ii]=Table[nust[ii,kk],{kk,1,dof}];
,{modes}];
mnust=Array[ax,{modes}];

set gamma (n x n) = 0
schleife=0;
run=0;
Do[
  schleife=schleife+1;
  run=0;
  Do[
    run=run+1;
    gamma[schleife,run]=0;
  ,{n}];
,{n}
deltax=.

```

```

deltax[1]=xi[1]/lges;
deltax[n]=xi[n]/lges-xi[n-1]/lges;
ii=1;
Do[
    ii=ii+1;
    deltax[ii]=xi[ii+1]/lges-xi[ii]/lges;
,{n-2}]
check if sum of deltax=1
ii=.
Sum[deltax[ii],[ii,1,n]]

0.996104252400547

jj=.
mm=.;
mm=0;
rr=0;

Do[
    rr=rr+1;
    Print[rr];
    mm=0;
    Do[
        mm=mm+1;
        gamma[rr,mm]=Sum[m[[i,i]] xi[i]/lges Sum[mnust[[rr,jj]]
            mnust[[mm,jj]] deltax[jj], {jj,1,i}], {i,1,dof}];
    ,{modes}];
,{modes}];
1
2
3
4
5
Grm=Array[gamma,{dof,dof}];
omega=.;
kdyn=omega^2 Grm;

```

Output section

```

omega=0;
kges=kgen+kdyn;
kges . Inverse[mgen];
Eigenvalues[%];
freq=%^.5;
freq=Sort[%]
wn1=freq[[2]]

68.41862788567951

```

```

run=0;
Do[
  omega=(run 4/10)^.5 wn1;
  Print[N[run 4/10]];
  kges=kgen+kdyn ;
  z=kges . Inverse[mgen];
  tt=Eigenvalues[z];
  xx=tt^.5;
  xx=Sort[xx];
  Print[xx[[2]]];
  xxx=(xx[[2]]/wn1)^2;
  Print[xxx];
  Print[""];
  run=run+1;
  ,{6}]

```

```

0.
68.4186
1.

```

```

0.4
135.412
3.91711

```

```

0.8
178.192
6.7831

```

```

1.2
212.264
9.6251

```

```

1.6
241.444
12.4533

```

```

2.
267.382
15.2727

```

```

omega=0;
kges=kgen+kdyn;
z=kges . Inverse[mgen];
Eigenvalues[z];

```

```

freq=%^.5;
freq=Sort[%]
wn2=freq[[3]]

```

```

225.3581507539162

```

```

run=0;
Do[
  omega=(run 4/10)^.5 wn1;
  Print[N[run 4/10]];
  kges=kgen+kdyn ;
  z=kges . Inverse[mgen];
  tt=Eigenvalues[z];
  xx=tt^.5;
  xx=Sort[xx];
  Print[xx[[3]];

  xxx=(xx[[3]]/wn2)^2;
  Print[xxx];
  Print[""];
  run=run+1;
, {6}]

```

```

0.
225.358
1.

```

```

0.4
297.736
1.74549

```

```

0.8
354.318
2.47195

```

```

1.2
402.216
3.18545

```

```

1.6
444.465
3.88981

```

```

2.
482.682
4.58749

```

Find the Rotating Eigenforms

wn1

68.41862788567951

Rotational Speed

omega=PSI^.5 wn1

86.5434794009031

ii=.

UNORM=Transpose[Table[u[ii],{ii,1,dof}]];

```

tb1=Inverse[Transpose[UNORM]] . kgen . Inverse[UNORM];
tb2=Inverse[Transpose[UNORM]] . kdyn . Inverse[UNORM];
tbges=tb1+tb2;
tbmass=Inverse[Transpose[UNORM]] . mgen . Inverse[UNORM];
c=Inverse[tbges];
d=c.tbmass;
{eval,evek}=Eigensystem[d];

Urot=Transpose[evek];
"Urot=strukturmatrix (not Normalized)"
"urot[i]=Eigenvektorens (rotating) "
run=0
Do[
run=run+1;
urot[run]=evek[[run]];
MatrixForm[urot[run]];
,{n}
"Normalizing"
run=0
Do[
run=run+1;
If[Abs[Max[urot[run]]]>Abs[Min[urot[run]]],teiler=Max[urot[run]],teiler=Min[urot[run]]];
urot[run]=urot[run]/teiler
,{n}

"formulate the rotating structure matrix"
run=0;
Do[
run=run+1;
zwischen=Table[urot[nn],{nn,1,n}];
,{n}
UNORM=MatrixForm[Transpose[zwisch]];
mgenrot=Transpose[Urot] . tbmass . Urot
mgenrot=Table[If[mgenrot[[kk,j]]<10^(-10),0,mgenrot[[kk,j]]],{kk,n},{j,n}]
MatrixForm[mgenrot];
kgenrot=Transpose[Urot] . tbges . Urot
kgenrot=Table[If[kgenrot[[kk,j]]<10^(-6),0,kgenrot[[kk,j]]],{kk,n},{j,n}]

MatrixForm[kgenrot];

omegaqurot=Table[kgenrot[[nn,nn]]/mgenrot[[nn,nn]],{nn,1,n}];
Sort[% ^(.5)]

(1/eval)^.5

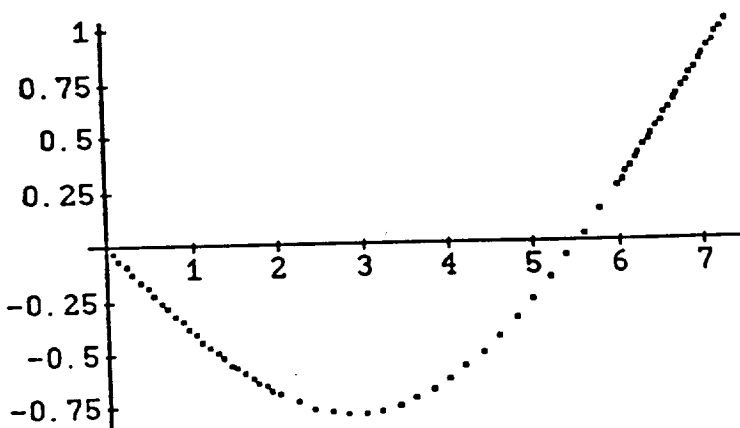
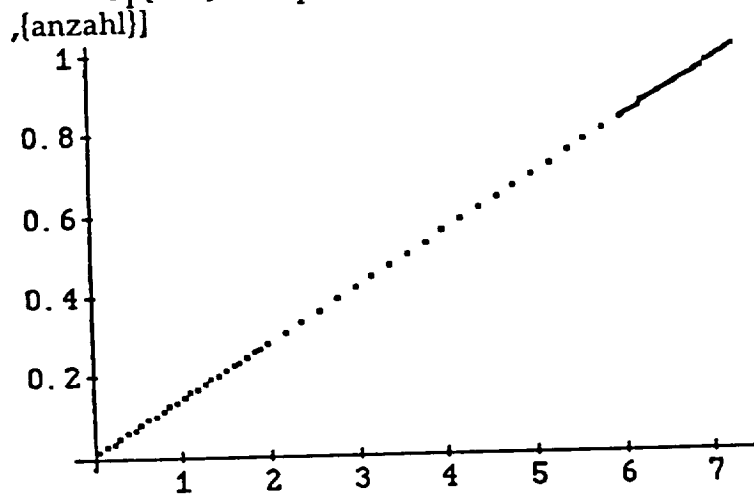
```

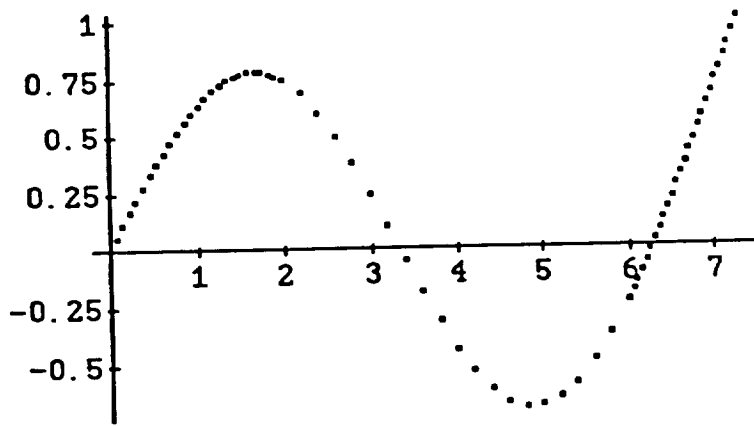
Plot nonrotating eigenvectors

```

run=0;
Do[
  run=run+1;
  "coordinate of the current element";
  xi[1]=elementlaenge[1];
  ort=1;
  Do[
    ort=ort+1;
    xi[ort]=xi[ort-1]+elementlaenge[ort];
    ,{n-1}];
  datapairs=Table[coords,{n}];
  ii=0;
  Do[
    ii=ii+1;
    datapairs[[ii]]={xi[ii],u[run]{{ii}}};
    ,{n}];
  bild[run]=ListPlot[datapairs];
  dp[run]=datapairs;

```





and so on..

rotating eigenvectors

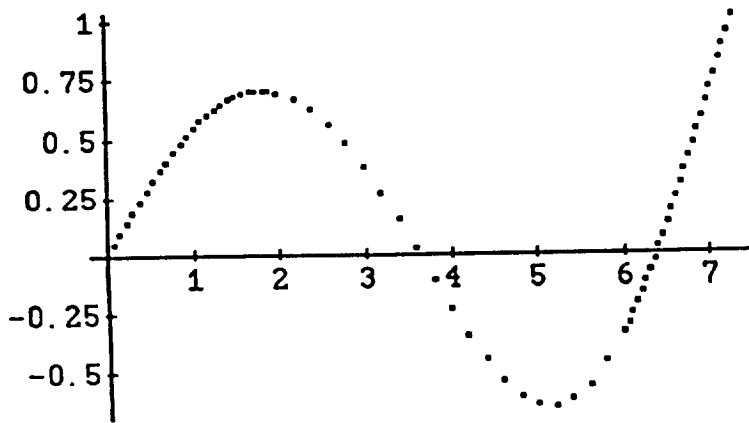
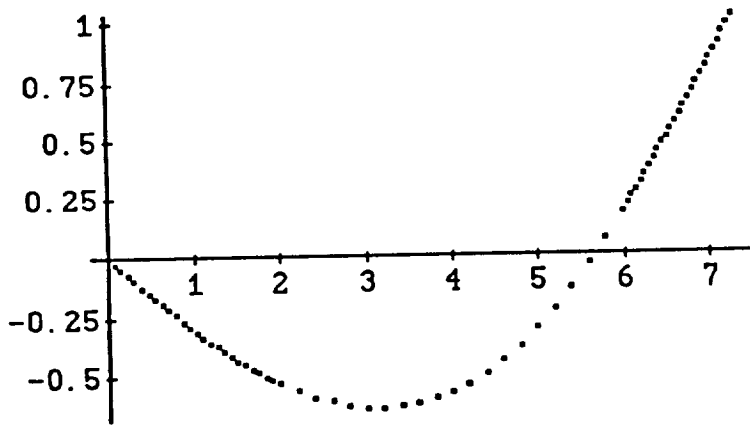
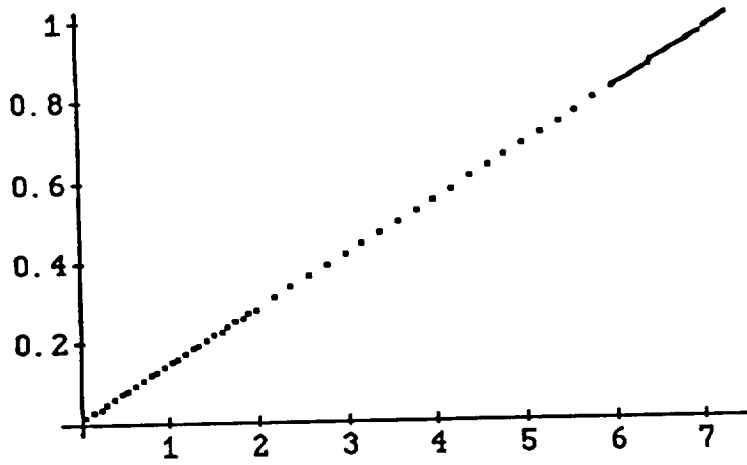
```

run=0;
Do[
  run=run+1;
  "coordinate of the current element";
  xi[1]=elementlaenge[1];
  ort=1;
  Do[
    ort=ort+1;
    xi[ort]=xi[ort-1]+elementlaenge[ort];
    ,{n-1}];

  datapairs=Table[coords,{n}];
  ii=0;
  Do[
    ii=ii+1;
    datapairs[[ii]]={xi[ii],urot[run][[ii]]};
    ,{n}];

  bildrot[run]=ListPlot[datapairs];
  dprot[run]=datapairs;
,{anzahl}]

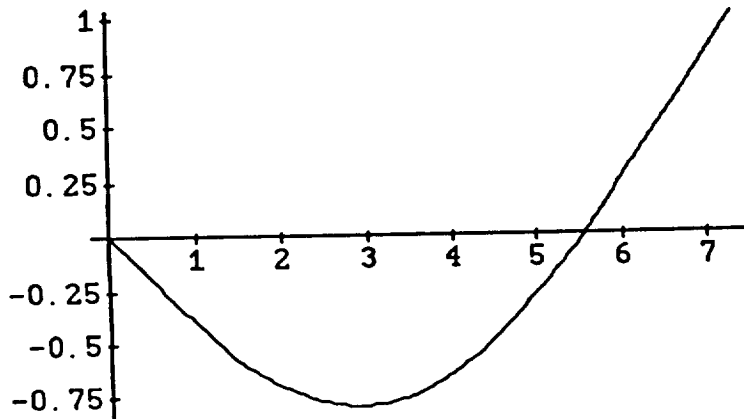
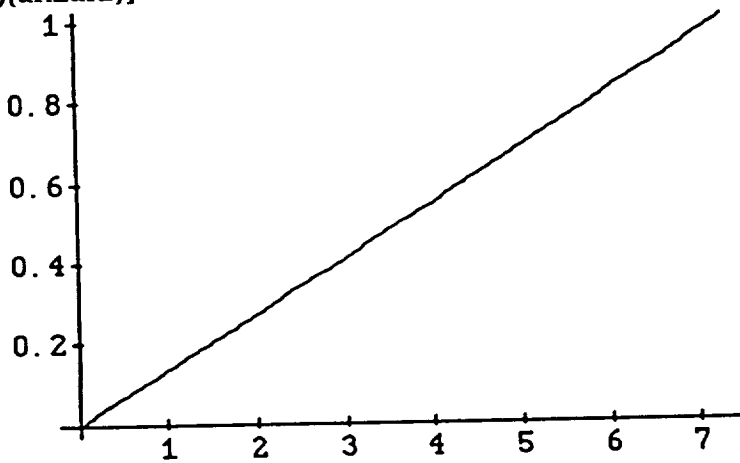
```

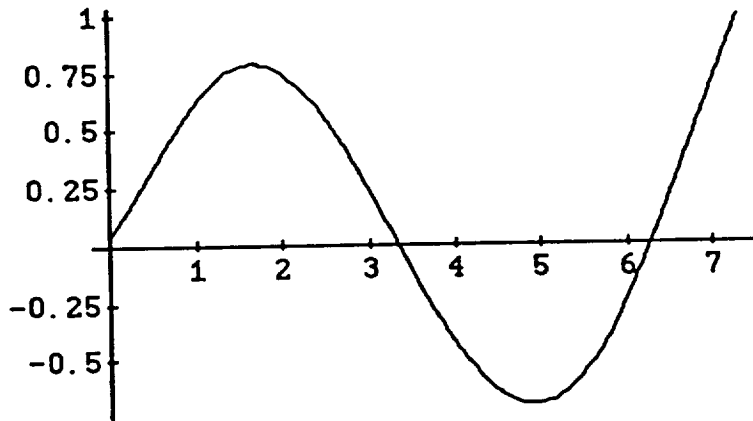


and so on...

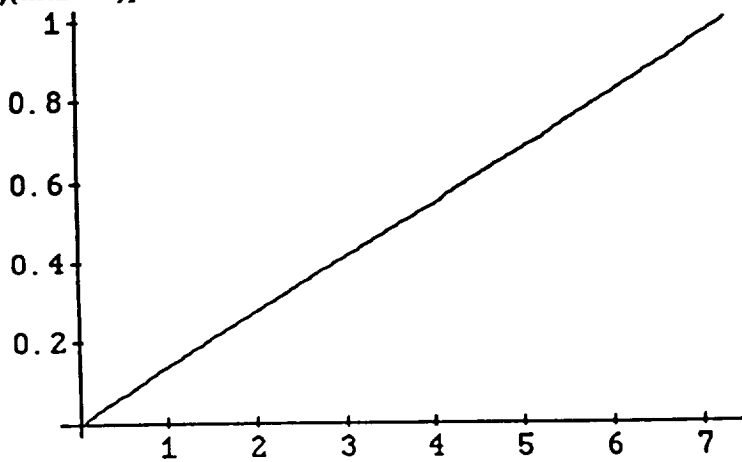
"polynomial approach non-rotating"

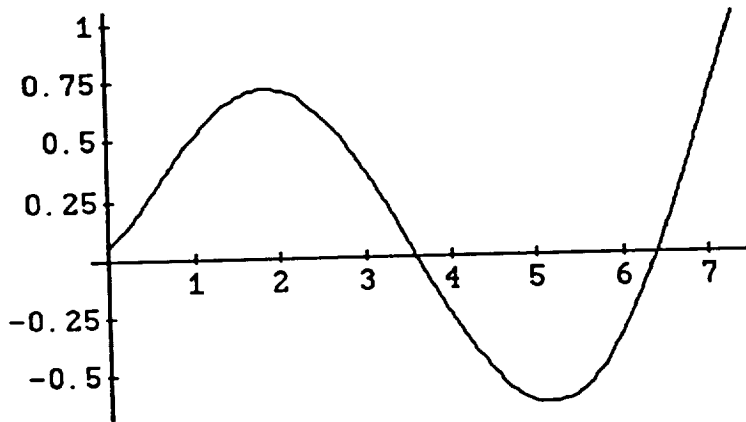
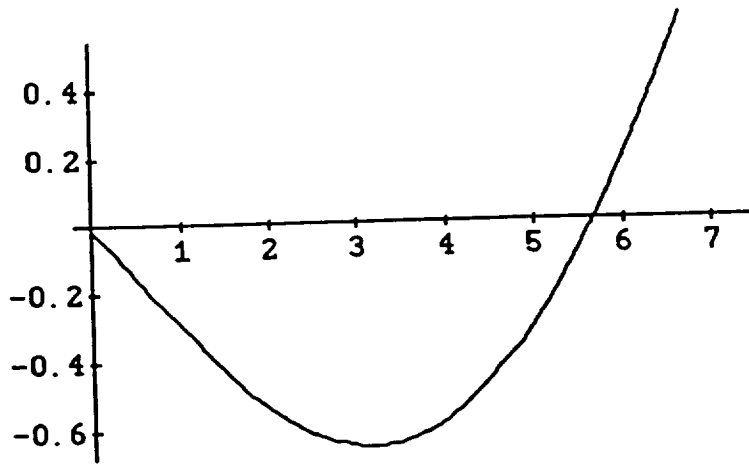
```
run=0
ii=.
x=.
Do[
run=run+1;
*****;
"degree of approach: Nr. of eigenform+3";
*****;
polyu[run]=Fit[dp[run],Table[x^ii,(ii,0,run+3)],x];
,{anzahl}}
run=0
Do[
run=run+1;
fkt[run]=Plot[polyu[run],{x,0,lges}];
,{anzahl}}
```





```
" rotating"
run=0
ii=.
x=.
Do[
run=run+1;
*****";
" #eigenform+2 ";
*****";
polyurot[run]=Fit[dprot[run],Table[x^ii,{ii,0,run+2}],x];
,{anzahl}]
lges
7.29
run=0
Do[
run=run+1;
fktrot[run]=Plot[polyurot[run],{x,0,lges}];
,{anzahl}]
```





Compare the non-rotating and the rotating eigenforms

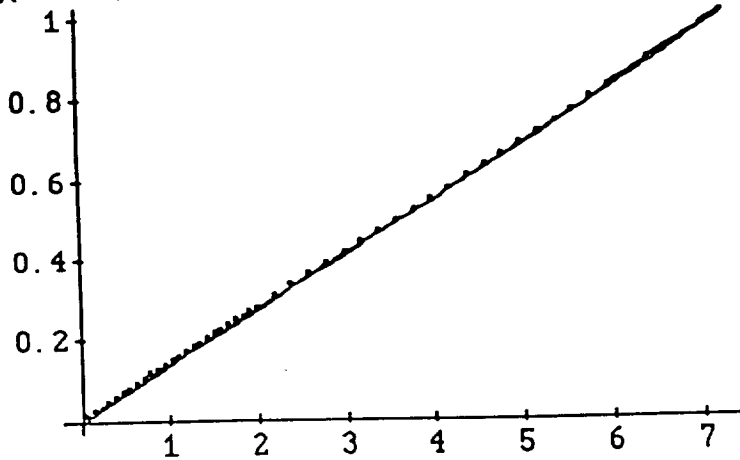
run=0

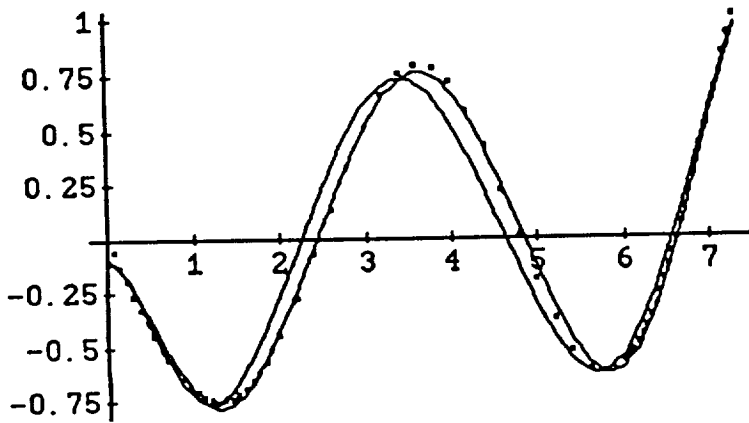
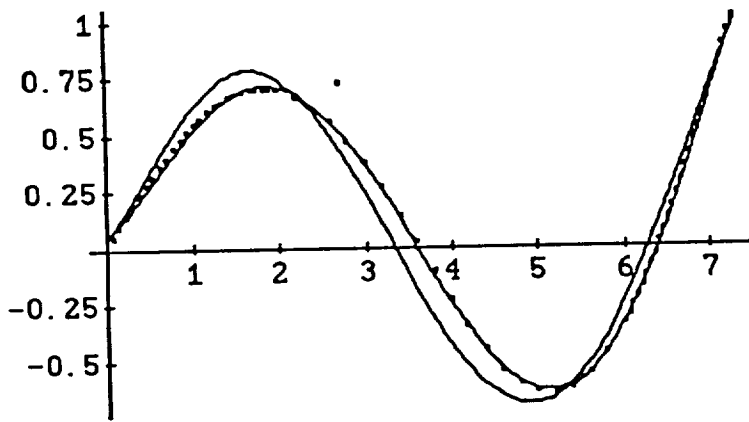
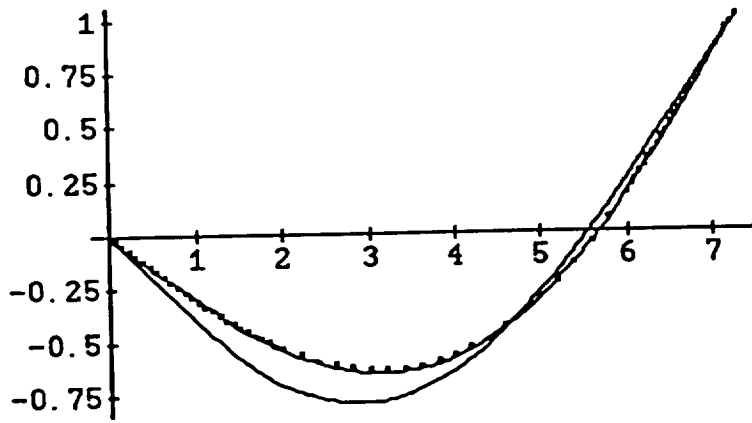
Do[

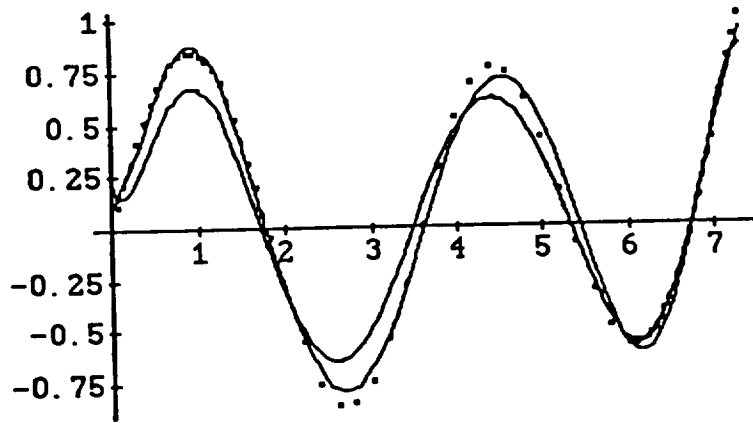
run=run+1;

Show[fkt[run],bildrot[run],fktrot[run]];

,{anzahl}]







End ROTATOR

```

Save data
Write["nrothi1",u[1]]
Write["nrothi2",u[2]]
Write["nrothi3",u[3]]
Write["nrothi4",u[4]]
Write["nrothi5",u[5]]
Write["rothi1",urot[1]]
Write["rothi2",urot[2]]
Write["rothi3",urot[3]]
Write["rothi4",urot[4]]
Write["rothi5",urot[5]]
ii=.
xi70=N[Table[xi[ii],[ii,1,n]]]
Write["xi hin (70)",xi70]

```

References

References, Part A

- A-1. Gasch, R. and Knothe, K. , "*Strukturdynamik*", Band I und II, Springer Verlag, 1989
- A-2. Dietrich, G. , "*Schwingungen*", Vorlesungen an der Universität Stuttgart, Institut für Statik und Dynamik der Luft- und Raumfahrtkonstruktionen, WS 1987/88 - SS 1988
- A-3. Halvorsen, W.G. and Brown, D.L. , "Impulse Technique for Structural Frequency Response Testing", *Sound and Vibration Magazine*, Nov. 1977, pp. 8-21
- A-4. Alexopoulos, A. "*Structural Dynamics Measurement and Analysis*", Hewlett-Packard Structural Analysis Seminar
- A-5. Walgrave, S.C. , "Understanding Modal Analysis", *Technical Paper Series # 780695*, Society of Automotive Engineers, 1978

References, Part B

- B-1. Bishop, R.E.D. and Johnson, D.C., "*The Mechanics of Vibration*", Cambridge University Press, 1960
- B-2. Yntema, R.T., "*Simplified Procedures and Charts for the Rapid Estimation of Bending Frequencies of Rotating Beams*", NACA TN 3459, June 1955
- B-3. Loewy, R.G. and Khader, N., "Natural Frequency of Rotating Beams Using Non-Rotating Modes", *Journal of the American Helicopter Society*, Vol.27, No.10, 1982, pp.75-78
- B-4. Bathe, K.-J. , "*Finite-Elemente-Methoden*", Springer Verlag, 1986

- B-5. Carnegie, W. , "Vibrations of Rotating Cantilever Blading: Theoretical Approaches to the Frequency Problem Based on Energy Methods", *Journal Mechanical Engineering Science*, Vol.1, No.3, 1959
- B-6. Bisplinghoff,R., Ashley,H. and Halfman,R., "Aeroelasticity", 2nd ed., Addison Wesley, 1957
- B-7. Kufield, R.M. and Ngujen, D. , "Full-Scale Uh-60A Rotor Blade Nonrotating Modal Analysis Shake Test", NASA Technical Memorandum 101005, Nov. 1989
- B-8. Smith,B.T. , Boyle, J.M. et. Al. , "Matrix Eigensystem Routines-EISPACK Guide", 2nd ed., Springer-Verlag, 1976
- B-9. Dinkler, D. and Ahrens, H. , "Finite-Element-Methoden" , Bericht Nr. 88-50, Institut für Statik, Technische Universität Braunschweig , 1988
- B-10. McKillip, R.M. , "Kinematic Observers for Rotor Vibration Control", *Proc. 42nd American Helicopter Society National Forum*, June 1986
- B-11. Craig, R.R. Jr. , "Structural Dynamics", John Wiley and Sons, 1981
- B-12. Guy, Strange , "Hey, Let me tell ya someting about dynamics", Basement of the Graduate Colledge, The D-Bar, Nov. 1989
- B-13. Paz, M. , "Structural Dynamics", Von NostrandRheinhold Company, 1980
- B-14. Ramsey, K.A. , "Effective Measurements for Structural Dynamics Testing", Part I and II , *Journal of Sound and Vibration*, Vol. 10, No. 4, 1975
- B-15. Meirovitch, L. , "Elements of Vibration Analysis", McGraw-Hill Book Company, 1986

References, Part C

- C-1. Seto, E.I. , *"NASA/ARMY Black Hawk (UH-60) Rotor Project Plan"* (Draft), NASA- Ames Research Center, Moffet Field, California, March 1986
- C-2. *"TRENDS"*, Analytical Mechanics Associates, Inc., Mountain View, California, May 1988
- C-3. Newland, D.E. , *"Random Vibrations and Spectral Analysis"*, 2nd ed., Longman House, 1984
- C-4. Newland, D.E. , *"Mechanical Vibration Analysis and Computation"*, Longman Scientific and Technical, 1989
- C-5. Young, T. , *"Linear Systems And Digital Signal Processing"*, Prentice-Hall Inc., 1985
- C-6. Wolfram, S. , *"Mathematica"*, Addison-Wesley Publishing Comp., 1988

INSTRUMENTED BLADE EXPERIMENTS USING A LIGHT AUTOGIRO

Robert M. McKillip, Jr., Assistant Professor
Michael H. Chih, Research Assistant
Mechanical and Aerospace Engineering Department
Princeton University, Princeton, NJ 08544 U.S.A.

Abstract

Results from a program to instrument the rotor blades of a light autogiro are described. The work was initiated to provide additional data on rotor dynamic response as well as investigate practical implementation issues on the use of blade-mounted instrumentation for rotor state feedback. A description of the aircraft and rotor electronics hardware design and installation is given, along with results to date from the initial flight test program for complete system check-out.

Introduction

Recent attempts to expand both the fidelity of engineering models for rotorcraft systems and the frequency bandwidth for helicopter flight controllers have required more accurate models of coupled rotor and airframe dynamics. The complexity of the engineering modeling problem, coupled with the general lack of sufficiently detailed flight test data, have made improvements in complete rotorcraft aeroelastic predictions difficult. Efforts to expand the available data for correlation exercises are underway [1], but such programs may experience funding and operational delays along with regulatory hurdles that preclude rapid turnaround for timely engineering research efforts.

As a means of addressing this data deficiency, a program is underway at Princeton University to instrument a Bensen B8-M Gyroglider for towed-flight investigations (Figure 1) [5]. This aircraft is an extremely simple teetering rotor autogiro whose power is supplied by towing the vehicle behind an auto along a runway or suitably paved surface. The University's inactive runway at the Forrestal Campus has served as the vehicle's testing ground. The use of a simple test aircraft provides the ability to perform fundamental

aeroelasticity experiments on a full size vehicle without the additional burden of maintenance manpower associated with a production helicopter. The added capability of an "in-house" test vehicle affords the researcher the luxury of planning and executing tests that are driven by the nature of the test data and not the predetermined schedule of the test program.

The desire to conduct instrumented rotor experiments on full size aircraft was inspired by similar efforts being done on a model rotor at the Rotorcraft Dynamics Laboratory (Longtrack) at Princeton's Forrestal campus [2] and aided by results reported from an instrumented AH-1G Cobra helicopter test by the NASA [3]. The design goals of the instrumentation system, and the impact of flight safety and testing procedure on the realization of its mechanical and electrical components is described below.

Basic Instrumentation Design Goals

Data Acquisition

In order to provide a basis for comparison with model results, blade mounted accelerometers and strain gauges were selected for the autogiro rotor experiments described. These sensors typically provide differential outputs that require some form of amplification prior to sampling for data storage. On the model tests, both the sensor excitation voltages and differential outputs are transferred from the fixed to rotating frames using a slip ring assembly. Such a technique requires from two to four rings per sensor, plus the associated hub attachment for the slippings and sensor wires. This type of installation was not possible, due to the inherent simplicity of the autogiro's hub. Since no torque is provided to the rotor, the primary aircraft control is performed through direct shaft tilt of the rotor, which is mounted in a pillow block attached to a sealed bearing assembly. Such an arrangement makes the main rotor shaft inaccessible for slipping attachment or routing of wires through its interior. Thus, the decision was made at an

Presented at the 16th European Rotorcraft Forum, Glasgow, Scotland, September 18-20, 1990.

early stage to telemeter the data from the rotating to fixed frames without the direct use of rotating brushes or slipping pick-ups. Use of a rotor-mounted telemetering system thus requires a co-located electronic power source, since no direct wire transfer was then possible from the aircraft fuselage. In order to reduce battery size on the hub, all integrated circuits used CMOS chips wherever possible, with power supplied from two standard 9-volt transistor batteries. A photograph of the instrumentation assembly is shown in Figure 2.

An additional system requirement was that the instrumentation system not adversely affect the mechanical integrity or aerodynamic performance of the rotor blades. The blades on the autogiro are stock Bensen factory-built blades constructed from aluminum sheeting riveted to a solid spar. The airfoil is a Bensen design, having a flat underside and slight reflexed trailing edge, originally developed for construction by the homebuilder from plywood sheeting. Since access to the blade's interior was not possible, multi-conductor ribbon cable for sensor signal routing was secured to the flat underside of the blade using a combination of double-sided sticky tape and epoxy, covered with one spanwise and several chordwise segments of mylar adhesive tape.

Aerodynamic performance considerations dictated the scheme used to condition the sensor signals. Unlike the system used in Reference [3], cost considerations did not allow development of custom millimeter-thick integrated circuitry for sensor signal conditioning and amplification. Since stock integrated circuits (IC's) would be used, a minimum number of chips could be tolerated at each sensor station in order to reduce the adverse drag penalty from surface irregularities they introduce. Although sensor noise would be lowest for co-located sensors, amplifiers and analog to digital (A/D) converters, the associated multiplexing necessary would add at least an additional chip, bringing the total to three ICs at each sensor's spanwise location. Thus, only the sensor's amplifier is located on the blade span, with the A/D and multiplexing operations performed by a single IC at the rotor hub. This arrangement also required only four wires to extend over the entire rotor radius. An installed accelerometer and amplifier are shown in Figure 3.

Sensor signal A/D sampling rate was traded off against multiplexing capability for the digitizing of the rotor data, with the final choice using the TLC541 LinCMOS chip from Texas Instruments as the primary workhorse for conversion of the data to digital form. This IC provides 11 channels of multiplexing capability into an 8-bit A/D converter, with an equivalent throughput rate of 1,024 samples per second on each channel. Since the nominal rotor speed of the autogiro is 375 rpm, the system's Nyquist rate (maximum digital bandwidth) is 82/rev, well beyond any potential dynamic or aeroelastic phenomenon one might expect to observe. For this reason, there are no anti-aliasing filters used prior to A/D conversion.

The multiplexer chip, originally designed for interfacing with a microprocessor, allows for direct control of both channel addressing and serial bit output rate through reasonably complex interfacing with timing and address pins. In order to avoid the requirement of co-locating a dedicated microprocessor, the complex timing patterns and address lines were stored ("burned") into an EPROM, driven by a counter and clock. The individual data bits for each of the 11 channels are sequentially loaded onto the serial digital data bus, followed by a test channel for receiver synchronization purposes. This "synch" word is modified to produce a string of 9 bits that cannot be duplicated by any combination of the 11 channel's data words, thus providing a unique marker for each "frame" of data.

To save on the total number of chips at the rotor hub, the counter that drives the EPROM interface chip does not reset to a predetermined value, and thus the first 1024 8-bit words are cycled over for each frame. Since the timing pulses only occupy the first two-thirds of this address space, a blank sector is available in the current frame of serial data for future expansion. This might consist of either additional rotating frame channels, or interwoven fuselage sensor data. This latter method would require a serial decoder and synchronizer in the non-rotating frame on the aircraft, a method that was not used on the current design concept. A diagram of the main circuit functional blocks appears in Figure 4.

Data Transmission and Storage

In order to transmit the digital data from the rotor to the fuselage frame of the autogiro,

the serial bit stream was Manchester encoded so as to provide a timing reference for individual bit transitions. While this format is particularly suited for direct radio frequency modulation, the additional weight and power requirements of a radio transmitter were deemed unacceptable. Instead, the coded signal is fed directly into the rotor blade's aluminum structure, with the pickup signal in the fuselage frame merely consisting of a wire secured to the metal airframe. Thus, the entire aircraft is electronically isolated from the sensor power signals, with the rotor data transmitted directly through the main rotor shaft bearing assembly. Alternate schemes using infra-red diodes, while conceptually feasible, were not nearly as simple as this technique.

Due to the limited amount of both ground support personnel and computational facilities, direct re-broadcast of the data from the autogiro to a ground station was not possible. Instead, appropriate signal modifications were made to the serial coded data so that it could be directly recorded onto an 8mm format video camera/recorder. The camera is a self-contained unit running from its own battery source, and is shock mounted to the autogiro directly in front of the pilot's seat, to allow for convenient access to both the record buttons and tape eject mechanism. Despite the high frequency of the Manchester encoded serial bit stream (1.3 MHz), such signals are well within the bandwidth of conventional NTSC video standards.

Post-flight data processing consist of playing back the recorded signals into a serial-to-parallel digital data synchronizer. The circuitry used to perform the data extraction, shown in functional form in Figure 5, consists of signal conditioning to standard logic levels, bit synchronization using a phase-locked loop (PLL), and data decoding with clocked flip-flop circuits. In order to provide for discrimination between channels, a search/synchronizer scheme using another EPROM and comparator was employed. Since the frame word consisted of a unique 9-bit digital bit pattern, a shift register and bit comparator were used to detect a "match" with this word indicating the beginning of the serial data frame. When the match was detected, the EPROM clock/counters were reset, and each channel was clocked through the shift register, combined with the four bits representing the channel count, and sent into a high-speed

parallel digital data port on an IBM-PC/AT. This data was then stored onto floppy diskettes for additional analysis and processing. After the EPROM cycled through its 11 channels of serial data timing, it entered a "re-match" state in which it looked for another frame start pattern. If this pattern was not found, the synchronizer would enter a "search" mode and warn the user (via light and buzzer) that synchronization was lost and data is invalid. If the pattern was matched, indications of a "locked" state would be given, and the process would cycle over each additional frame of serial data.

Auxiliary Data System Components

In order to interpret the rotor structural dynamic data, some measurement of the operating state of the autogiro flight condition was required. Of particular importance is the rotor advance ratio, and the associated angle of attack of the rotor blades. As the detailed flow of the rotor is unavailable, several fuselage-mounted sensors were used to infer this information. These sensor data were routed to a pulse-width modulator (PWM) box having a capacity for 43 channels of analog data sampled at 20Hz per channel. This data acquisition system was previously used in flying qualities experiments at Princeton on variable-stability general aviation aircraft and gliders [4]. The PWM signal was in turn fed into the separate audio input channel of the 8mm video camera, thus providing separate but synchronous data recordings for both rotor and fuselage sensor data.

The rotor speed was measured using a magnet mounted on the rotor hub, and a Hall-effect sensor on the rotor mast just below the hub pillow block assembly. The pulses were fed into a PLL circuit that output an analog voltage proportional to pulse frequency, with this information displayed to the pilot and sent to the fixed-frame data commutator system. Autogiro angle of attack and sideslip were measured through two vanes mounted on low friction potentiometers, and airspeed was taken from a cup anemometer. Rotor shaft tilt was measured from stick potentiometers, and rudder pedals were instrumented as well. A picture of the data system components is in Figure 6.

Power for the PWM commutator was provided from four 9-volt batteries tied in

series, regulated to a nominal 28-volt DC level. Although larger power rechargeable batteries were available, their significant increase in weight deemed them unacceptable for initial flight tests and data system check-outs. Additional instrumentation, such as use of Princeton's Inertial Measurement Unit [4], will require upgrading the available power source on the autogiro airframe.

Since monitoring of the video tape index during flight could jeopardize safety through increased pilot workload, the FM communicators used between pilot and tow vehicle personnel was coupled into the audio input channel of both the on-board video recorder and the tow car's video camera. Since this same space on the tape is used by the fixed-frame sensors, voice markers were stored only during push-to-talk operations of the pilot. Simultaneous voice recording allowed for approximate synchronization between the signals from both cameras during postflight analysis.

Preliminary Testing

As a means of both adjusting amplifier offsets and confirming data transmission, storage and retrieval/synchronization, an impact test was made of the rotor blade. An instrumented force hammer in conjunction with the blade-mounted accelerometers were recorded for a series of impacts at several spanwise locations in order to identify the non-rotating mode shapes of the autogiro rotor blade. Such information is essential for accurate post-processing of the accelerometer data, as is pointed out in [2].

Since the spanwise accelerometers are oriented to measure out-of-plane accelerations, as the blade deflects out of the plane of rotation, these sensors will measure both blade vertical acceleration as well as a component of rotational acceleration proportional to the local slope at the sensor's spanwise location (see Figure 7). This information can then be used in a processing scheme called a Kinematic Observer [6] to reconstruct rotor blade state variables. On the autogiro, however, the ratio between the measurement of fundamental teetering (flapping) acceleration and teetering displacement is constant for any spanwise station. For any accelerometer at spanwise location r , it will sense contributions from each

mode's acceleration ($\ddot{g}_i(t)$) and each mode's displacement ($g_i(t)$) according to:

$$\text{accel}(r,t) = \sum_{i=1}^{\infty} \eta_i(r) \ddot{g}_i(t) + \frac{\partial \eta_i(r)}{\partial r} r \Omega^2 g_i(t)$$

where $\eta_i(r)$ represents a particular blade natural mode shape. For the case of the rigid teetering mode, $\eta_1(r) = r$, giving contributions from the teetering mode $\beta_1(t)$ as:

$$r \ddot{\beta}_1(t) + r \Omega^2 \beta_1(t)$$

and for simple harmonic flapping at 1/rev, these two terms cancel. For this reason, a potentiometer was installed in the rotor hub to measure rigid teetering motion, and the accelerometers were positioned so as to maximize their sensing of the various higher blade vibratory modes.

Flight operations for testing the autogiro instrumentation are currently underway at the inactive runway at Princeton University's Forrestal Campus. Since the autogiro has no engine, it is towed by a nylon rope attached to its nose from an automobile. While this results in limited continuous flight time, the runway's 3000 foot length allows flight experiments of approximately 45 to 60 seconds duration, depending on wind direction along the tow path. Communications are kept with the tow vehicle driver and observer using FM transceivers, and a glider tow hitch with release may be operated by the pilot in the event of fouling of the tow line.

Rotor data power has been tested to provide consistent data for over two hours of operation, and fuselage batteries have a roughly equivalent life. Battery life on the video camera used for serial data storage is slightly under an hour, resulting in approximately fifteen flights during a standard sequence of runs. Such a record provides a wide range of test points for analysis, the results of which will appear in a forthcoming paper.

Acknowledgements

Partial support for this work was provided from a Marshall Scholarship from the

Department of Mechanical and Aerospace Engineering at Princeton University. The authors especially wish to thank the substantial contributions from Mr. James E. Risser, also of Princeton University.

References

- [1.] Seto, E., "NASA/Army Blackhawk (UH-60) Rotor Project Plan", NASA Ames Research Center, Moffett Field, California, March 1986.
- [2.] McKillip, R. M., Jr., "Experimental Studies in System Identification of Helicopter Rotor Dynamics", Proc. Fourteenth European Rotorcraft Forum, Milano, Italy, September 1988; Also *Vertica*, V. 12, No. 4, pp. 329-336, 1988.
- [3.] Knight, V. H., Haywood, W. S., Jr., and Williams, M. L., "A Rotor-Mounted Digital Instrumentation System for Helicopter Blade Flight Research Measurements," NASA TP 1146, April 1978.
- [4.] Sri-Jayantha, M., "Data Acquisition for Stall/Spin Flight Research", Joint University Program for Air Transportation Research - 1982, NASA CP 2285, Langley Research Center, December 1982.
- [5.] Chih, Michael H., "Airborne Digital Data Acquisition System for a Rotor," Bachelor of Science in Engineering Thesis, Mechanical and Aerospace Engineering Department, Princeton University, May 1990.
- [6.] McKillip, R. M., Jr., "Kinematic Observers for Active Control of Helicopter Rotor Vibration," *Vertica*, V.12, n.1/2, 1988.

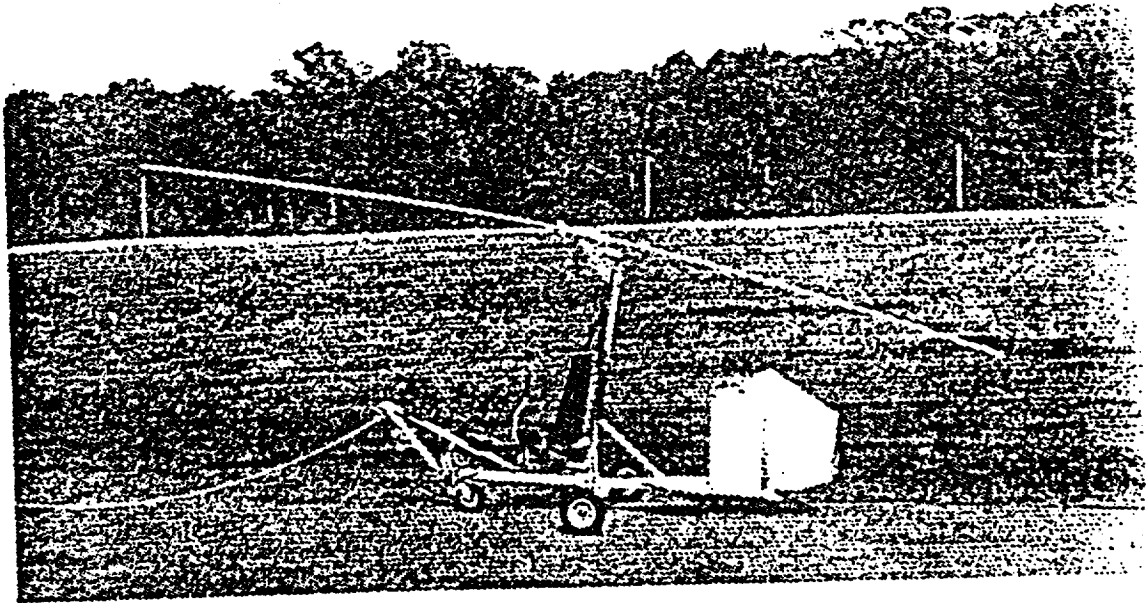


Figure 1: Instrumented Bensen autogiro (glider)

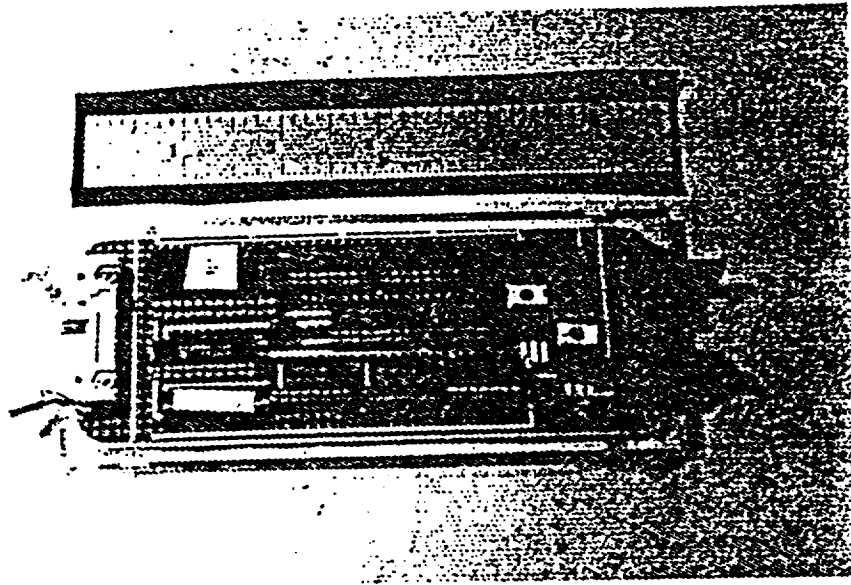


Figure 2: Digital data acquisition and telemetry circuitry

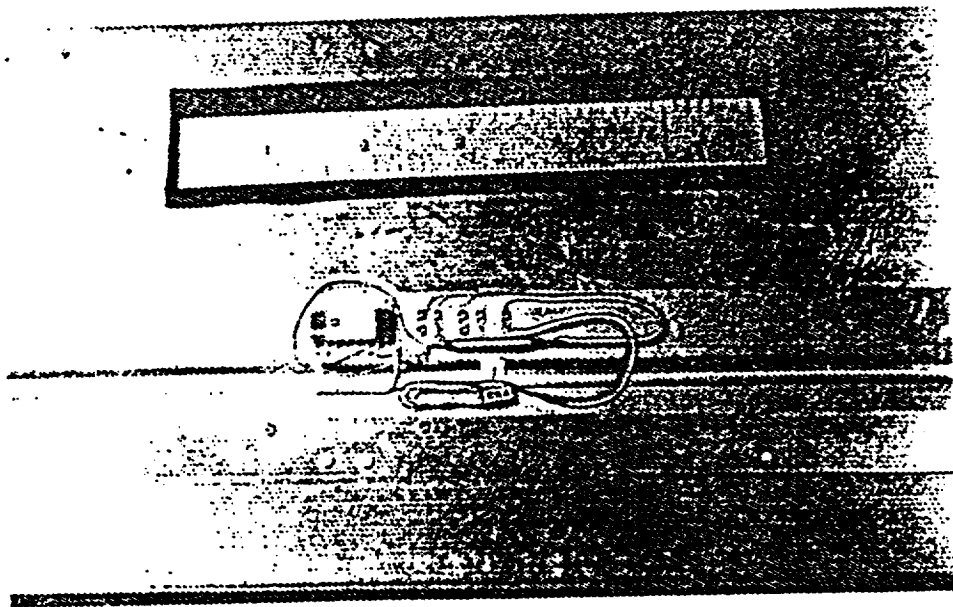


Figure 3: Accelerometer and amplifier installation on blade underside

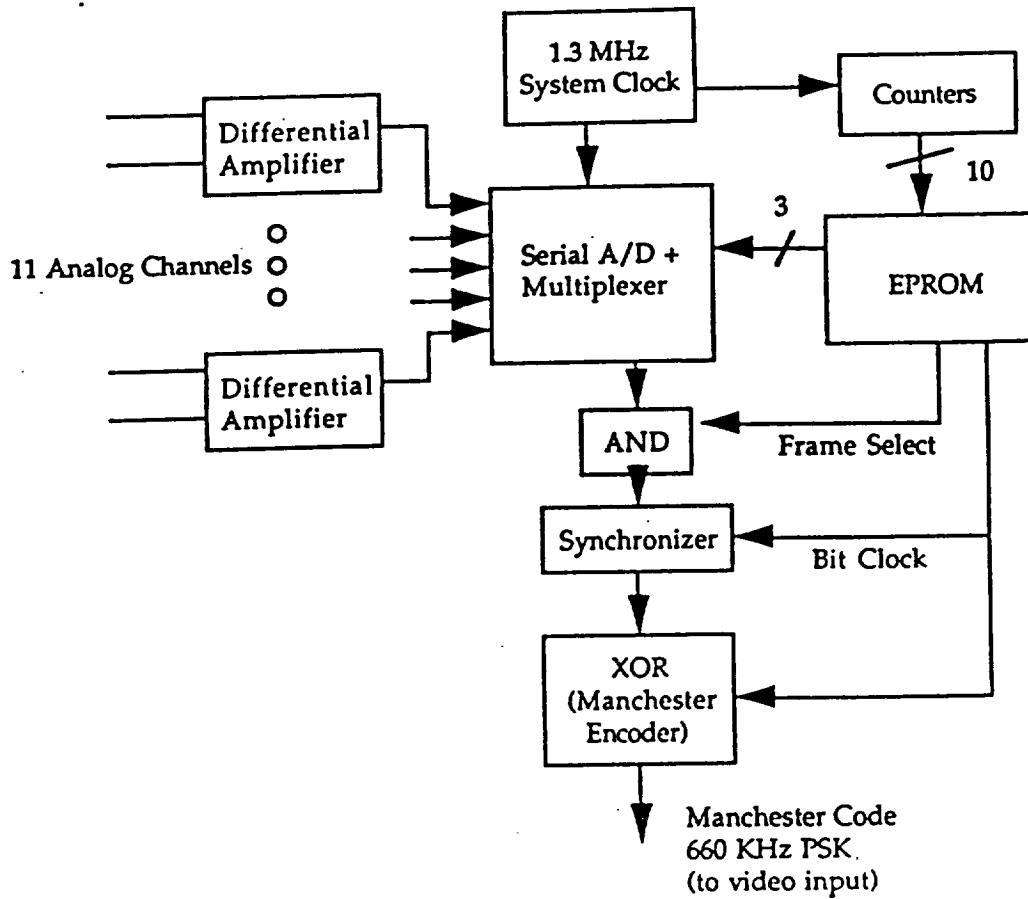


Figure 4: Rotor data acquisition circuit functional diagram

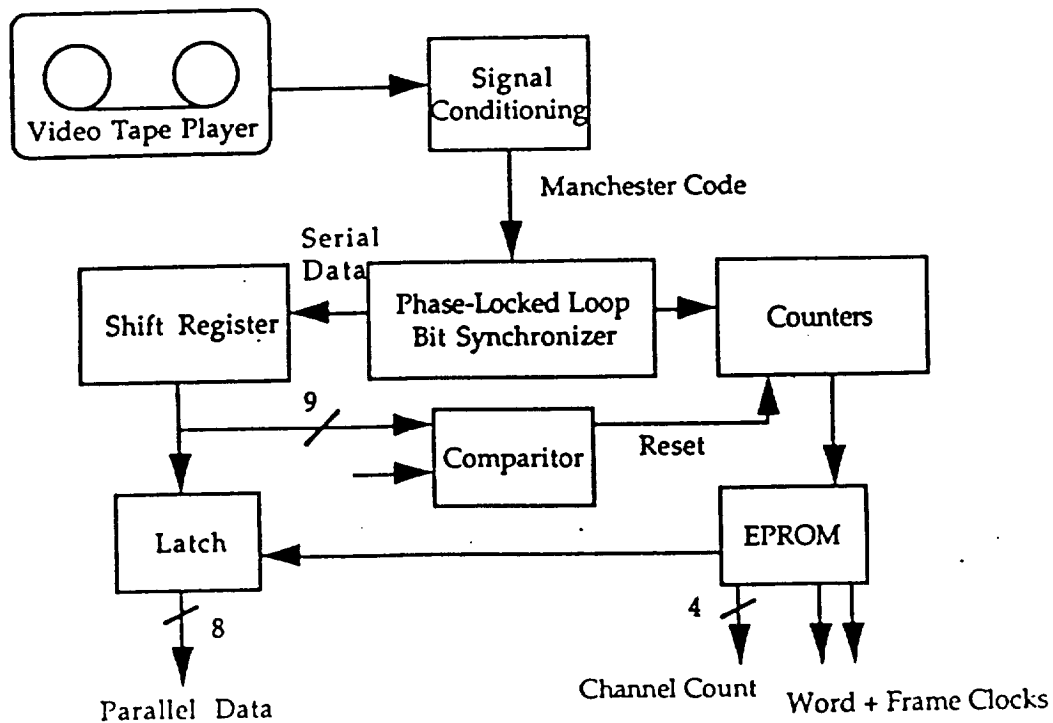


Figure 5: Digital data synchronization and parallel output functional diagram

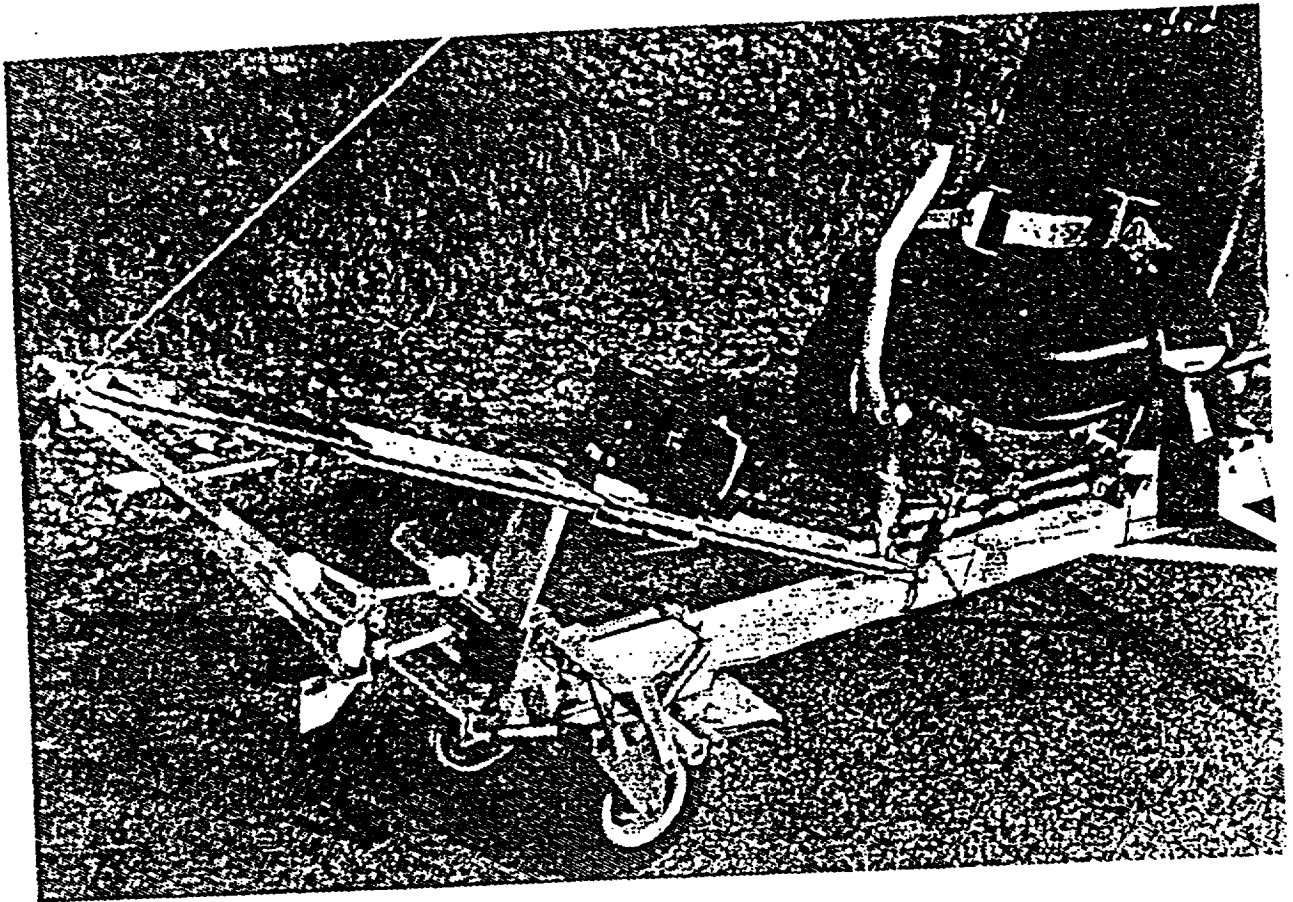
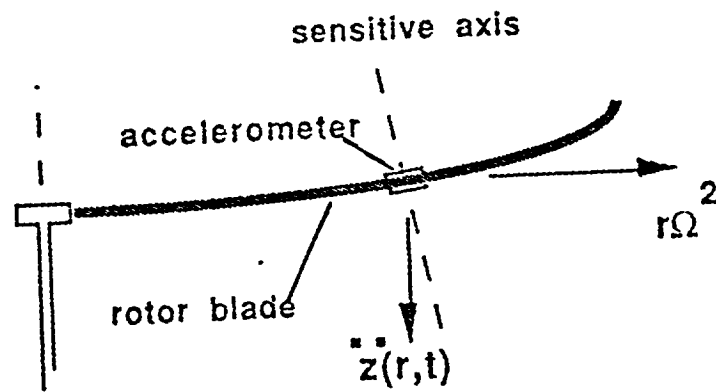


Figure 6: Fuselage mounted airdata sensors and camera attachment



$$\text{accel}(r,t) = \sum_{i=1}^{\infty} \eta_i(r) \ddot{g}_i(t) + \frac{\partial \eta_i(r)}{\partial r} r \Omega^2 g_i(t)$$

Fig. 7: Out-of-plane accelerometer sensing schematic